

Optimum Design of Propeller Boss Cap Fins (PBCF) by Model Scale Numerical Evaluation

Christian K. Rosenvinge & Marcus P. Sandland

Aalborg University, Energy Technology, 28th May 2021



AALBORG UNIVERSITET



DEPARTMENT OF ENERGY TECHNOLOGY
AALBORG UNIVERSITY

Energy Technology
Aalborg University
<https://www.et.aau.dk/>

Title:

Optimum Design of Propeller Boss Cap Fins (PBCF) by Model Scale Numerical Evaluation

Type:

Master's Thesis

Project Period:

Spring Semester 2021

Project Group:

TEPE4 - 1002

Participants:

Christian Kjaer Rosenvinge
Marcus Pless Sandland

Supervisors:

Chungen Yin

Page Numbers:

74

Date of Completion:

28th May 2021

Christian Kjaer Rosenvinge
<rosenvinge93@gmail.com>

Marcus Pless Sandland
<m_sandland@yahoo.dk>

Abstract:

Implementation of Propeller Boss Cap Fins (PBCF) have presented great mitigation capabilities towards the induced hub vortex downstream of shipping propulsion systems, which implies an increased propeller efficiency.

This project investigates the design and optimisation process of PBCF for a specified Controllable Pitch Propeller (CCP), achieved through a model-scale steady-state 3D RANS analysis in the software STAR-CCM+. The numerical model is validated against empirical data both with a rudder attached and at open water conditions, where satisfactory results justified the further utilisation of the model.

From a thorough literature study a basis for the geometrical composition of the PBCF were formulated and analysed through the numerical model. By investigating different hydrofoils it was found the NACA 4412 yielded the greatest result.

An individual optimisation procedure for each parameter were conducted, which concluded that the span height, circumferential and axial position were the most influential parameters. From the optimum measure of each parameter the optimised PBCF was achieved, which yielded an increase in efficiency of minimum 1.0 % for a wide range of ship speeds. For varying advance ratios an efficiency improvement between 0.59 % and 1.19 % was found. Pressure contour comparisons concluded that the induced hub vortex was completely destroyed.

The content of this report is freely available, but publication (with reference) may only be pursued due to agreement with the author.

Copyright © Aalborg University 2021

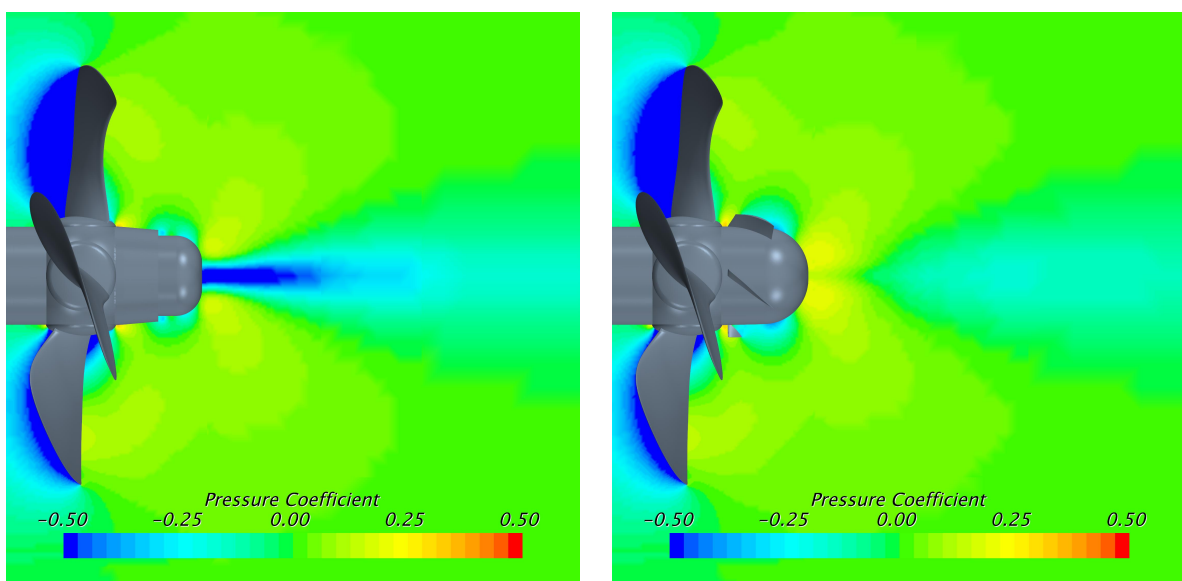
Executive Summary

A steady-state 3D computational model is formulated based on a literature study of similar research, for a model propeller/rudder system. The quality of the model is evaluated with indicators within the computational software and a grid independence analysis is conducted to insure valid and consistent results. The model is validated against empirical data produced by MAN Energy Solutions Frederikshavn and the deviation between the efficiency when the rudder is attached is maximum 0.5 %. The model is thus considered appropriate for the purpose of optimising and evaluating PBCF designs.

A thorough literature study regarding the geometrical parameters composing PBCF have been conducted. The various literature showed similar optimised values for the different parameters, but contradicting terminologies, insufficient data, or limited illustrations are present throughout the literature. A simple definition of the geometrical parameters are proposed in this project together with elaborate illustrations.

The original boss cap were replaced with a new design, which eliminated the intersection caused of a bolt notch and the installation of the fins. The new boss cap designed yielded an increase in efficiency of 0.17 % compared with the original, but were unable to mitigate the hub vortex generated.

Based on the conducted literature study, a base design formed on the basis of utilising the traditional rectangular profiles and the determined optimum measures of each parameters were established. This design was carefully analysed, where a perpendicular installation of the fins to the boss cap's surface curvature performed superior to the traditional installation. Likewise, did the analysis results in a replacement of the rectangular fins with hydrofoils instead. As a result of nine hydrofoils tested and compared with the rectangular profile, the NACA 4412 hydrofoil yielded the highest efficiency gain. The perpendicular installation of the fins and the NACA 4412 were implemented, and this acted as the base design upon which a parametric study was conducted.



(a) Original boss cap without PBCF.

(b) New boss cap with PBCF.

Figure 1: Pressure coefficient contours plots around the propeller and boss cap without the rudder attached for better visualisation of the eliminated hub vortex.

From the parametric study, it was evident that the literature study had yielded a great starting point for the base PBCF design, where few of the implemented parameters needed alteration. It was found that the span height, circumferential position, and axial position had the most significant impact on the efficiency, and should therefore be carefully examined and implemented. The insight and results from the parametric study were utilised in the PBCF design, where each parameter was studied independently. Therefore, a new study was performed with a basis in the optimum measures determined from the parameter study taking the interaction between the parameters into account. This indicated that small changes in the installation angle, maximum thickness, and axial position should be implemented. This resulted in the optimised design, which was found to increase the efficiency by 0.7284 percentage points, or approximately 1.04 % when compared to the original boss cap without PBCF. An analysis of the yield strength of the PBCF ensured that the design was physically realistic and could withstand the forces applied. The hub vortex generated downstream of the original boss cap can be seen in Figure 1a visualised through the low-pressure zone. In Figure 1b the hub vortex is completely mitigated by the PBCF implementation, yielding the increase in propeller efficiency.

Preface

This thesis is written by Christian Kjaer Rosenvinge and Marcus Pless Sandland at Aalborg University in the spring semester of 2021. The project accounts for 30-ECTS points and is the Master's project for M.Sc. in "Thermal Energy and Process Engineering." The project is written as a back-to-back project, where the initial commence of the research began in the autumn semester of 2020 and is thereby an extension of the previous work conducted.

The thesis is carried out in collaboration with MAN Energy Solutions Frederikshavn located in Frederikshavn, Denmark. The company has provided the authors with empirical data, computational resources, software, hardware, propeller geometry data, CAD files, and general knowledge regarding the subject. The simulations throughout the thesis is conducted utilising a model-scale propeller/rudder system. The numerical model is formulated based on the model-scale CAD files provided.

The authors and MAN Energy Solutions Frederikshavn have settled on a Non-Disclosure Agreement, which restricts the data and information that is presented in the thesis. Therefore, is a percentage increase showcased instead of the actual value of the efficiency in some figures.

Prerequisites

To achieve a considerable comprehension of this thesis's subject, a good understanding of mathematics, fluid dynamics, and numerical modelling is necessary.

Reading Guidance

The thesis is presented in such a way that the reader should peruse it from a pdf file, which accommodates zooming for better visualisation of the numerous figures and tables. The literature throughout this thesis is stated in accordance with the "Harvard Method"; Ogura et al. [1987]. The bibliography is located at the back of the thesis before the appendices are stated. Information about each specific citation is carefully examined to ensure the correct details are stated with regards to the title, author(s), journal, doi, pages, year, conference, etc. The note option is likewise utilised for some citation, which yields additional insight or key information regarding the specific citation, which could be the place of a conference or the like.

The nomenclature is stated on the succeeding page, where the various symbols, super/subscripts, and abbreviations are listed, including a description of each. Through this project, the SI unit system is listed, likewise stated for each variable in the nomenclature.

The numerous equations, tables, and figures presented through this thesis are numbered, heeding their order of appearance and corresponding chapters.

Applied Software

The computational fluid dynamics software *STAR-CCM+* is utilised in this thesis and is provided by MAN Energy Solutions Frederikshavn. The analyses conducted for the several numerical studies are examined through *MATLAB*[®], which likewise have been applied to create the plots and graphs of the results obtained. For designing the Propeller Boss Cap fins, the CAD software *SolidWorks* has been applied.

Acknowledgement

Thanks to our supervisor Chungun Yin for the support and aid throughout this thesis. Likewise, a special thanks to MAN Energy Solutions Frederikshavn for their assistance in completing this thesis. Their practical knowledge, encouragement, and resources have been extremely valuable for the completion of this project.

Thesis Structure

The structure of thesis is visualised in Figure 2:

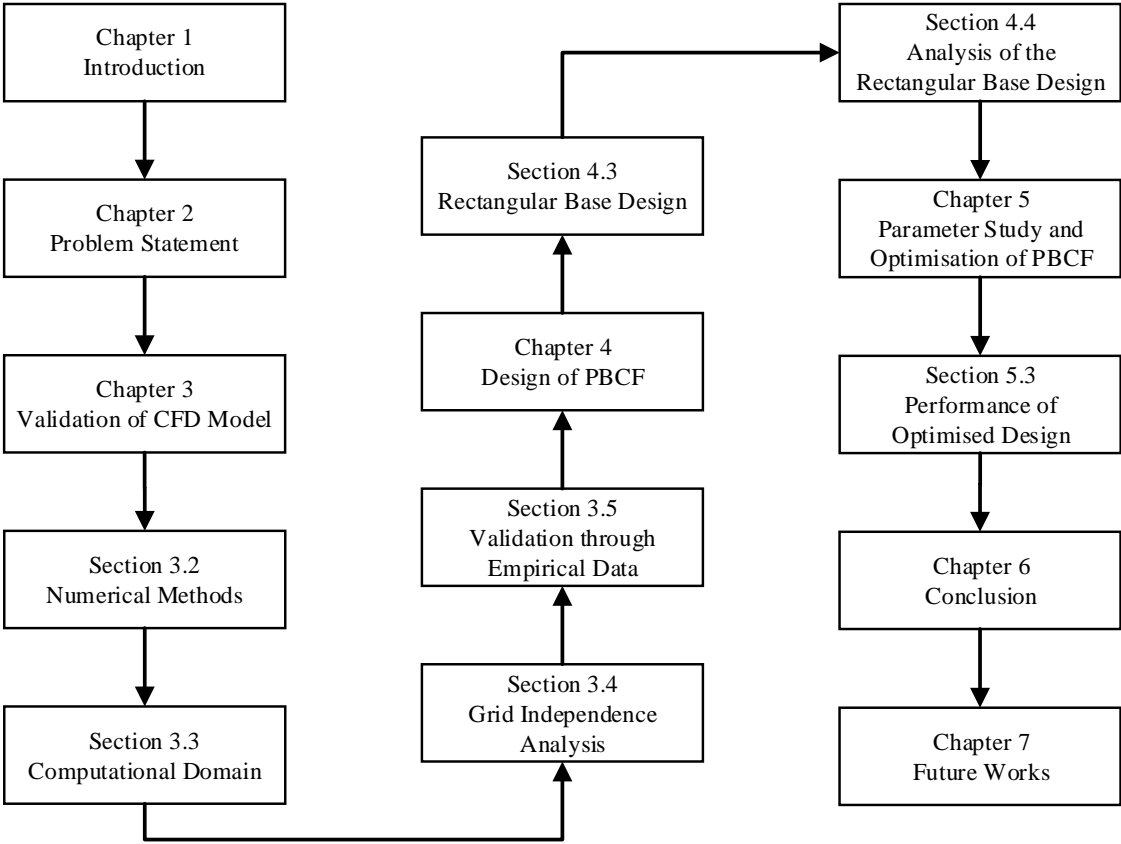


Figure 2: General structure of the thesis.

Nomenclature

Symbol	Description	Unit
a	Circumferential distance	m
b	Axial distance	m
c	Camber	m
C	Coefficient	-
D	Diameter	m
J	Propeller advance ratio	-
K_T	Thrust coefficient	-
K_Q	Torque coefficient	-
l	Length	m
l_c	Chord length	m
n	Number of Fins	-
N	Rotational velocity	s^{-1}
p	Pressure	Pa
P	Pitch	mm
r, R	Radius	m
s	Fin span	m
t	Thickness	m
Q	Torque	Nm
T	Thrust	N
V	Velocity	m/s
V_A	Propeller advance speed	m/s
V_S	Ship speed	m/s
y^+	Non-dimensional wall distance	-

Greek letter	Description	Unit
α	Installation angle	$^\circ$
Δ	Difference	-
ϵ	Propeller blade root pitch angle	$^\circ$
η_o	Propeller efficiency	-
θ	Rake angle	$^\circ$
ν	Kinematic Viscosity	m^2/s
ρ	Density	kg/m^3
ϕ	Slope angle	$^\circ$
ω	Skewness angle	$^\circ$

Sub-/ Superscripts	Description
bc	Boss cap
br	Blade root
D	Drag
L	Lift
max	Maximum
n	Airfoil number
p	Propeller, pressure
PBCF	Propeller Boss Cap Fins
∞	Freestream

Abbreviations	Description
AoA	Angle of Attack
PBCF	Propeller Boss Cap Fins
BST	Baseline Stress Transport
IMO	International Maritime Organisation
EEDI	Energy Efficiency Design Index
ESD	Energy Saving Devices
GCI	Grid Convergence Index
CPP	Controllable Pitch Propeller
FPP	Fixed Pitch Propeller
RB	Rudder Bulb
p.p.	Percentage point

Contents

1	Introduction	1
1.1	State of the Art	3
2	Problem Statement	8
3	Theory and Validation of Computational Model	9
3.1	Ship Propeller Terminology	9
3.2	Numerical Methods	10
3.2.1	Reynolds-Averaged Navier–Stokes (RANS)	10
3.2.2	Segregated Flow Model	10
3.2.3	Shear Stress Transport k - ω Turbulence Model	11
3.2.4	γ - Re_θ Transition Model	12
3.2.5	Moving/Multiple Reference Frame (MRF)	12
3.2.6	All y^+ Wall Treatment	13
3.3	Computational Domain	14
3.3.1	Mesh Generation	14
3.3.2	Mesh Evaluation	17
3.4	Grid Independence Analysis	22
3.5	Validation through Empirical Data	24
3.5.1	Validation with Rudder	24
3.5.2	Validation at Open Water Conditions	26
3.6	Efficient Usage of Computational Power	28
4	Design of PBCF	31
4.1	Definition of Propeller	31
4.2	Geometrical Parameters of PBCF	33
4.2.1	Hub/Boss Cap Geometry	33
4.2.2	Fin Geometry and Definition	35
4.2.3	Fin Profile	37
4.2.4	Fin Installation Position	39
4.2.5	Fin Installation Angle	39
4.2.6	Fin Span	40
4.2.7	Rake Angle	41
4.2.8	Summary of Geometrical Parameters	42
4.3	Rectangular Base PBCF Design	42
4.4	Analysing the Rectangular Base Design	46
4.4.1	Fin Installation Arrangement	46
4.4.2	Hydrofoil Investigation	47
4.4.3	Number of Fins	53
4.4.4	Mirrored	53
4.4.5	Rectangular and Base Design Comparison	55

5	Parameter Study and Optimisation of PBCF	57
5.1	Parameter Study	57
5.1.1	Geometry	58
5.1.2	NACA 4412	60
5.1.3	Installation position	62
5.2	Optimised Design	64
5.3	Performance of the Optimised Design	68
5.3.1	Varying Ship Speed	68
5.3.2	Varying Advance Ratio	69
5.3.3	Yield Strength Analysis	69
6	Conclusion	72
7	Future Works	74
	Bibliography	75
A	Validation of CFD Model	78
B	Visualisation of Investigated Hydrofoils	85
C	Parameter Study Visualisation	88

Chapter 1

Introduction

In recent decades, increasing the efficiency of larger vessels within the shipping industry has gained growing awareness due to the increasing focus on reducing air pollutants and fuel consumption. The Energy Efficiency Design Index (EEDI) enacted by the International Maritime Organisation (IMO) obligated newly manufactured shipping vessels to endorse a minimum energy efficiency level, which accommodates the demand of lessening air pollution by retrenching fuel consumption. The EEDI takes multiple variables into account, such as emissions, shipping capacity, and ship speed. Using a complex formula, the EEDI of a given vessel can thereafter be calculated. The EEDI limit is lowered every fifth year, commenced in 2015, where the regulation baseline was introduced in 2013. The choice of Energy Saving Devices (ESD), which meets the regulation, is left for the manufacturers because of the performance-based mechanism of the EEDI. Therefore, various ESDs have emerged as a consequence of the EEDI, where special attention has been given to implementation, development, and research. [IMO, 2020]

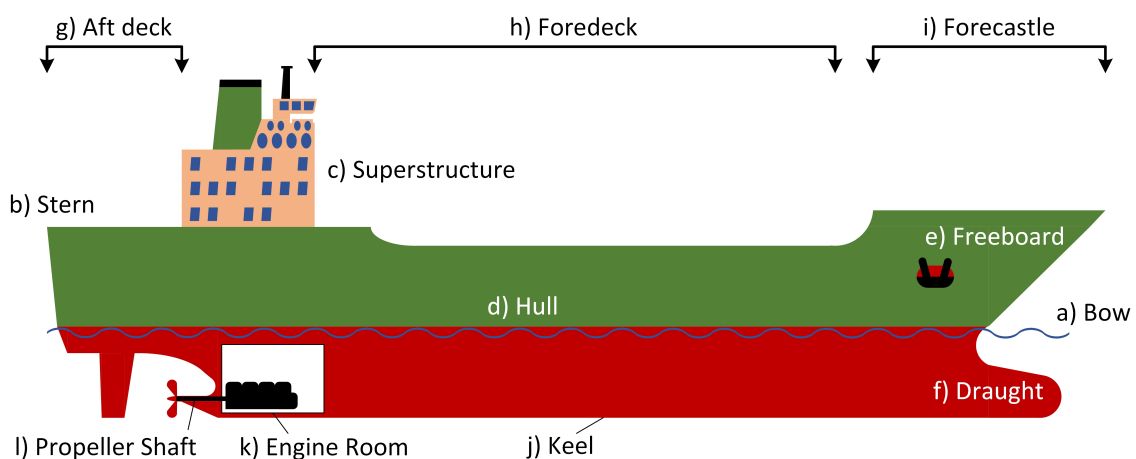


Figure 1.1: Description of the different parts constituting a given vessel.

Depending on the type of transported cargo, different types of shipping vessels can be found through the world's cargo fleet. Though the cargo hold may be different, all the ships are composed of the same basic parts, which are shown in Figure 1.1. In maritime terminology, the front and back end of a given vessel is called the bow and stern, seen respectively at point *a*) and *b*). At the bow, a bulbous bow is shown, which is implemented because of its significant drag-reducing and hydrodynamic improving abilities. The largest vessels throughout the world's shipping fleet have the majority of their space allocated for the specific cargo they transport, yielding minimal space for accommodations. The superstructure seen at point *c*) is implemented for this requirement, which likewise acts as the control or command tower (typically referred to as the bridge). The superstructure is defined as the part of a given vessel that projects above the main deck. This includes other vessels such as sailboats, aircraft carriers, fishing boats, etc. The "shell" of a vessel is called the hull, shown in the figure at point *d*). The hull is partly underwater, as indicated by the figure. The part of the hull, which is

above and below the water surface, is called freeboard and draught, respectively (point *e*) and *f*). The deck of the vessel is shown at point *g*) to *i*), composed of three segments: the aft deck, the foredeck, and the forecastle. All three distinctive decks are used on the largest container ships for transporting containers, including the cargo hold within the hull. The keel shown at point *j*) in the figure is the bottom of the vessel. Just above the keel at the stern of the vessel, the engine room and propeller are located, shown at point *k*) and *l*), respectively. Mechanical energy generated by the engine induces the propeller shaft to rotate, which produces thrust, generating the vessel's forward motion. [Officer of the Watch, 2020] [Engpin, 2015]

Various ESDs can be implemented throughout a vessel, where the bulbous bow shown in Figure 1.1 is just one of a broad selection. The ESDs chosen for implementation can be attached/incorporated onto the hull at different locations, which can be divided into three distinctive regions shown in Figure 1.2. The appropriate region to implement a given type of ESD is determined from the purpose of the specific ESD, where some tend to reduce drag and others to increase the hydrodynamic efficiency of the hull. Some ESDs are implemented upstream of the propeller (Region I), others within the propeller's near vicinity (Region II), and some are lastly implemented from the stern to the propeller's near vicinity (Region III). The devices located in Region I can be implemented to accommodate a more favourable wake to the propeller or to reduce drag. In Region II and III, the devices are typically implemented within the propeller/rudder vicinity, where they may reduce torque upon the propeller shaft or increase thrust by interacting with the slipstreams from the propeller blades.

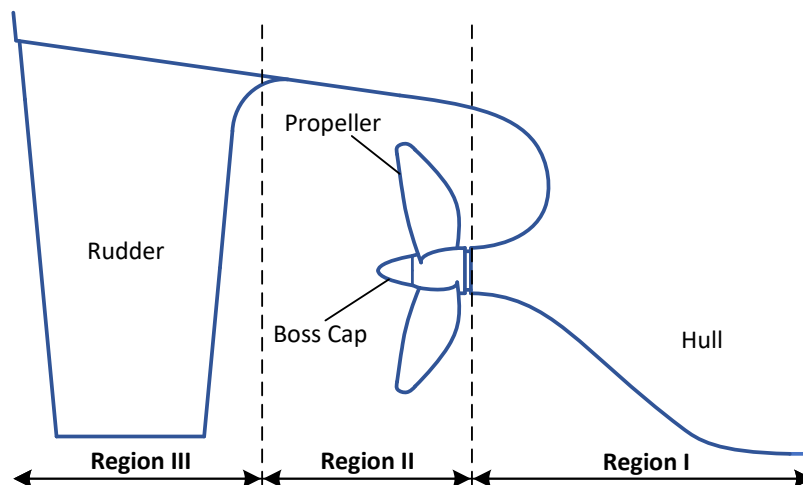


Figure 1.2: ESD region classification.

The EEDI is only mandatory to uphold for newly constructed vessels, as mentioned in the section above. Implementing various ESDs is relatively simple to accomplish upon newly designed vessels, as the vessel is already in dry dock. For already operating vessels, this can become an expensive and time-consuming process due to reduced operating time. Depending on the chosen ESD, the process can likewise become further time-consuming for older vessels, as some ESDs require hull or rudder modification, which can likewise promote mechanical difficulties and further expenditures.

An ESD that does not require vessel modification is the Propeller Boss Cap Fins (PBCF).

The original boss cap of the propeller is directly replaced by this device, which can significantly increase the propeller efficiency and thereby lowers flue gas emissions. Implementing a PBCF reduces or completely breaks up the induced hub vortex generated downstream by the propeller rotation, lowering torque upon the shaft. Likewise, a weakened or destroyed hub vortex will reduce the risk of cavitation upon the propeller and rudder. Installation of the PBCF is inexpensive compared with other ESDs, as they require hull or rudder modification [Seo et al., 2016]. The PBCF are designed and manufactured to utilise the original bolt position used for the boss cap. The implementation process can likewise be done without the need for drydocking, which lowers the operational time and thereby income. This can be achieved underwater while the ship is docking due to the relatively simple installation procedure, [Haun, 2014]. The propeller without the PBCD is shown in Figure 1.3a where a hub vortex is generated as mentioned above. On this particular propeller, the hub vortex is completely eliminated by implementing the PBCF instead of a regular boss cap, which is visualised in Figure 1.3b.

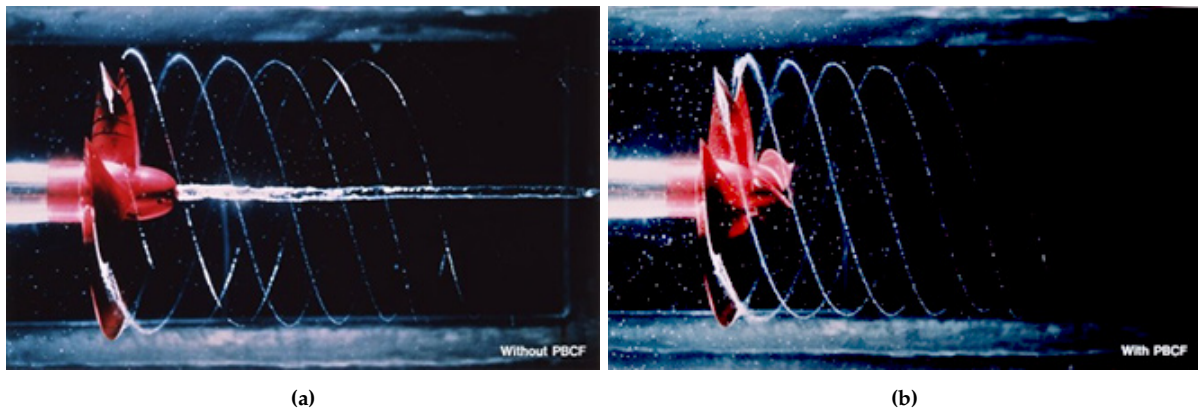


Figure 1.3: (a) without implementation of PBCF and (b) with implementation of PBCF. [MOL Techno-Trade, 2015]

One company that researches and develops ESDs and integrated propulsion systems is the international corporation MAN Energy Solutions Frederikshavn, located in Frederikshavn, Denmark. In recent years their primary focus within the ESD sector has been integration, research, and development of the so-called Rudder Bulb (RB). By implementing RB, the propulsion efficiency can be increased, lowering the flue gas emissions of a given vessel. MAN Energy Solutions Frederikshavn is interested in the less expensive method of increasing efficiency by implementing PBCF, which in addition to other ESDs, can accommodate the EEDI requirements. Therefore, this thesis will focus on the design, optimisation, and simulation of the PBCF for a given propeller/rudder system to obtain an optimised solution for efficiency increase.

1.1 State of the Art

The hydrodynamic behaviour of the induced hub vortex downstream of a propeller and boss cap has been a known fact for several decades. After the discovery of cavitation and tearing upon the rudder, prompted by the hub vortex, research and development on weakening the vorticity field were commenced. The Japanese company Mitsui O.S.K. Lines, the West Japan Fluid Engineering Laboratory Co., and Mikado Propeller Co. developed and patented a new invention explicitly designed to weaken or even eliminate the hub vortex generated down-

stream. The manufacturing company claims to have installed more than 3,000 PBCF [MOL Techno-Trade, 2015] on the world's shipping fleet since they patented their invention in 1987. In the paper by Ouchi et al. [1988] the inventors conclude based on a vast amount of empirical data that an increase in propeller efficiency of up to 7 % and approx. 2 % self-propulsion efficiency increase could be expected by implementing PBCF. The inventors discuss in their patent the inexpensive and straightforward design and implementation procedure regarding PBCF and conclude that the PBCF could become an excellent ESD in the future [Ogura et al., 1987].

The authors describe in their patent that three conditions should be followed to satisfy an efficient fin design: the number of fins should equal the number of propeller blades, the diameter of the PBCF should not exceed 33 % of the propeller diameter, and the difference between installation angle and propeller blade root pitch angle should be kept between -20° and 30° [Ogura et al., 1987]. In the paper by Hsin et al. [2008], the authors examine various geometric PBCF parameters by applying potential flow boundary element analysis. They found that the diameter of the PBCF should be kept within 20-25 % of the propeller and states that the two most critical parameters in their analysis are the installation and rake angle (referred to as the pitch and installation angle in their paper, respectively). Little attention has been given to the number of fins, and it appears that the researchers have implemented an equal number of fins as propeller blades based on previous studies regarding the subject. After analysing the effect of altering the geometry by applying the potential flow boundary element method, the authors conduct a RANS investigation to more accurately obtain the effect of implementing PBCF on efficiency. Analysing two individual propellers the authors gained an increase of 1.4 % and 1.6 % in propeller efficiency by implementing PBCF.

In a study by Lim et al. [2014] where the authors' focus is examining the design parameters and hub cap, it was found that the propulsion efficiency of the given vessel was underestimated by 1.4 % to 2 % when comparing open water CFD analysis to open water experimental investigation. Both the numerical simulation and the empirical tests were conducted at model-scale, and the results obtained showed similar tendencies as previous research regarding PBCF. The authors conclude that the most critical parameters for PBCF design are the installation angle and the chord-span ratio, which is in agreement with Ouchi et al. [1988].

In the work of Mizzi et al. [2017], the authors validate a model RANS CFD open water analysis against experimental data. In previous research, the different PBCF parameters are determined and varied individually, without taking their interaction into account, leading to inaccurate results. The authors discuss that analysing each parameter individually and neglecting their interaction can result in local optimums instead of global optimums. The authors' research suggests an automated optimisation technique, which effectively, quickly, and easily maximises the outcome of a given system to yield the best design of the PBCF. The resulting PBCF design was afterwards tested at full-scale using RANS methods, yielding an efficiency gain of 1.3 % compared to the case without PBCF. The authors discuss that previous studies have achieved a higher increase in efficiency, but these studies were conducted at model scale, which is claimed by Mizzi et al. [2017] to be the reason. They discuss that evaluating the designed PBCF in full-scale takes the physically highly turbulent behaviour into account, where the model scale investigation will move the testing media towards the more unrealistic laminar region. The authors discuss that empirical scaling effects could possibly account for this, which is claimed to be inapplicable or inaccurate in certain cases. The study,

therefore, concludes that the analysis and final evaluation of implemented PBCF should be done at full-scale to account for the testing media's hydrodynamic behaviour.

Constructing a CFD model which approximates the hydrodynamic and physical occurrences most realistically requires that the meshing of the system domain is considered carefully. The approach of meshing a propeller system is discussed by Gaggero [2018], where the author utilises *snappyHexMesh* and *OpenFOAM* to generate the mesh and CFD simulation, respectively. Here an automated optimisation algorithm is formulated, which varies different PBCF geometrical parameters. These are applied to *snappyHexMesh* and simulated in *OpenFOAM*, where the results are alternated automatically by the optimisation algorithm to obtain an optimised PBCF design yielding the highest efficiency gain. The author examines the algorithm with two distinctive propellers, KP505 and E779A, resulting in an efficiency increase of 0.9 % and 4 %, respectively. The author claims that the higher efficiency gain in the latter is due to its older design, which he discusses is less hydrodynamically refined. The domain size was found sufficient with $4D_p$ (propeller diameter) in the radial direction, $4D_p$ downstream, and $2D_p$ upstream. Because of the open water condition and the periodic rotation of the propeller, the chosen simulated domain is a cylindrical sector of 90° , as the propeller consists of four blades. The simulated domain is chosen as it drastically reduces calculation time. In the study by Mizzi et al. [2017], the authors simulate the entire 360° cylindrical domain with a seven times larger cell size than Gaggero [2018]. The authors chose to simulate the entire domain as they did not reach their limit regarding the available computational power. The coarseness of the mesh was analysed to investigate its effect on efficiency. From the three mesh coarseness analysed, the results showed minor influence upon the efficiency though the finest mesh of 1.0×10^7 cells was chosen nevertheless.

In the paper by Kawamura et al. [2012] the cylindrical sector boundary domain were likewise utilised, where a single blade and fin passage is simulated using RANS. This work focuses on analysing the propeller and PBCF system at model- and full-scale Reynolds numbers. The Reynolds number is kept constant for each of the two propellers analysed, where the rpm is varied to accommodate the changing diameter from model to full-scale. By comparing the simulations, an efficiency increase of about 5 % could be seen when the conditions were changed to full-scale analysis. The authors assumes that the increase was partly due to the greater boss drag at full-scale, which amplifies the reduction made by the PBCF, triggering a larger increase in efficiency. It was likewise investigated if different inflow conditions (wakefields) would affect the efficiency, which was concluded to be insignificant. It was noticed that the increased efficiency due to PBCF implementation was primarily due to the blade configuration. The authors conclude that a 2.32 % and 2.05 % efficiency increase for the two propellers respectively were achieved and states that the possible minimum efficiency gain of 4 % claimed by the PBCF inventors were not achievable.

In a study by Hansen et al. [2011], the authors conducted model-scale experiments on an Aframax tanker, which afterwards were compared to full-scale tests after the model-scale experiments showed promising results. The full-scale tests were performed with and without implementing PBCF within four days. It was concluded that a decrease of 3.7 % in power consumption was achieved in the full-scale testing of the vessel, which were in excellent accordance with the model-scale experiments yielding 3.8 %. Their research further discusses the importance of vessel fouling, which according to the authors, can significantly impact efficiency. They emphasize that the experiments should be conducted within the first year after

the vessel is docked, as fouling can contribute up to a 5 % increase in power consumption each year. Fouling is most commonly due to the accumulation of algae, microorganisms, and plants on the hull during long-time operation in the shipping industry.

PBCF is typically designed with regards to an existing propeller, where the interaction between the propeller and PBCF is neglected. In the research by Hao-peng et al. [2013], the propeller and PBCF are examined as a complete system, alternating the propeller geometry as well as the PBCF's synchronously to obtain a more significant interaction between the two components and yielding a more efficient propeller design in the process. The authors conclude that the proposed method achieves a higher efficiency gain than the conventional way of designing PBCF.

Information regarding previous numerical studies is stated in Table 1.1. From the table, it is evident that some authors are more clear in the configuration of, e.g. the number of cells or the y^+ chosen. Two different approaches regarding the simulated domain are seen, where some simulate the entire propeller, and others chose to simulate only one blade passage due to lack of availability of computational power. Different adaptations of the domain size are chosen, but nearly all the researchers have implemented the same turbulence modelling approach. An investigation of the modelling options will be presented in Chapter 3, with regards to dis- and advantages.

Table 1.1: Various numerical studies' information regarding simulation options.

Author	Domain	Number of cells	Turbulence model	Near-wall modelling	y^+
Ghassemi et al. [2012]	-	-	-	Neumann kinematic boundary condition Kutta condition	-
Kawamura et al. [2012]	Single blade passage $4D_p, 10D_p, 6D_p$	1.3×10^6	SST $k-\omega$	-	-
Lim et al. [2014]	Entire propeller $2D_p, 4D_p, 3D_p$	-	SST $k-\omega$	-	-
Katayama et al. [2015]	Entire propeller	3.2×10^7	SST $k-\omega$	Tetrahedral and prismatic cells	1
Druckenbrod et al. [2015]	-	-	SST $k-\omega$	-	-
Mizzi et al. [2017]	Entire propeller $2D_p, 5D_p, 3D_p$	9.2×10^6	SST $k-\omega$	All- y^+ treatment approach	model-scale: <1 full-scale: >30
Gaggero [2018]	Single blade passage $2D_p, 4D_p, 4D_p$	1.2×10^6	SST $k-\omega$	Wall Functions Prism layer extrusion	avg. $\simeq 30$

A summary of various researchers' chosen geometrical PBCF parameters and their range is stated in Table 1.2. Here 11 studies regarding PBCF are conducted from 1988-2018. If a parameter has been analysed in one of the studies, but the investigated range or measure is not specified, the parameter will be marked with a "v". The research listed in the table includes both numerical and empirical analyses together with model- and full-scale investigations. As seen in the table, some parameters have been researched in multiple studies, indicating a more significant influence of the given parameter. With a basis in the table, a starting point for the sizing of the geometrical PBCF parameters used for further optimisation in the project will be evaluated. The applied geometrical parameters of PBCF mentioned in Table 1.2 are illustrated in Figure 4.5 on page 36. The terminology regarding the specified parameters is by some authors inconsistent with the terminology utilised through this project, which in the table has been altered to fit this project.

Table 1.2: Researchers' chosen PBCF parameters and range.

Author	Advance Ratio	PBCF Diameter	Axial Position	Circumferential Position	Hub Diameter	Phase Lag	Fin Chord Length	Camber	Slope Angle	Installation Angle	Rake Angle	Efficiency Gain
Ouchi et al. [1988]	0-1.1	0.09-0.175 D_p	0-0.08 D_p	<0.07 D_p			0.09 D_p , 0.12 D_p			45-105°	± 30°	≤ 7 %
Hsin et al. [2008]		0.2D-0.25 D_p	<0.025 D_p							v	v	1.4-1.64 %
Hansen et al. [2011]	0-1.0											≈ 3.5 % ¹⁾
Chassemi et al. [2012]		0.33 D_p	v		v	v			0-15°	v		Increase
Kawamura et al. [2012]	0.3-0.9											1.48-2.32 %
Lim et al. [2014]	0.0-1.0	0.28-0.31 D_p							-12(-6)°	61.5-71.5°	± 10°	1.4-2 %
Katayama et al. [2015]	0.45-0.7	v			v	v	v		v		v	0.69-1.28 %
Druckenbrod et al. [2015]	v	v				v	v	v	v	v		4-6 % ²⁾
Seo et al. [2016]	0.1-0.9	v				0-60°	0.078-0.14 D_p			32-56°		1.6 %
Mizzi et al. [2017]		v				0-71°	0.053-0.11 D_p			± 50°		1.3 %
Gaggero [2018]	0.4-1.1	0.25-0.45 D_p	0.05-0.20 D_p			-45-40°	0.07-0.15 D_p	-0.015-0 D_p		30-60°		0.9, 4.0 %

1) Fuel Efficiency, 2) of D_p

Chapter 2

Problem Statement

How can CFD be utilised to optimise the efficiency of a propeller/rudder system by implementing and optimising propeller boss cap fins, and to which extent?

Assumptions and Limitations

MAN Energy Solutions Frederikshavn provides empirical data for the use of validating the computational model. It is assumed that these have been conducted in a correct way since the authors have had no influence on the creation of these.

Chapter 3

Theory and Validation of Computational Model

Through this chapter, the numerical theory regarding the computational model will be stated. An introduction and analysis of the computational domain will be conducted, to evaluate the quality and reliability of the model. Lastly, will a comparison between the empirical and the obtained numerical data be performed to ensure a valid model.

Empirical data and CAD drawings of a four-bladed propeller for a Ro-Ro ship is provided by MAN Energy Solutions Frederikshavn, as mentioned in the preface. The drawings contain a model scale propeller which is illustrated in Figure 4.1 on page 31 along with the attached rudder.

3.1 Ship Propeller Terminology

To establish an understanding of the commonly used terminology regarding propellers, equations defining the hydrodynamic behaviour will be stated. These are based on the propeller's thrust and torque, which will be non-dimensionalised to obtain a simple way to compare the results with other researchers.

The speed of the propeller compared to the surrounding free stream fluid is non-dimensionalised with the advance coefficient, which is used in both aero- and hydrodynamics. The definition is as follow:

$$J = \frac{V_A}{N \cdot D_p} \quad (3.1)$$

The definition of the thrust coefficient is as follow:

$$K_T = \frac{T}{\rho_\infty \cdot N^2 \cdot D_p^4} \quad (3.2)$$

The definition of the torque coefficient is as follow:

$$K_Q = \frac{Q}{\rho_\infty \cdot N^2 \cdot D_p^5} \quad (3.3)$$

The definition of the propeller efficiency is as follow:

$$\eta_o = \frac{J \cdot K_T}{2\pi \cdot K_Q} = \frac{T \cdot V_A}{2\pi \cdot Q \cdot N} \quad (3.4)$$

The definition of the pressure coefficient is as follow:

$$C_P = \frac{p - p_\infty}{0.5 \rho_\infty V_\infty^2} \quad (3.5)$$

where V_A is the propeller advance speed, N is the rotation of the propeller per second, D_p is the diameter of the propeller, T is the thrust, ρ_∞ is the density of the freestream flow, Q is the torque, p is the pressure, p_∞ is pressure of the freestream flow, and V_∞ is the velocity of the freestream flow.

3.2 Numerical Methods

The governing equations in the implemented models will be stated in this Section 3.2. The most common form of the equations will be utilised to ensure a clear understating of the information. The denominations and symbols used in the section might not be in coherence with what is used in the preceding and following sections and will not be stated in the nomenclature.

The simulations are conducted in steady-state where the RANS (Reynold-Averaged Navier-Stokes) solver have been utilised. The solver provides high accuracy to the needed computational power and is thus often used for similar setups. The segregated flow solver, SST $k-\omega$ and γ - Re_θ model have been chosen for the governing of the flow separation and turbulence. These models have been chosen based on the models used throughout the literature as stated in Table 1.1.

3.2.1 Reynolds-Averaged Navier–Stokes (RANS)

When describing turbulent flow, the RANS turbulence models are commonly used. It was first introduced by Reynolds [1895] and advances compared to the DNS and LES in the lower required computational power. The model is formulated from the Navier-Stokes equations, which describe incompressible fluid flow. The velocity of the fluid is divided into two components containing a fluctuating and time-average part, which are denoted u' or \bar{u} , respectively. The governing equations are formulated in Equation (3.6) and (3.7) for incompressible Newtonian fluids, where the last segment $(-\rho\overline{u'_i u'_j})$ of Equation (3.6) is denoted the Reynolds stress. This term needs to be further specified to complete the RANS equation, which can be archived by the formulation of turbulence models, such as the SST $k-\omega$ model. Maulik et al. [2020]

$$\rho\bar{u}_j \frac{\partial \bar{u}_i}{\partial x_j} = \rho\bar{f}_i + \frac{\partial}{\partial x_j} \left(-\bar{P}\delta_{ij} + \mu \left(\frac{\partial \bar{u}_i}{\partial x_j} + \frac{\partial \bar{u}_j}{\partial x_i} \right) - \rho\overline{u'_i u'_j} \right) \quad (3.6)$$

$$\frac{\partial \bar{u}_i}{\partial x_i} = 0 \quad (3.7)$$

where ρ is density, f is an external force vector, P is pressure, δ is a Kronecker delta function and μ is dynamic viscosity.

3.2.2 Segregated Flow Model

The segregated flow model and coupled flow model are two solvers that are used for solving similar problems. These both have pros and cons regarding convergence and computational resources. The coupled flow model solves the conservation equations simultaneously for momentum, mass, and energy, while the segregated model solves the equations separately. This results in more memory needed for the coupled solver. The segregated model is generally recommended by STAR-CCM+ as the first choice for incompressible flows where shocks, high Mach numbers, or high Rayleigh numbers are not present. Both solvers should be adequate

for the purpose of this project, but the segregated solver with a first-order upwind scheme is found most applicable. This is based on an extensive comparison between the first- and second-order segregated and coupled flow solver with empirical data. The empirical data is presented later in the project on page 25 and is used to validate the model. The comparison between the different schemes and models is present in Appendix A on page 78.

3.2.3 Shear Stress Transport k - ω Turbulence Model

The turbulence model SST k - ω was proposed nearly three decades ago by Menter [1994] and is still used in the present time with some additions. It is a blend that combines the strength of the k - ω and k - ϵ model. The k - ϵ was the first developed model and is highly capable of accounting for turbulent flow but becomes inaccurate in the near-wall region. The inaccuracy is produced by a damping function and increased as the wall distance is decreased. The k - ω model was developed to account for this error by defining the model without damping functions. This model is accurate in the near-wall region but is highly sensitive to turbulent conditions defined at the inlet of a domain, which is often difficult to define accurately. A blend of the two models with respect to the wall distance was developed, resulting in the SST k - ω model, which combines the advantages of both models.

The specific dissipation rate and turbulent kinetic energy is stated in Equation (3.9) and (3.10), respectively. These are established from the k - ϵ and k - ω model, which is formulated similarly, though with the addition of the term stated in the following equation, which only appears in the k - ϵ model:

$$2\sigma_{\omega 2} \frac{1}{\omega} \frac{\partial k}{\partial x_i} \frac{\partial \omega}{\partial x_i} \quad (3.8)$$

By multiplying $(1 - F_1)$ and varying F_1 between 0 and 1, to this segment, a seamless blend between the two models is achievable. In the near-wall region where the k - ω is most capable, a F_1 value close to 1 is used and lowered towards 0 as the wall distance is increased and the k - ϵ models are more capable. The initial model gained from this is referred to as the k - ω BST model (Baseline Stress Transport) and gave improved overall results compared to the original models but over-predicted the wall shear stress. This was accounted for by introducing a limiter to the near-wall viscosity, where separation is more likely to happen and shear stress is significant. Equation (3.11) describes this viscosity limiter where a max function is taken advantage of by multiplying the significant shear stress (S) with a blending function (F_2). The SST k - ω model is highly reliable and has proven so due to the nature of the blending functions and the viscosity limiter function.

For this project, the SST k - ω model is the most suitable turbulence model due to the high accuracy in evaluating flow separation under adverse pressure gradients and prediction of the onset of the flow. The good prediction in the near-wall flow is very relevant in this study, and the model has been used in all published research on the subject (see Table 1.1).

Specific dissipation energy:

$$\frac{\partial \omega}{\partial t} + u_j \frac{\partial \omega}{\partial x_j} = \alpha S^2 - \beta \omega^2 + \frac{\partial}{\partial x_j} \left((v + \sigma_{\omega} v_T) \frac{\partial \omega}{\partial x_j} \right) + (1 - F_1) 2\sigma_{\omega 2} \frac{1}{\omega} \frac{\partial k}{\partial x_i} \frac{\partial \omega}{\partial x_i} \quad (3.9)$$

Turbulent kinetic energy:

$$\frac{\partial k}{\partial t} + u_j \frac{\partial k}{\partial x_j} = P_k - \beta^* k \omega + \frac{\partial}{\partial x_j} \left((v + \sigma_k v_T) \frac{\partial k}{\partial x_j} \right) \quad (3.10)$$

Viscosity limiter:

$$v_T = \frac{a_1 k}{\max(a_1 \omega, SF_2)} \quad (3.11)$$

3.2.4 γ - Re_θ Transition Model

For the flow transition between the laminar and turbulent boundary layer, the γ - Re_θ transition model is often adopted. The transport Equations (3.12) and (3.13) are similar to the equations of the k - ω model with some alterations. Empirical correlations have been used to determine the constants in the source terms of the model. The turbulence intermittency (γ) and the momentum thickness Reynolds number (Re_θ) are the two primary focus points of this model. The local turbulence is resembled by γ between 0 and 1, indicating fully laminar or turbulent, respectively. In turbulent conditions when $\gamma = 1$ the equations are equal to the SST k - ω model.

Whether a flow is in the laminar, transition or turbulent zone is possible to determine on a simple geometry like a flat plate, based on the distance from the leading edge, but it can be impossible to determine it in a similar way on more complex geometries like a propeller. The momentum thickness Reynolds number Re_θ can instead be defined to describe the flow's local velocity profile and momentum, which can be used to define the percentage of fully laminar or turbulent flow, from 0 to 1, respectively.

Intermittency:

$$\frac{\partial \rho \gamma}{\partial t} + \frac{\partial (\rho U_j \gamma)}{\partial x_j} = P_\gamma + E_\gamma + \frac{\partial}{\partial x_j} \left(\left(\mu + \frac{\mu_f}{\sigma_f} \right) \frac{\partial \gamma}{\partial x_j} \right) \quad (3.12)$$

Transport momentum thickness Reynolds number:

$$\frac{\partial \overline{Re_{\theta t}}}{\partial t} + \frac{\partial (\rho U_j \overline{Re_{\theta t}})}{\partial x_j} = \overline{P_{\theta t}} + \frac{\partial}{\partial x_j} \left(\sigma_{\theta t} (\mu + \mu_t) \frac{\partial \overline{Re_{\theta t}}}{\partial x_j} \right) \quad (3.13)$$

where,

$$P_\gamma = F_{length} c_{a1} \rho S (\gamma F_{onset})^{0.5} (1 - c_{e1} \gamma) \quad (3.14)$$

$$E_\gamma = c_{a2} \rho \Omega \gamma F_{turb} (1 - c_{e2} \gamma) \quad (3.15)$$

3.2.5 Moving/Multiple Reference Frame (MRF)

The formulation of a moving reference frame is implemented when part of a body is rotating. It is performed by applying a rotation to a sub-domain surrounding the part of interest. By doing this, an interpolation algorithm is needed to compensate for the cells next to the rotating and stationary mesh not lining up.

Furthermore, a rewriting of the cell velocity is needed to compensate for the rotation. The velocity is instead defined as a relative velocity to the moving reference (u_r), the angular velocity of the rotation (Ω), and the distance from the rotation axis (r), as stated in Equation

(3.16). This formulation replaces the velocity formulated in the Navier-Stokes equation for all the cells in the MRF. By doing so, additional source terms are need in regards to Ω and r , though this will not be elaborated further.

$$u = u_r + \Omega \times r \quad (3.16)$$

3.2.6 All y^+ Wall Treatment

Due to the no-slip condition, a steep velocity gradient is present in the near-wall region. A fine mesh is needed in this region in order to resolve the gradient, which is often done by refining the mesh as the distance to the wall is decreased. A piecewise-linear approach was originally used to refine the mesh in this area but was eventually replaced by wall functions, which lowers the needed number of cells and thus computational time. The wall functions rely on non-linear functions, which enables the use of larger cells with similar results. Figure 3.1a illustrates the difference between these two methods.

These non-linear wall functions are formulated from DNS simulations and empirical experiments, where the non-dimensionalised wall distance y^+ , stated in Equation (3.17), is used as a reference for the tangential velocity of the flow. Figure 3.1b illustrate the subdivision of the boundary layer into the viscous sub-layer, the buffer layer, and the log-law region. Based on empirical data, two wall function have been defined describing the viscous sub-layer and the log-law region $y^+ < 5$ and $30 < y^+$, respectively. These two functions are accurate in their respective zone, but lags in the buffer layer zone as the y^+ gets further away from the design value ($y^+ < 5$ and $30 < y^+$). A blend between the two is a prevalent method when defining wall functions on the basis of the y^+ .

The all y^+ wall treatment mixes the low y^+ and the high y^+ wall treatment. The low y^+ wall treatment is applicable when a refined mesh and low Reynolds numbers are present. For the most accurate results, a $y^+ < 1$ is preferable for a well resolved viscous sub-layer. The high y^+ wall treatment is meant for a coarser mesh in the region were $30 < y^+ \lesssim 100$. By combining these, it can be expected to get accurate results in a wide range of y^+ and thus it is chosen to be used in this study, where torque and thrust coefficients are of interest. The ability to resolve the viscous sub-layer on the propeller surface is essential, and $y^+ \approx 1$ will be advantageous, allowing the software to exploit this method fully.

Non-dimensional wall distance:

$$y^+ = \frac{u^* y}{\rho_\infty} \quad (3.17)$$

Friction velocity:

$$u^* = \sqrt{\frac{\tau_\omega}{\rho_\infty}} \quad (3.18)$$

Non-dimensional velocity:

$$u^+ = \frac{u}{u^*} \quad (3.19)$$

where u^* is the friction velocity measured at the nearest wall, y is the distance to the nearest wall, ρ_∞ is the density of the freestream fluid, u is the local velocity, and τ_ω is the wall shear stress.

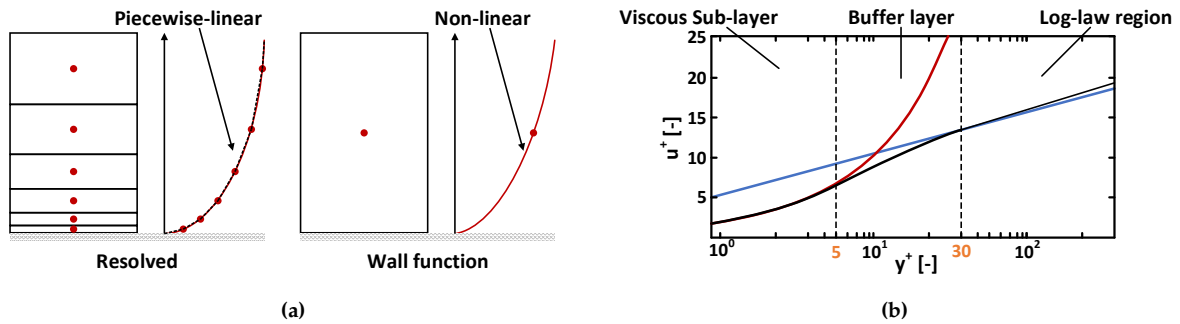


Figure 3.1: Wall treatment methods where (a) the difference between resolved mesh and wall function and (b) the three near-wall layers.

3.3 Computational Domain

A computational domain in the shape of a cylinder is defined for the propeller. The dimensions of the cylinder extends $6D_p$ downstream and $3D_p$ upstream with a radius of $4D_p$, which is based on the literature study summarised in Table 1.1. For the modelling of the propeller, a small rotating cylinder is defined with the measures of $0.29D_p$ downstream and $0.6D_p$ upstream with a radius of $0.6D_p$. The concentric cylinders will be denoted Outer Domain and MRF Domain for future references, as shown in Figure 3.2.

The left side of the Outer Domain is defined as a velocity inlet, while the corresponding outlet (right side) is defined as a pressure outlet, where the static pressure is defined. The cylinder sides are defined as walls with slip. From the inlet to the propeller is a stationary shaft defined as shown.

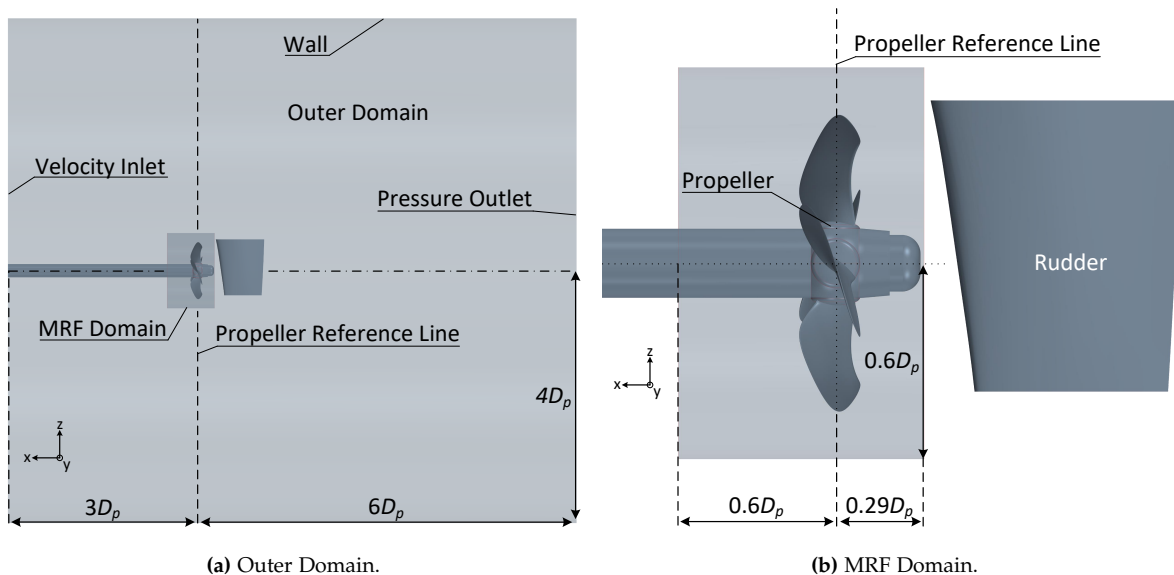


Figure 3.2: The two computational domains with dimensions specified.

3.3.1 Mesh Generation

The generation of the mesh in STAR-CCM+ is computed by choosing the desired meshing models and determining a reference “Cell Base Size” for each domain. The meshing models determine how the mesh is generated while the base size is used as a reference when determining other mesh properties, like the maximum cell size or prism layer thickness. The same meshing models are chosen for the MRF and Outer Domain, though different base sizes have been chosen. The following meshing models have been chosen.

- Trimmed Mesher
- Surface Remesher
- Prism Layer Mesher

Trimmed Mesher

The Trimmed Mesher, which is first applied, covers the entire domain in a template mesh consisting of hexahedrons of equal size. The hexahedrons in the near-wall region are subdivided into smaller hexahedrons when approaching a wall to account for the shape of a geometry. The speed of the sub-division is controlled by a volume growth rate which defines the minimum number of cells of equal size that is needed before the cell size can be subdivided again. A value of 1, 2, 4, or 8 cells of similar size before a subdivision can happen can be chosen here, where a higher value naturally results in a more refined mesh. Three of the levels are shown in Figure 3.3 where the level with 8 layers is the one chosen for the project. Lastly, the hexahedrons are trimmed or cut in the areas near the surface if needed to represent the part correctly. Polyhedrals in the form of hexahedrons with a corner missing are thus formed next to the surface, which represents the surface more accurately. This results in a domain predominantly consisting of hexahedrons in the free stream and polyhedral in the near-surface zone. A high-quality grid with low cell skewness can be expected to be created by this method.

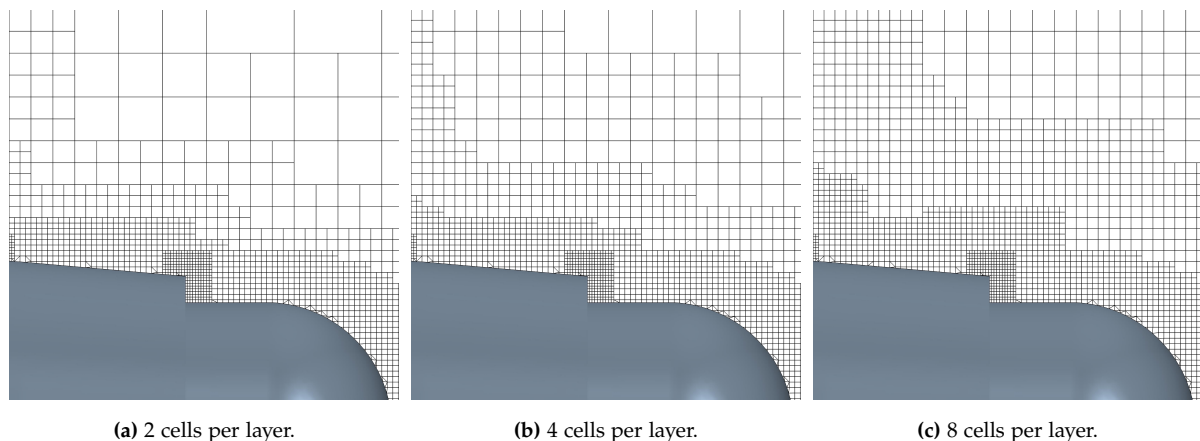


Figure 3.3: Trimmed Mesher with three different number of layers per subdivision.

Surface Remesher

The Surface Remesher is often recommended in combination with the Trimmed Mesher to account for the meshing of the surface. The entire surface is triangulated by reforming the hexahedrons with a corner missing into tetrahedrons which are able to represent the surface more accurately. The accuracy is based on user-defined quality requirements, which increases the number of surface cells as the requirements are increased. These includes the accuracy of the surface curvature, defined by the number of points around a circle that would be used to define it or the surface growth rate which defines the maximum increase in area from one cell to another. The propeller blade and hub before and after the Surface Remesher is shown in Figure 3.4, where the surface with the Surface Remesher shows a refined mesh consisting of triangles.

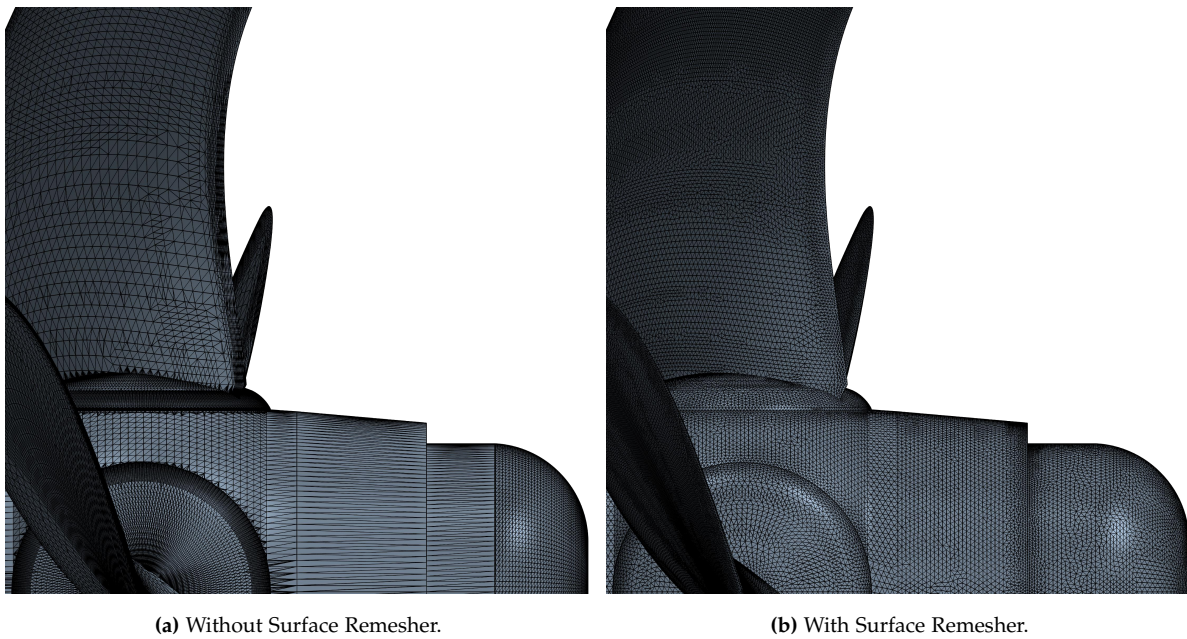


Figure 3.4

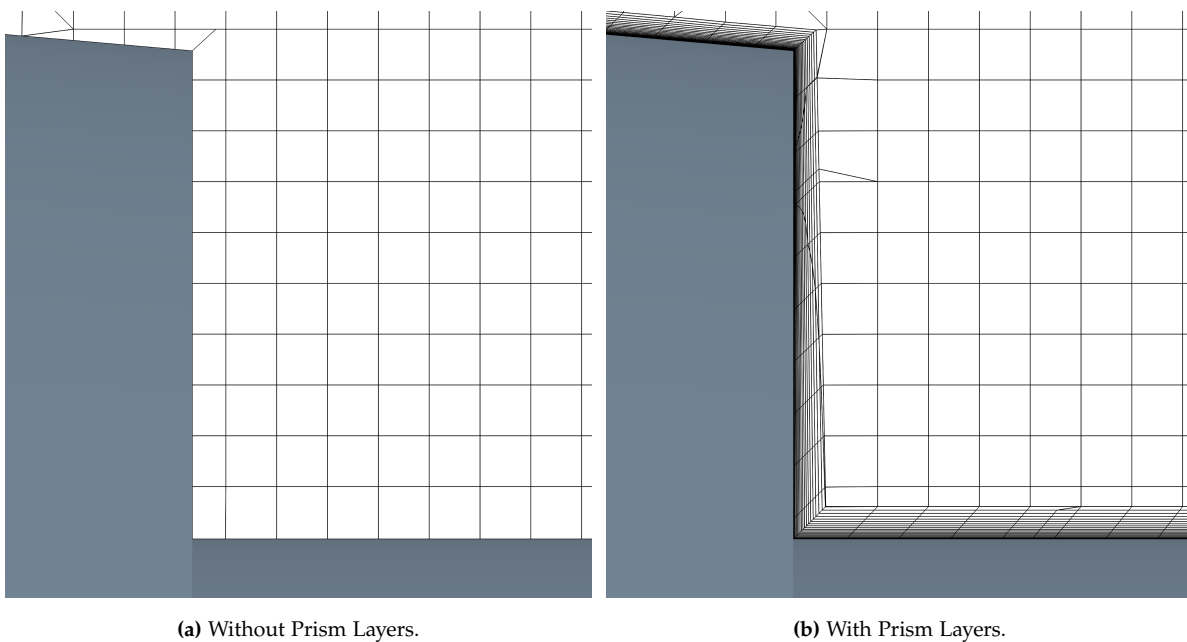


Figure 3.5

Prism Layer Mesher

The Prism Layer Mesher allows for a decreasing cell size in the near-wall region. This is done by creating cell layers orthogonal to the wall with a fixed growth rate for each layer of cells. The cell size is thus increased as the distance to the wall is increased. This is essential for resolving the near-wall region accurately, especially when flow separation is likely to happen. The prism layers are defined by three characteristics; thickness, number of layers, and growth rate. The number of layers is by default set to 6 and a growth rate of 1.5 in STAR-CCM+.

Figure 3.5 show the difference between having prism layers or not, where 16 prism layers and a growth rate of 1.1 is chosen in Figure 3.5b. It can be observed how the near-wall region is much better resolved when the prism layers are applied. The volume increase from the last prism layer cell to the neighbouring non-prism layer cell do not follow the normal recommended growth rate and a smoother transition would be more appropriate.

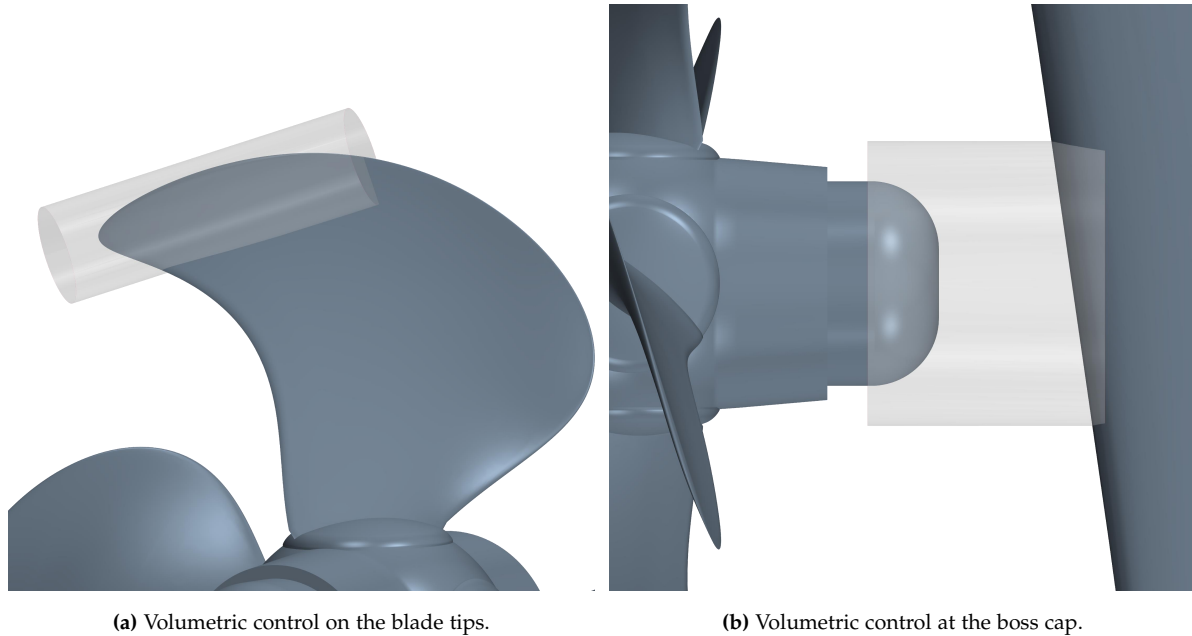


Figure 3.6: Volumetric controls.

Volumetric Controls

Volumetric controls can be implemented in defined areas where a more refined mesh is needed. It is possible to refine the surface mesh and/or the volume mesh, which are advantageous in areas where small geometries are present, or flow separation is likely to occur, respectively. For this application, flow separation is most likely to happen at the propeller tips. In Figure 3.6a volumetric controls in the shape of cylinders are placed at fin tips to account for this. Higher residuals are observed downstream of the boss cap, which has been resolved by implementing a volumetric control here as shown in Figure 3.6b. The volume refinement is here chosen to be 10 % of the general mesh in this domain.

A method of locating the cells with the highest residuals and refining the mesh accordingly have been used to determine the most appropriate meshing values while limiting the total number of cells. A comparison is presented in Appendix A on 80 where the cells with the highest residuals are shown for the model with the default settings and the settings present in Table 3.1.

3.3.2 Mesh Evaluation

The generated mesh presented in the previous section will now be evaluated to determine the quality of the mesh. This can be done through a great variety of parameters where the following five will be in focus:

- Cell y^+

- Cell Skewness
- Cell volume ratio
- Residuals
- Steadiness

The y^+ , skewness angle and cell volume ratio gives a great insight into the quality of the mesh and have thus been stated in Table 3.2

Table 3.1: Chosen values for mesh generation.

Number of cells, MRF	1.15×10^7
Number of cells, Outer	2.66×10^6
Cell base size, MRF	$8.7 \times 10^{-2} D_p$
Cell base size, Outer	$1.0 \times 10^{-1} D_p$
Volume growth rate	8 cells pr. layer
Points in surface curvature	36
Surface growth rate	1.1
Prism layer thickness	$8.7 \times 10^{-4} D_p$
Number of prism layers	18
Prism layer growth rate	1.1

Table 3.2: Mesh quality values.

Average y^+ on blades	0.39
Range of y^+ on blades	1.9×10^{-2} to 1.7
Average skewness angle	1.1°
Max skewness angle	88.5°
Average cell volume ratio	0.98
Min cell volume ratio	9.65×10^{-5}

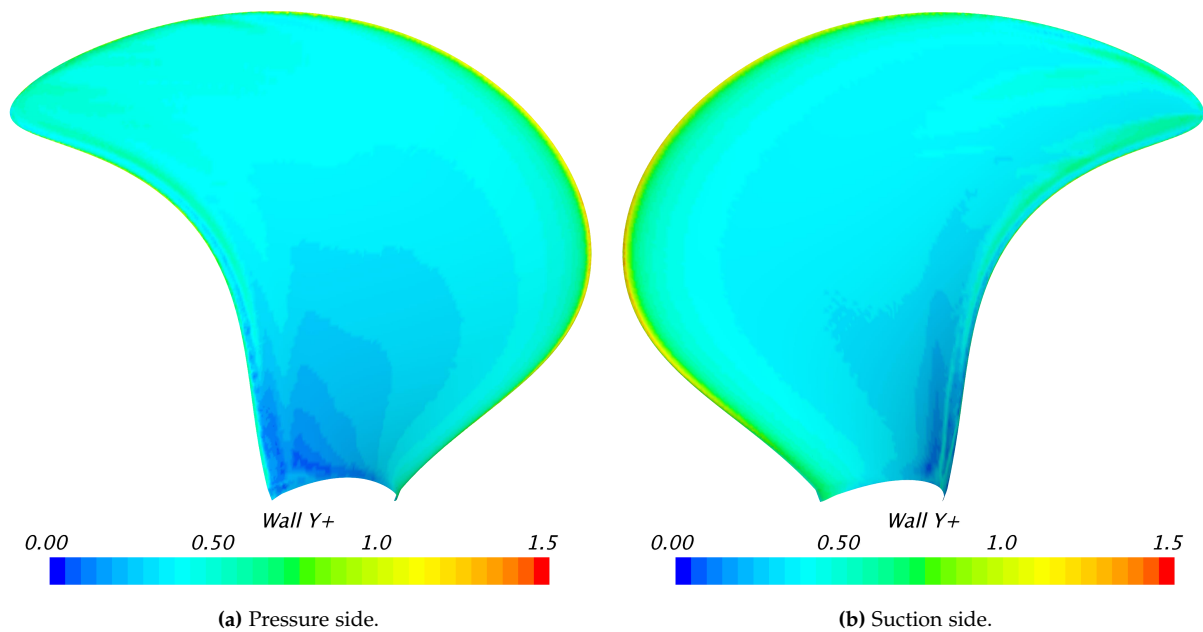


Figure 3.7: y^+ on one propeller blades.

Value of y^+

The importance of a low y^+ have been emphasised in previous sections, but it is essential to accurately model the near-wall flow, especially if flow separation is likely to happen. The maximum $y^+ = 1.7$ on the blades are below the commonly recommended value of 5. The

average value of 0.39 is adequate for this kind of model where flow separation and cavitation are likely to happen. The distribution on the pressure and suction side of one of the blades is shown in Figure 3.7. The value increases towards the tip of the blades but is generally at a value below 1, as were stated in the table.

Skewness Angle

The skewness angle is measured from the angle that is formed from a vector connecting two cell centroids and the face normal vector, as shown in Figure 3.8a. An angle of 0° indicates a perfect orthogonal mesh, while an angle greater than 90° indicates concave cells. STAR-CCM+ generally recommends a value below 85° to get a robust and good quality mesh. The maximum value at 88.5° is above the recommended value and indicates that at least one cell is above the recommended value of 85° . These cells have been located and illustrated in Figure 3.8b, where it can be observed that the cells are primarily located at the trailing edge of the rudder. This is expected due to the sharp edge of the rudder and the fact that it is located outside of the MRF Domain, where coarser mesh is present. Due to the location of the cells and the high average value, this is considered appropriate.

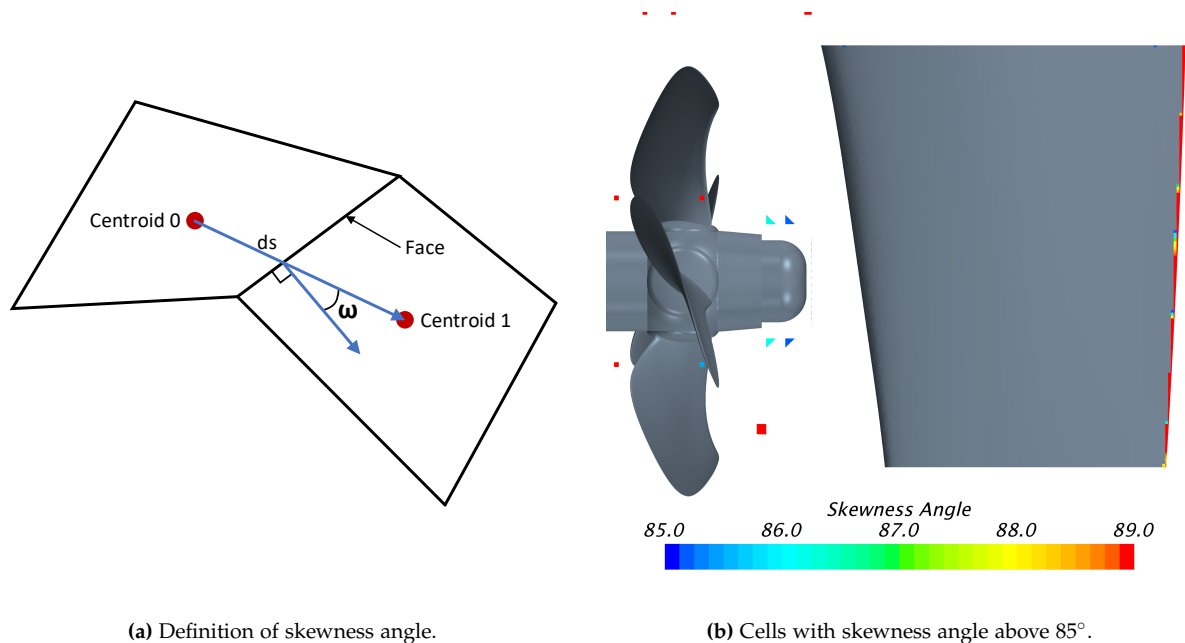
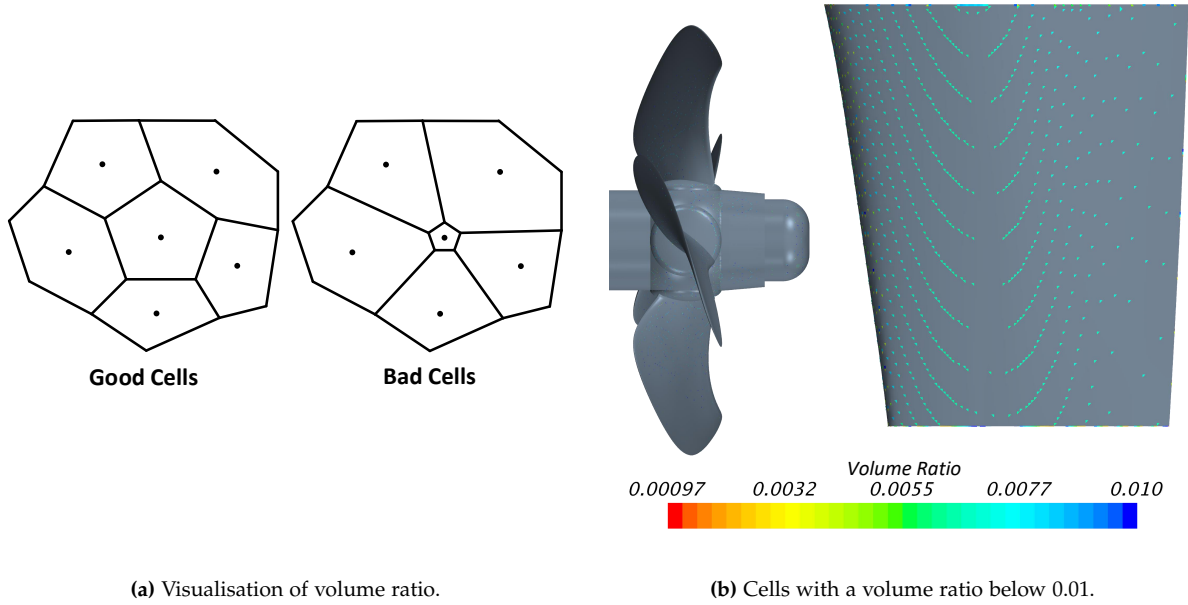


Figure 3.8: Skewness angle.

Volume Ratio

The cell volume ratio describes the volume of a cell compared to its largest neighbour, see Figure 3.9a. The value is between 0.0 and 1.0, where 0.4 as an example would indicate that the cell volume is 40 % of the largest neighbouring cell and 1.0 indicates that the cell volume is equal to or greater than any neighbouring cells. STAR-CCM+ does not recommend values below 0.01 due to potential of instability and inaccuracy in the solvers. The average value is close to 1 and the lowest value is 9.65×10^{-5} , which indicates that at least one cell is below the recommended value. The cells with a value below the recommend 0.01 have been located and is illustrated in Figure 3.9b. It can be observed that the cells are primarily located at the side of the rudder due to it being located outside of the MRF Domain, where a coarser mesh is

located. This is considered acceptable due to the propeller being the primary interest and the fact that most of the cells are close to the recommended value.



(a) Visualisation of volume ratio.

(b) Cells with a volume ratio below 0.01.

Figure 3.9: Volume ratio.

Residuals

The residuals are a measure of how well the discretised equations are satisfied. The residuals for all the variables would be equal to zero in a completely converged solution. A low number is thus always preferable as this results in reliable and stable values. The definition of residuals can vary between programs but is in STAR-CCM+ showcased as normalised global residual as default. The value is normalised to easier compare the residuals against each other. The presented residuals are calculated as follow:

$$Res_{pres} = \frac{Res_{rms}}{Res_{norm}} \quad (3.20)$$

$$Res_{rms} = \sqrt{\frac{1}{n_{cell}} \sum_{n_{cell}} r^2} \quad (3.21)$$

$$Res_{norm} = \max(|R_1|, |R_2| \dots |R_5|) \quad (3.22)$$

where Res_{pres} is the residuals value presented in the residuals window, which normally assume a value between 0 and 1 for a converging model due to the normalisation. Res_{rms} is the root mean square value of the residuals in all the cells in the domain, where n_{cell} is the total number of cells and r is the absolute error in each cell. Res_{norm} is the normalisation factor that takes the maximum residual from the first five iterations. More iterations can be used, but STAR-CCM+ commonly recommends five.

Based on the chosen models, eight variables are possible to monitor as shown in Figure 3.10. It is commonly recommended to have a value below 10^{-3} for which have been achieved in this case. The highest values are intermittency and continuity, which regards turbulence

and conservation of mass, respectively. The momentum in the X, Y and Z direction follows next where the X is slightly higher, probably due to it being in the flow direction. Tke (turbulence kinetic energy), Sdr (specific dissipation rate) and $Re_{\theta t}$ (governs transition), follows next.

The variables can be observed to decrease as the iterations number increase, which is expected for a steady-state simulation. The simulation seems to reach a steady point at 500 to 600 iterations, and for the following 400 iterations, only a slight decrease is observed.

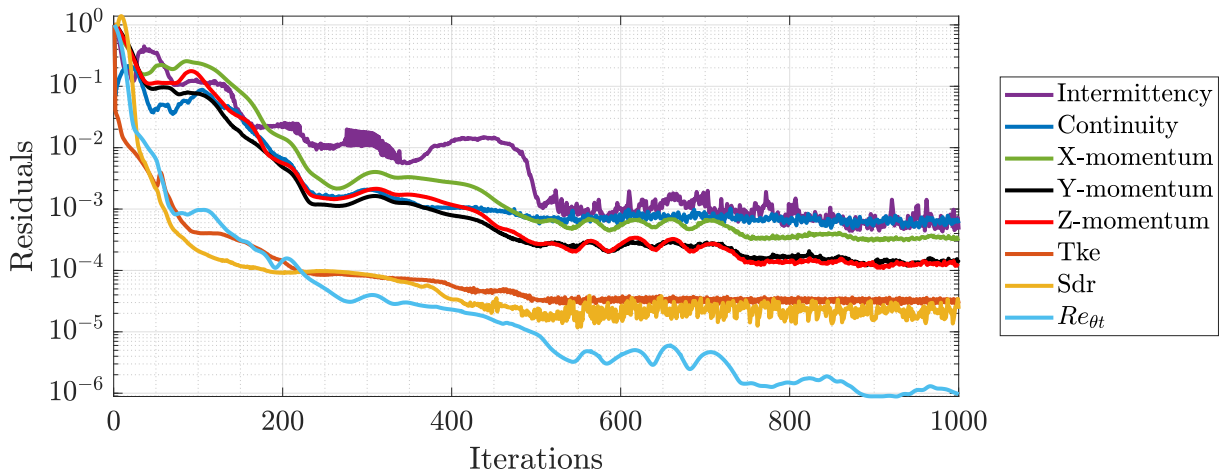


Figure 3.10: Normalised global residuals over 1000 iterations as the simulation stabilises.

Steadiness

For steady-state simulations, a constant value after a certain amount of iterations is expected if the correct models have been chosen and the meshing is done correctly. The development of the thrust and torque of the blade is shown in Figure 3.11. Here an unstable value can be observed for the first couple of iterations while a converged value is reached as the model progresses through the 1000 iterations.

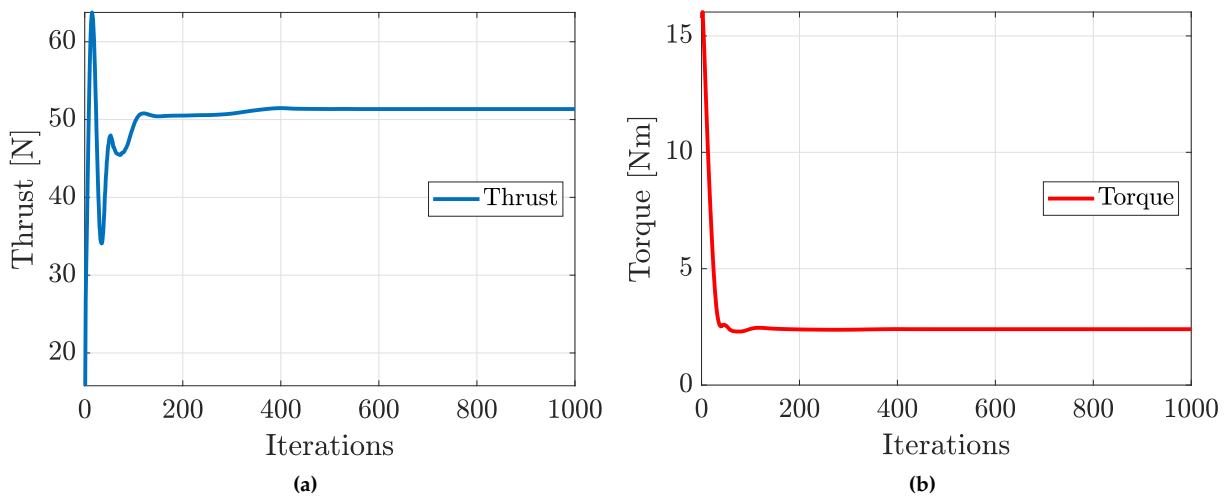


Figure 3.11: Stabilisation over 1000 iterations of (a) thrust and (b) torque.

The average, minimum, and maximum value for the last 100 iterations are stated in Table 3.3. A deviation of 0.002 % and 0.001 % compared to the average value is achieved, indicating that the model has reached a steady-state.

Table 3.3: Values of the last 100 iterations for the thrust and torque.

	Thrust	Torque
Average value	51.3521 N	2.40142 Nm
Minimum value	51.3516 N	2.40140 Nm
Maximum value	51.3526 N	2.40144 Nm
Deviation	0.001	3×10^{-5}
Deviation	0.002 %	0.001 %

3.4 Grid Independence Analysis

In the book by Roache [1998] a method is presented for determining an appropriate number of cells in any simulation by studying the effect of changing the total number of cells. Three simulations referred to as fine, medium, and coarse, with different number of cells are needed for the approach. The number of cells should be halved in each spacial direction when comparing the fine to medium, and medium to coarse, for a good setup. The cylindrical shape of the domain in this study does not allow for that kind of control in each direction, but the total number of cells will instead be used as the reference. The number of cells can be altered by changing the “base size” for the cells in the MRF- and Outer Domain equally. Due to the three dimensions of the domain, an increase of 2^3 is needed when the mesh is refined.

Through the iterative process described in Section 3.3.1 a mesh with a cell number of 1.4×10^7 have been generated. This will be considered as the fine grid, with the corresponding medium and coarse grid of 1.75×10^6 and 2.2×10^5 cells, respectively. The generated mesh on the surface of the blades is shown in Figure 3.12, while the total number of cells with other mesh-related properties for the three setups are stated in Table 3.4.

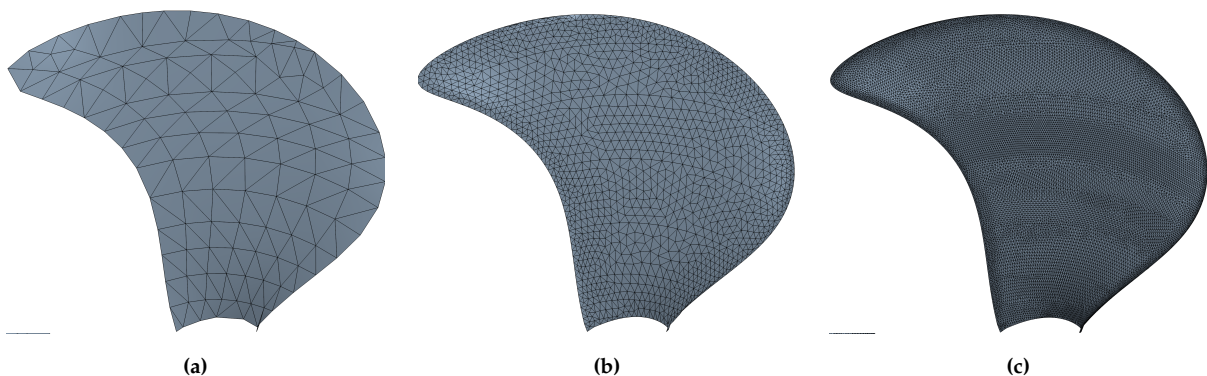


Figure 3.12: The mesh formation on the blade when varying the number of cells. Here (a) coarse grid, (b) medium grid and (c) fine grid.

Table 3.4: Setup for the three models used in the Roach grid independence analysis.

	Coarse	Medium	Fine
Total number of cells	2.20×10^5	1.75×10^6	1.41×10^7
Cells in MRF Domain	1.38×10^5	1.49×10^6	1.15×10^7
Cells in Outer Domain	8.44×10^4	2.60×10^5	2.66×10^6
Average y^+ on blades	3.12	0.41	0.39
Range of y^+ on blades	0.47 to 40	0.029 to 1.9	0.019 to 1.7
Average skewness angle	9.4°	7.6°	1.1°
Max. skewness angle	100°	89.9°	88.5°
Average cell volume ratio	0.87	0.89	0.98
Min. cell volume ratio	2.16×10^{-5}	4.20×10^{-5}	9.65×10^{-5}

A low y^+ and skewness angle, and a volume ratio close to 1.0 is always preferable. It can be observed that these values are worsening as the number of cells is increased, and the mesh gets coarser. It is noted that the average y^+ for the coarse mesh increases to a 3.12 which is below 5, but the range is increased to a value of 40. This is commonly not recommended but is acquired due to the low cell number. The skewness angle and volume ratio follows the same trend with worsened values as the mesh gets coarser. The coarse mesh would probably not be recommended for any reliable data but is solely used for the Grid Convergence Index (GCI) test.

The three models are now constructed, and at least one decisive parameter is needed to determine the order of convergence. This is done by comparing it between the three simulations and determining what value it is converging towards as the number of cells increases. The torque and thrust are chosen for this study as these are essential for analysing the propeller.

An index called GCI is introduced by Roache, which represents a percentage the simulated value is from the value obtained when the total cell number goes towards infinity. Richardson extrapolations are used in the GCI calculations, where a GCI values close to zero will be present if the fine grid is in the vicinity of the converged value. The shape of the domain complicates the use of the original approach proposed by Roache, as mentioned previously, thus a newer approach by Celik [2008] is used. This is based on the original approach but is able to analyse non-ideal cell distribution. The method of the GCI equations and the estimation of the converged value will be present by the following equations:

The convergence order:

$$P = \frac{1}{\ln(r_{21})} \left(\left| \ln \left(\left| \frac{\epsilon_{32}}{\epsilon_{21}} \right| \right) + q(P) \right| \right) \quad (3.23)$$

$$q(P) = \ln \left(\frac{r_{21}^P - S}{r_{32}^P - S} \right) \quad (3.24)$$

$$S = \text{sign} \left(\frac{\epsilon_{32}}{\epsilon_{21}} \right) \quad (3.25)$$

where r is a cell volume ratio between the medium/fine and coarse/medium grid, and ϵ is a ratio between thrust and torque coefficient. The number 1-3 indicates the fine, medium, and coarse grid, respectively.

The converge value is determined from the order of convergence and the value of the coefficient for the fine and medium grid by the use of Richardson extrapolation.

$$K_{ext,21} = \frac{r_{21}^P K_1 - K_2}{r_{21}^p - 1} \quad (3.26)$$

where the thrust coefficient is represented by K .

The approximate relative error, the extrapolated relative error, and the GCI of the fine grid are determined in the respective order:

$$e_{a,21} = \left| \frac{K_1 - K_2}{K_1} \right| \quad (3.27)$$

$$e_{ext,21} = \left| \frac{K_{ext,21} - K_1}{K_{ext,21}} \right| \quad (3.28)$$

$$GCI_{fine}^{21} = \frac{1.25e_{a,21}}{r_{21}^p - 1} \quad (3.29)$$

The values of the uncertainties and the GCI are stated in Table 3.5 for the fine grid.

Table 3.5: Grid convergence index based on the torque and thrust for the fine grid.

	K_T	K_Q
Order of convergence, P	1.3	2.6
Relative error, e_a	3.8 %	1.4 %
Extrapolated relative error, e_{ext}	1.5 %	0.1 %
Grid Convergence Index, GCI	1.9 %	0.2 %

A low relative error and extrapolated relative error indicate that the fine grid should result in valid data independent of the number of cells. The values in Table 3.5 are considered acceptable due to the low values along with the low GCI value. The GCI of 1.9 % for the K_T is higher than for K_Q which shows that the torque is less influenced by the number of cells than the thrust is. A value of 1.9 % is still acceptable and proves that the simulation with the fine grid is independent of the grid and results in a converged value. Further reduction of the cell size could result in a lower GCI, but it is considered superfluous to do so.

3.5 Validation through Empirical Data

MAN Energy Solutions Frederikshavn has conducted two model scale experiments with the propeller. One experiment was performed at open water conditions, while the other was performed with a rudder attached downstream. From the data collection of the experiments the torque, thrust, and efficiency were calculated and will be used for the validation of the computational model.

3.5.1 Validation with Rudder

For the experiment with the rudder attached, a varying ship speed (V_S) and rotational velocity of the propeller have been utilised. This has been performed so that the advance ratio of the propeller has been kept similar for the varying ship speed. The same conditions have

been simulated in the computational model to make a comparison. The torque and thrust coefficient, and the efficiency are shown in Figure 3.13a and 3.13b, respectively. The deviation between the experiments and simulations shown in the figure are stated in Table 3.6 for further examination. When comparing the experiments and simulations, a good correlation are present for the range of ship speeds. The deviation for both K_T and K_Q increases as the ship speed increases reaching a maximum deviation of 1.9 % and 2.3 %, respectively. However, the deviation for η_o is below 0.5 % for the full range indicating that the increase in both K_T and K_Q is similar. The efficiency is the primary design factor for the following design and optimisation of PBCF, and a low deviation will ensure good accuracy and validity of the results. Based on the trend presented in the figure and the deviations stated in the table, the computational model is considered appropriate for simulations with a rudder attached.

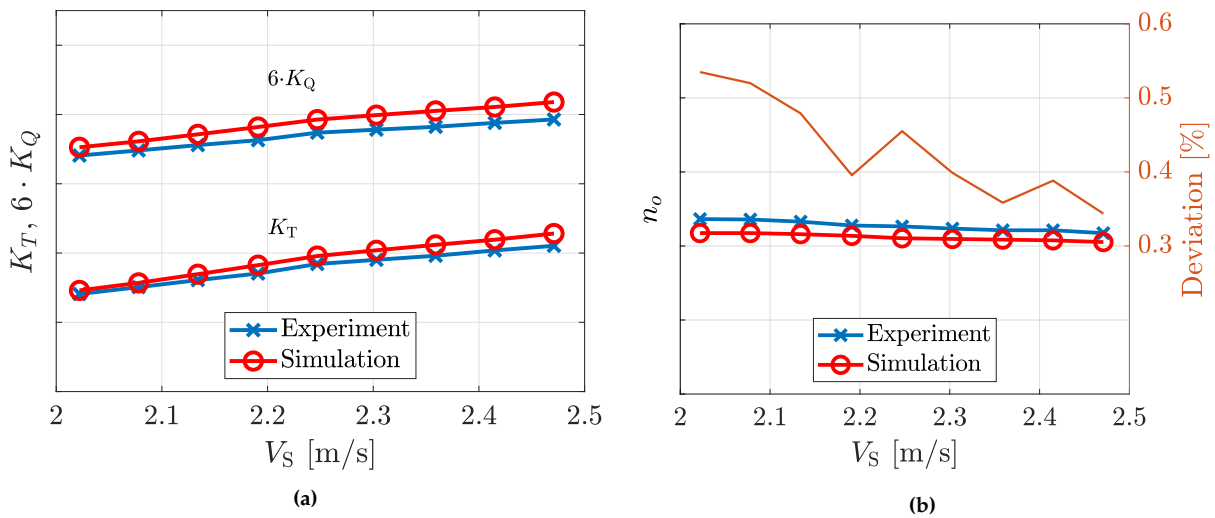


Figure 3.13: Comparison between experiments and simulations with an implemented rudder at a varying ship speed for (a) torque and thrust coefficient and (b) efficiency.

Table 3.6: Deviation between simulation and experiments shown in Figure 3.13.

V_S [m/s]	2.02	2.08	2.13	2.19	2.25	2.30	2.36	2.42	2.47
K_Q [%]	1.1	1.2	1.5	1.8	1.8	1.9	2.1	2.1	2.3
K_T [%]	0.6	0.7	1.0	1.4	1.3	1.5	1.8	1.7	1.9
η_o [%]	0.5	0.5	0.5	0.4	0.5	0.4	0.4	0.4	0.3

Pressure coefficient contour plots of the propeller and rudder are presented in Figure 3.14. These are created from the simulation with a water inflow speed of 2.25 m/s. Through these figures, zones with low- and high-pressure are visualised. A low-pressure zone directly downstream of the boss cap is present in Figure 3.14c, while a high-pressure zone occurs both above and below, along the leading edge of the rudder. This influences the pressure acting on the propeller blades, which can be seen in Figure 3.14b. Here the upper blade has a higher C_p value than the other blade, which is a result of the inclined rudder with a smaller distance in the upper portion. The low-pressure zone transpire $2D_p$ downstream of the propeller as seen in Figure 3.14d. The shape of the propeller blades and boss cap creates a vortex downstream

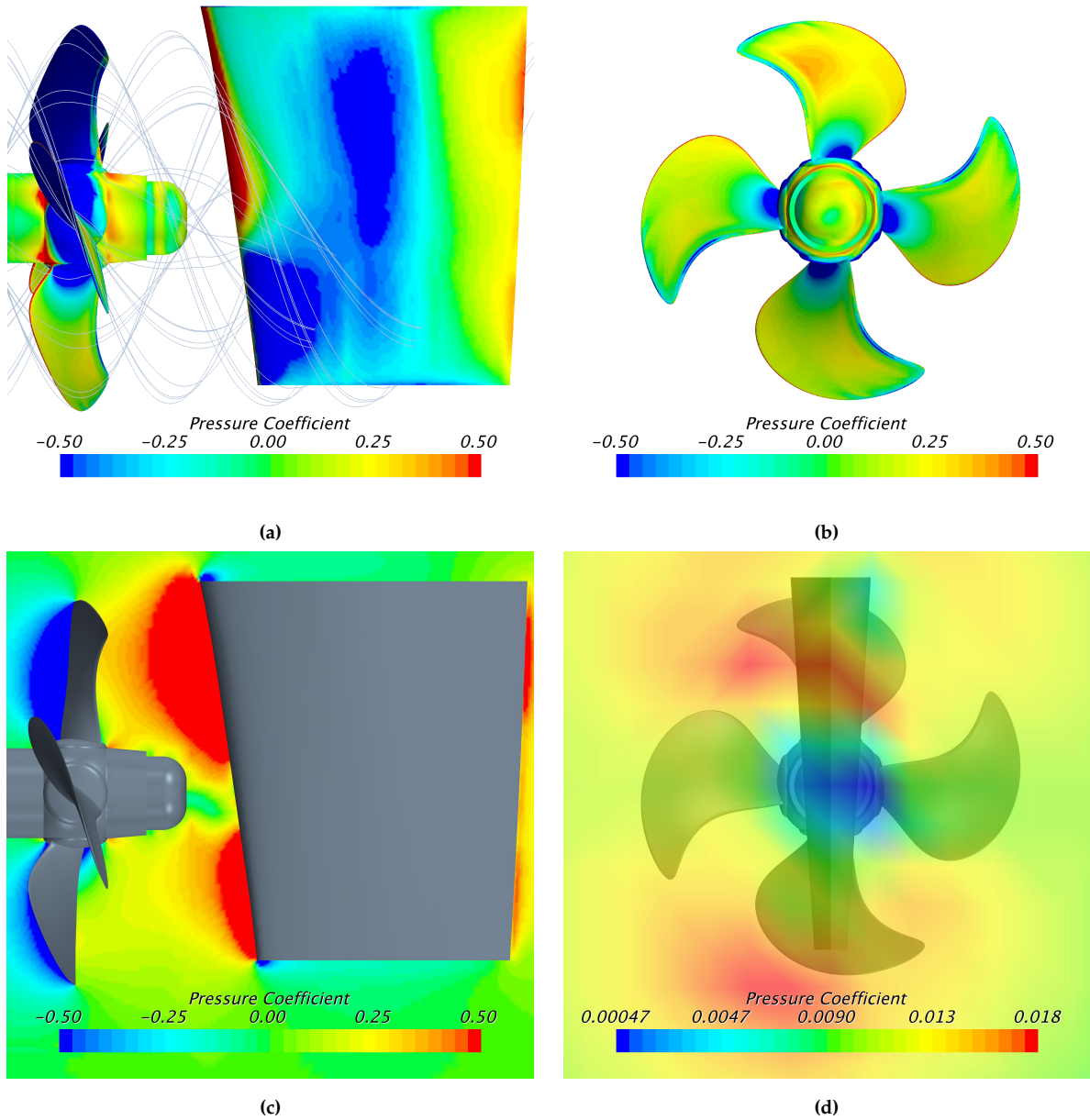


Figure 3.14: C_p contour plots on or around the propeller and rudder, with the water flow from left to right with an inflow speed of 2.25 m/s and rotation 10.13 rps. Where (a) side view, (b) downstream without the rudder, (c) side view contour of flow, and (d) pressure plane of flow $2D_p$ downstream of propeller, note a different pressure coefficient range.

of the boss cap, creating this low-pressure zone. Implementation of PBCF on the boss cap should reduce the formation of the vortex and improve the overall efficiency.

3.5.2 Validation at Open Water Conditions

Experiments at open water conditions have been conducted as well. No rudder is attached, and the shaft is connected downstream of the propeller to obtain an uninterrupted upstream flow. An advance ratio range from 0.3 to 1 have been obtained by keeping a constant rotational velocity at $N = 20$ rps of the propeller while altering the inlet velocity of the water. The

experiments and simulations is shown in Figure 3.15 while the deviation is stated in Table 3.7. The K_Q has the lowest deviation in the middle of the advance ratio range, while a greater deviation occurs in both ends of the range. The opposite trend is present for the K_T where the lowest deviations appears at the edge of the range, and a greater deviation is occurring in the centre of the range. This results in a deviation of η_o that is stable but overshoots approximately 2 to 2.5 % for the entire range. The deviation of the efficiency for the open-water simulations is greater than when the rudder is attached but is still considered acceptable due to the low and stable value. The open water conditions will not be used later when designing the PBCF but are solely included to validate the computational model.

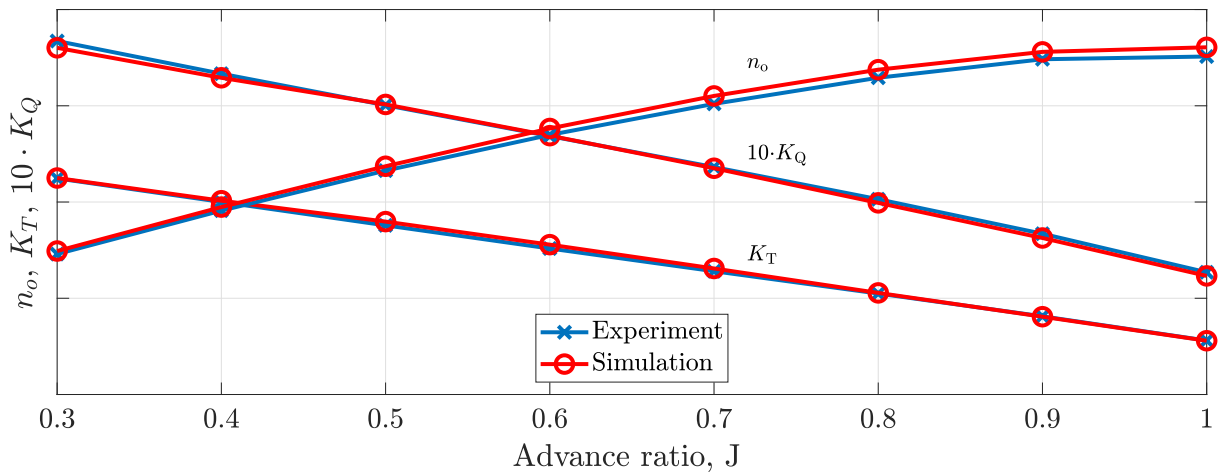


Figure 3.15: Comparison between experiments and simulations of the efficiency, thrust, and torque coefficient determined at open water condition with a varying advance ratio.

Table 3.7: Deviation between simulation and experiments shown in Figure 3.15.

J [-]	0.3	0.4	0.5	0.6	0.7	0.8	0.9	1.0
K_Q [%]	-1.9	-1.3	0.3	0.2	-0.5	-1.9	-2.6	-3.0
K_T [%]	0.2	0.6	2.2	2.6	2.2	0.6	-0.5	-0.3
η_o [%]	2.1	1.9	1.9	2.5	2.7	2.5	2.2	2.7

C_p contour plots for the open water simulation with $J = 0.6$ is shown in Figure 3.16. The tendencies are similar to the simulation with the rudder attached. A significant difference is present in the area downstream of the propeller, which is not affected by the rudder. A low-pressure zone is similarly formed in the centre downstream as shown in Figure 3.16c and is sustained $2D_p$ downstream as shown in Figure 3.16d. Unlike with the rudder attached, small low-pressure vortex form at the blade tip and travel downstream.

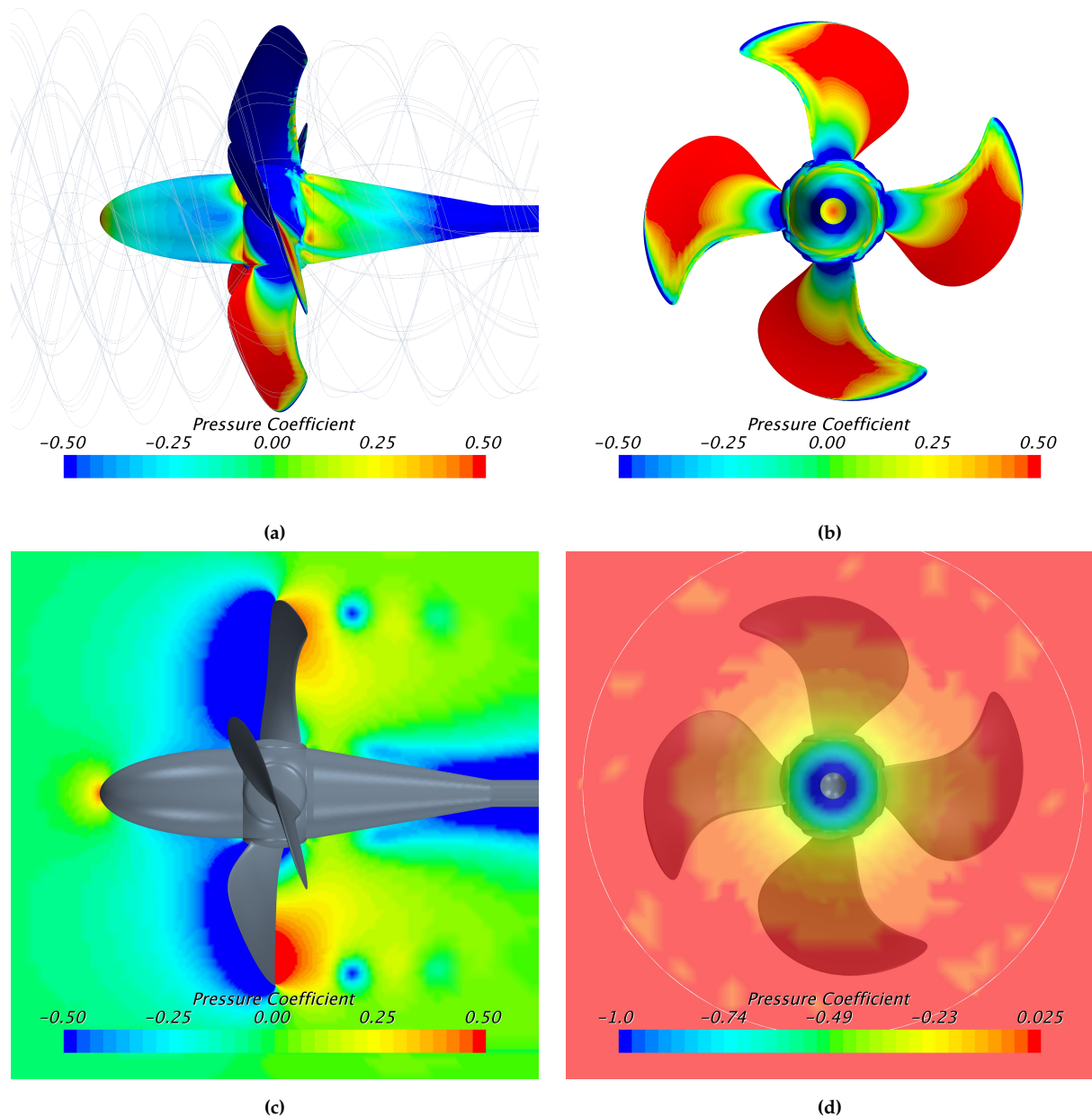


Figure 3.16: C_p contours plots on or around the propeller and rudder, with the water flow from left to right with an inflow speed of 3.20 m/s, rotation 20.0 rps and advance ratio of 0.7. Where (a) side view, (b) downstream without the rudder, (c) side view contour of flow, and (d) pressure plane of flow $2D_p$ downstream of propeller, note a different pressure coefficient range.

3.6 Efficient Usage of Computational Power

The cluster available for the study consists of 15 processors with 12 cores each and 12 processors with 20 cores each, equalling 420 cores total. This cluster is shared with one other student project at MAN Energy Solutions Frederikshavn and should thus be utilised appropriately. A limited number of STAR-CCM+ licenses are shared by all employees using other clusters, and the usage of these should thus be limited.

To determine an appropriate number of cores for a specific job the calculation time com-

pared to the number of cores and number of cells are investigated. The result of this are shown in Figure 3.17 and in Table 3.8 where the minute values are stated. This is done by varying the total number of cells in the model and simulating it for 1000 iterations. The model has been simulated with a varying number of cells, on an increasing number of cores from 20 to 160 by steps of 20. It can generally be observed that the time to complete the simulation decreases as the number of cores increases. When inspecting the model with 1.6×10^7 cells, the simulation time at 20 and 40 cores are 209 and 118 min, respectively. The simulation time is thus decreased by 44 %, though the number of cores is doubled. A new sub-domain is created for each core, which causes additional communication time between each sub-domain that the computational domain is divided into. When the number of cores is doubled to 80 cores the simulation time equals 71 min, which is a decrease of 40 % compared to the simulation time with 40 cores.

Thus, increasing the number of cores decreases the total simulation time, but the total computational time is increased each time additional cores are added. For the current model with 1.4×10^7 cells, a number of cores between 20-80 will be used. When a great number of simulations (10+) is to be simulated, 40 cores for each will result in the fastest results if a sufficient number of licenses are available, while a greater number of cores will be used if fewer models are to be simulated.

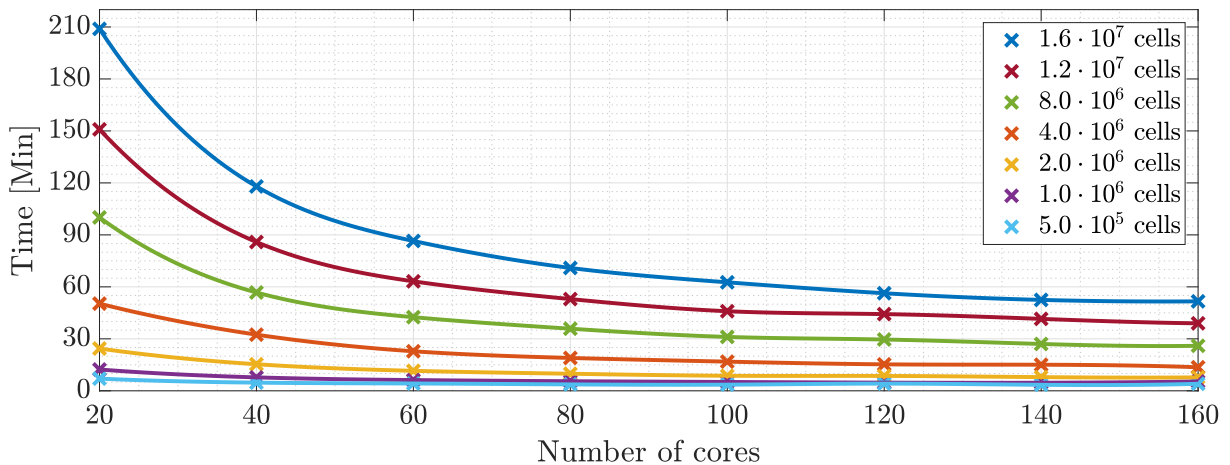


Figure 3.17: Total simulation time for generating mesh and simulating 1000 iterations, with respect to the number of cores used.

Table 3.8: The computational time in minutes shown in Figure 3.17.

Cells	Cores							
	20	40	60	80	100	120	140	160
1.6×10^7	209	118	86	71	63	56	52	52
1.2×10^7	151	86	63	53	46	44	42	39
8.0×10^6	100	57	43	36	31	30	27	26
4.0×10^6	50	32	23	19	17	15	15	14
2.0×10^6	24	15	12	10	9	9	8	8
1.0×10^6	12	8	6	6	5	5	5	5
5.0×10^5	7	5	4	4	4	4	3	4

A computational model is now created and validated based on computational errors and experimental data. It is initially based on previous studies of similar topics. The total number of cells is investigated through a grid independence study. When validating the model against computational data, a great coherence is present, which ensures realistic results when the model is used for optimisations later in the report.

Chapter 4

Design of PBCF

In the following chapter, the geometrical parameters defining the PBCF design will be elaborated. An introduction to the vital propeller and PBCF parameters will be stated together with a more detailed literature review, ultimately resulting in the base PBCF design used for the individual parameter optimisation procedure.

4.1 Definition of Propeller

The propeller/rudder system CAD-file provided by MAN Energy Solutions Frederikshavn can be seen in Figure 4.1. The propeller is a four-bladed Controllable Pitch Propeller (CPP) attached to a Ro-Ro ship. Though the propeller is a CPP it will be analysed as a Fixed Pitch Propeller (FPP), making the propeller unable to rotate during operation. This is obviously not practical, as the pitch of the propeller will, under certain operating conditions, be altered to yield a more efficient utilisation of the propeller rotation. CPPs are primarily implemented in ships that may require a rapid change in speed without compromising the electricity generated by the shaft rotation. The pitch of the propeller blades is thereby altered to either generate a change in forward or reverse motion without changing the rotational direction of the shaft.

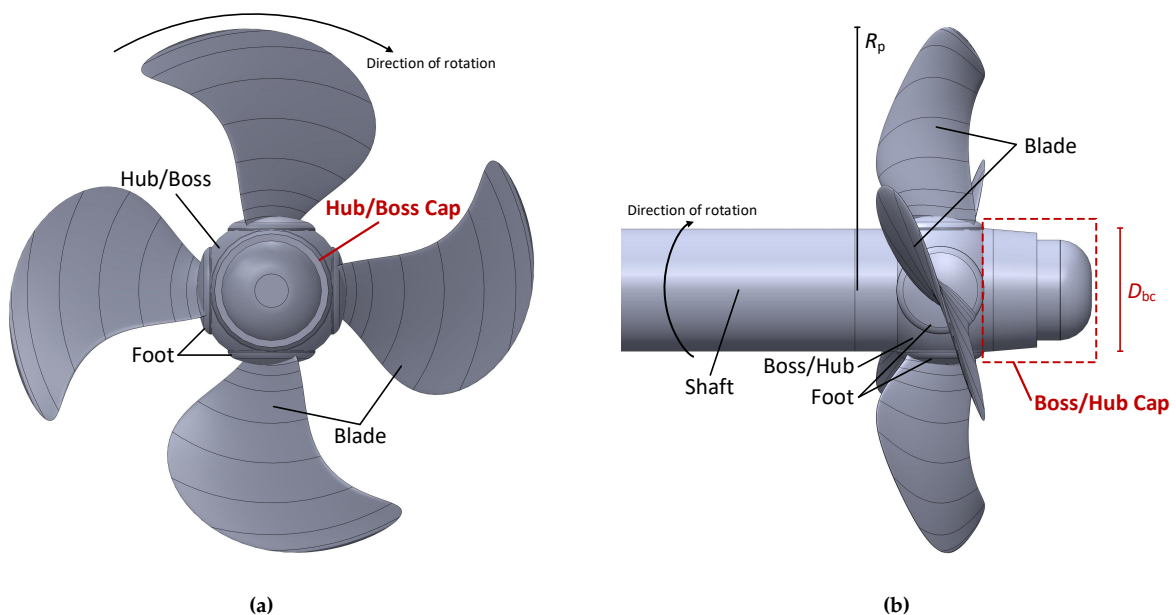


Figure 4.1: Illustration of the propeller, where (a) and (b) is a frontal and a side view, respectively. At (b) the boss/hub cap is clearly illustrated.

The propeller diameter is 4.8 m. but will be analysed at model-scale with a $D_p = 0.23 \text{ m}$, which will be used as a reference for the different measures of the PBCF geometrical parameters through this project. The root pitch angle of the propeller blade will likewise be used as a reference here with regards to the installation angle of the fins, which is explained in the following sections. The blade root profile is located at $r_{p,br}/R_p = 0.281$ and has a pitch of 5600.2 mm, stated in the propeller datasheet. The pitch can be converted into the blade root

pitch angle (ϵ) using its definition seen in Equation 4.1:

$$\tan(\epsilon) = \frac{P}{2\pi r_{p,br}} \longrightarrow \epsilon = \tan^{-1}\left(\frac{5600.2 \text{ mm}}{2\pi \cdot 674.4 \text{ mm}}\right) \approx \tan^{-1}(1.3216) \quad (4.1)$$

$$\longrightarrow \epsilon = 52.88671568^\circ \approx 52.89^\circ$$

where P is the pitch and $r_{p,br}$ is the blade root radius calculated knowing the radius ratio at the blade root, using Equation 4.2:

$$r_{p,br}/R_p = 0.281 \longrightarrow r_{p,br} = 0.281R_p = 674.4 \text{ mm} \quad (4.2)$$

The propeller model parameters utilised in this project are summarised in Table 4.1. The stated parameters in the table are visualised in the following figures through this chapter.

Table 4.1: Summary of the model propeller system's geometrical parameters utilised through this project.

Description	Symbol	Value
Model Scaling Factor	-	21.23894
Propeller diameter	D_p	226 mm
Blade root pitch angle	ϵ	52.89°
Boss cap base diameter	D_{bc}	53.02 mm
Boss cap length	l_{bc}	46.74 mm
Boss ratio	D_{bc}/D_p	≈ 0.235
Blade root radius	$r_{p,br}$	$\approx 31.75 \text{ mm}$
Blade root ratio	$r_{p,br}/R_p$	0.281

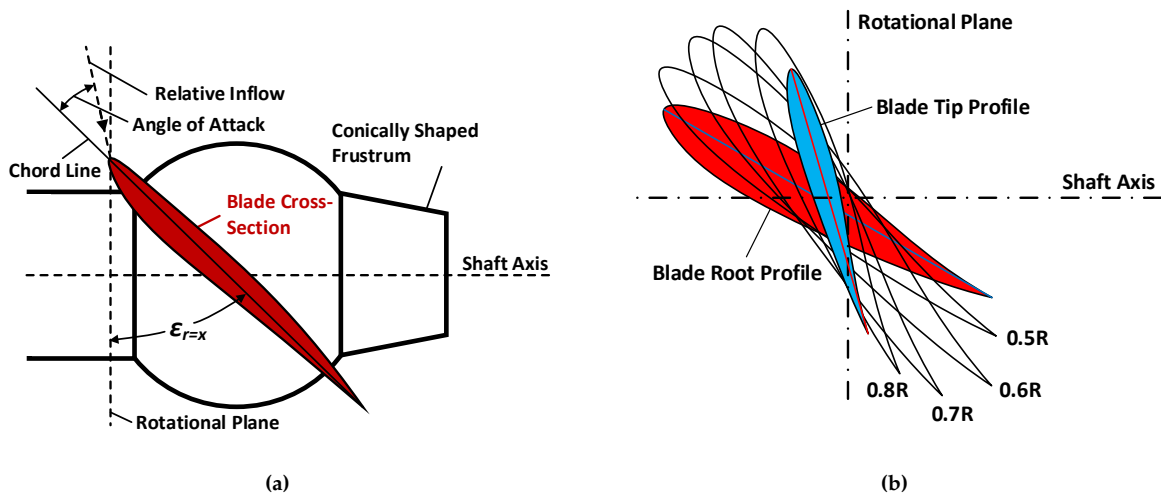


Figure 4.2: Definition of the blade pitch angle, where (a) illustrates a given blade cross-section and (b) illustrates varying pitch angles throughout the blade's radial span.

The propeller of a ship is a highly complex geometry to describe, which in modern times requires numerous parameters to fully comprehend the complete assembly, shown in Figure 4.1. Skew, rake, changing airfoil sections, and pitching at different radii are just some of the various parameters encountered when analysing a data sheet for a given modern-day ship

propeller. The approach of designing a PBCF, through this project, requires two of the propeller parameters, as stated above: the propeller blade pitch angle and the propeller diameter. The blade pitch angle is illustrated in Figure 4.2a for a given blade cross-section and is defined as the angle between the rotational plane and the profile chord. Here $\epsilon_{r=x}$ represents the propeller blade's pitch angle at a certain radius. A variable pitch can be seen in Figure 4.2b, where each profile cross-section through the blade's radial span (at a given interval) have different pitches. This is implemented to obtain the highest achievable propeller efficiency possible to ensure an economically and efficient operation. Due to the varying pitch throughout the blade, the manufacturers typically use the nominal pitch at $r/R_p = 0.7$ as the representing pitch value.

4.2 Geometrical Parameters of PBCF

Various geometrical parameters define the design of the PBCF. Through this section, the different parameters investigated in this project are elaborated, and a thorough literature study with particular attention to the analyses and results obtained by various researchers will be conducted. The different optimised measures from each study will be presented, which will form a starting point for the chosen geometrical parameters later applied in the PBCF base design.

4.2.1 Hub/Boss Cap Geometry

Firstly, the geometry of the boss cap is considered. The boss cap is directly bolted to the shaft/hub with bolts extending from the 'bolt notch', seen in Figure 4.3b, into the shaft/hub. The diameter of the hub end base and the boss cap base is typically made equal, making the two parts' transition as hydrodynamically smooth as possible.

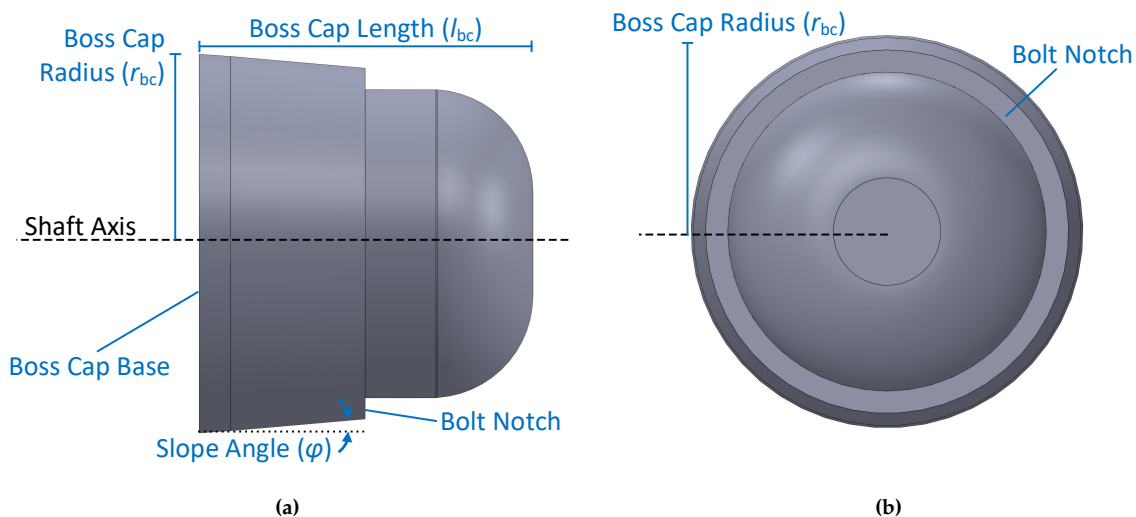


Figure 4.3: *a*) side view and *b*) downstream view of the boss cap.

The most investigated parameter regarding the boss cap is the slope angle (ϕ). The slope angle dictates whether the boss cap is diverging or converging, implying either a negative or positive slope angle, respectively. It is measured as shown in Figure 4.3a and the converging, straight, and divergent boss caps are shown in Figure 4.4.

In a study by Abar et al. [2018] the researchers investigate the effect of varying the slope

angle between $\pm 15^\circ$ in steps of 5° . In all cases where PBCF was installed on a diverging boss cap, they discovered that the efficiency decreased considerably. The decreasing trend for the diverging boss cap was found to be completely opposite for the converging. All converging boss caps with implemented PBCF were found to have an increasing effect on efficiency. A comparable conclusion was made by Katayama et al. [2015], who likewise found the efficiency to increase when installing PBCF on a converging boss cap. In a study by Lim et al. [2014] regarding the divergent boss cap, the authors discuss that the hub vortex downstream of the boss cap was increased by implementing PBCF on a diverging boss cap, which resulted in a decreasing tendency on efficiency. In the papers mentioned above, the researchers design the boss caps as a conically shaped frustum, with a constant slope angle for $\phi \neq 0$, as visualised in Figure 4.4. Notice that for the converging boss cap in Figure 4.4a all researchers have rounded the edge at the boss cap end base, thereby not keeping a constant slope angle throughout the entire extent of the boss cap.

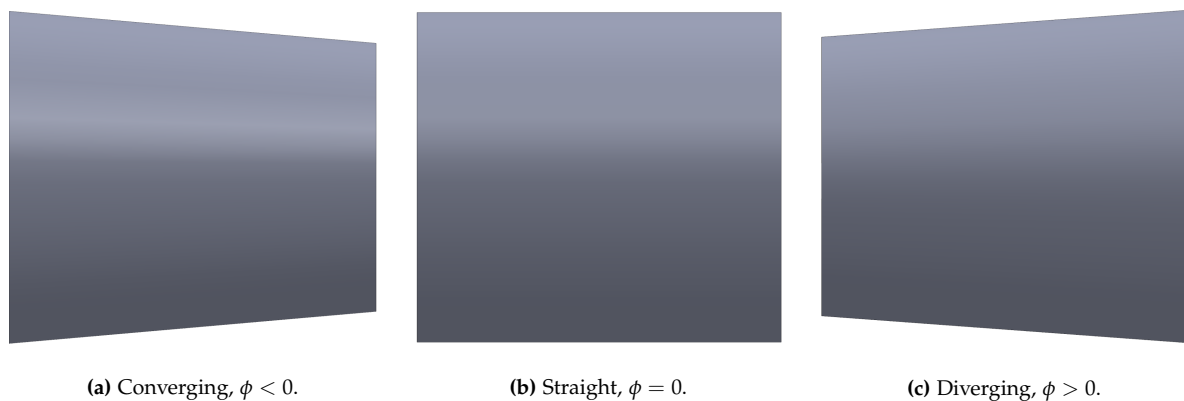


Figure 4.4

Another approach for designing the hub cap is presented by Druckenbrod et al. [2012], who divided the boss cap into a two-piece geometry defined by two independent functions. The two functions were allowed to be up to a third-order polynomial. Their first derivatives determined the transition between the functions, thereby the geometry of the boss cap at their intersections. The numerical modelling and simulation were done without PBCF but instead took the rudder and costa-bulb into account. They discuss that taking the rudder into account highly affects the boss cap performance, as the interactions between the rudder and boss cap would induce a pressure build-up around the boss cap. In the paper by Sun et al. [2016] the authors likewise investigate a propeller-rudder system, however, they install PBCF on a one-piece geometry, where the boss cap have a constant slope angle throughout its axial length. Similarly to the former study, the authors discuss the importance of likewise consider the rudder when implementing PBCF. Through empirical data, they discover a significant declining tendency in efficiency when the rudder is considered. Analysing the performance of the PBCF without and with a rudder attached yielded a decrease in efficiency from 1.47 % to 1.08 %. Furthermore, the authors then replace the rudder with a twisted rudder, which increased the efficiency from 1.08 % to 1.16 %. They thereby conclude that implementing a twisted rudder could yield a smaller decrease in efficiency compared with an ordinary rudder.

The literature evidently states that implementing PBCF on a diverging boss cap contributes

to increased torque upon the shaft, resulting in reduced efficiency. The boss cap must have a converging geometry to yield an increase in efficiency, either defined by a constant slope angle or multiple functions. In the majority of the literature, the researchers tend to neglect the hydrodynamic interaction between the boss cap and rudder. The various studies are typically more engrossed in designing, optimising, and conducting parametric studies regarding the PBCF, without an implemented rudder, than analysing the propulsion system to a full extent.

Through this project, the propulsion system will be investigated as a whole since the final PBCF design is conducted based on an already operating vessel. Neglecting the rudder would undoubtedly give rise to incomparable efficiency results.

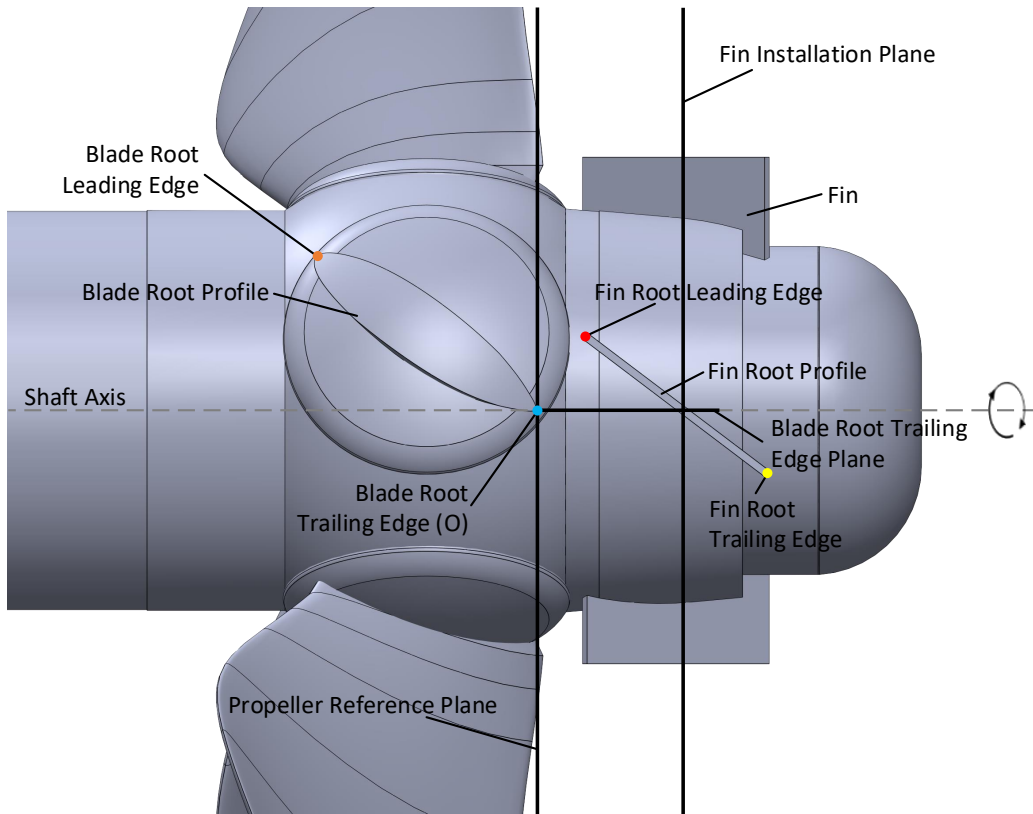
4.2.2 Fin Geometry and Definition

The design and installation process of the PBCF can be conducted through numerous parameters, which determines the shape of the fins, measurements, and position on the boss cap. The original developers, Ouchi et al. [1988], assessed the problem through a reasonably straightforward approach, especially compared with the more modern research. Since the invention of PBCF in 1987, various authors have investigated the parameters, profiles, number of fins, and shapes of the PBCF, both through numerical modelling and empirical assessment. In addition to the explanation and definition of each geometrical parameter, the research conducted regarding each parameter will be discussed in the following sections, as well.

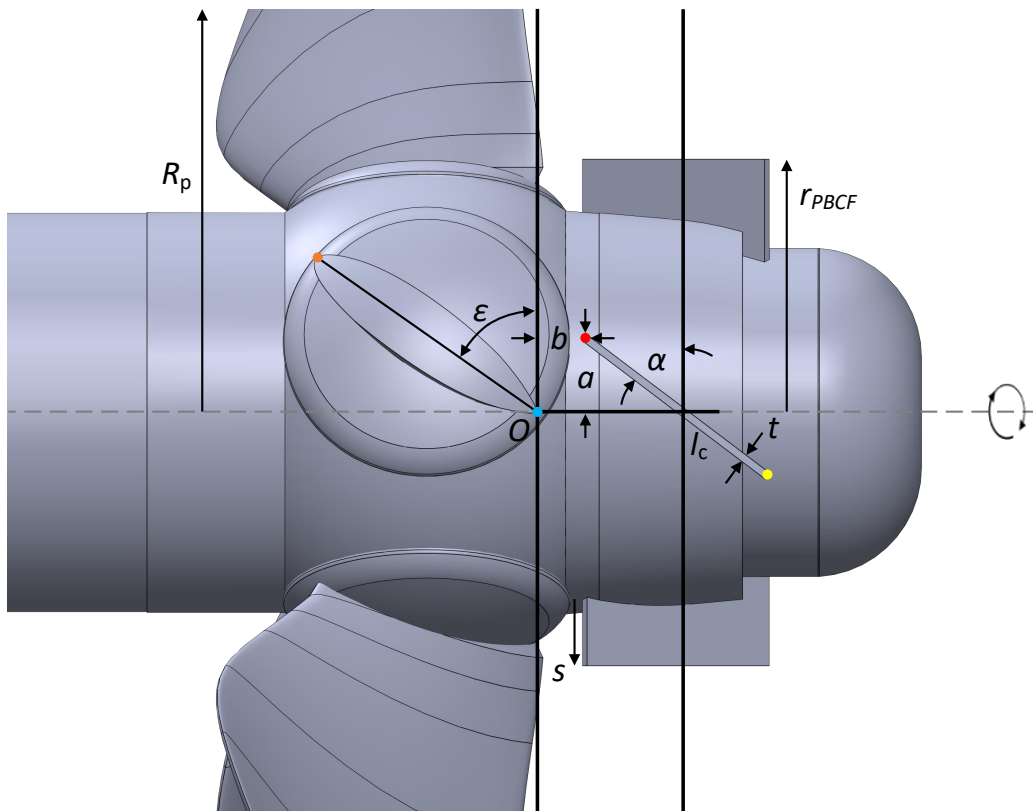
In the patent of the PBCF, Ogura et al. [1987], the developers discuss that the number of propeller blades should equal the number of fins to maximise their increasing effect on the efficiency. In the study by Katayama et al. [2015] the researchers investigate the implementation of PBCF with more fins than propeller blades. Here the implementation of PBCF are conducted upon a five- and six-bladed propeller, where seven fins are attached upon the converging boss cap of each propeller. The authors concluded an increase of 1.28 % and 0.69 % for the six-bladed and five-bladed propeller, respectively. When investigating the different literature, the vast majority obey the designing guidelines of an equal number of fins and blades, as presented by Ogura et al. [1987]. The results obtained by the former paper could indicate that a larger difference between the number of fins and blades would yield a smaller increase in efficiency and may likewise indicate that keeping them equal is most optimal. A difference between the number of fins and blades will similarly struggle to direct each slipstream from each blade, possibly still inducing the hub vorticity downstream. The symmetry of equalising the fin and blade number will therefore yield the ability to diminish the forming hub vortex, increasing the efficiency by lowering the boss cap drag induced by the low-pressure zone directly downstream of the the boss cap.

The definition of each applied geometrical parameters through this project are visualised in Figure 4.5. The following bullet list has been added to yield a more thorough understanding of each parameter:

- **Radius (R_p) and (r_{PBCF})** - radius of both the propeller and PBCF, respectively, defined as the distance from the shaft axis to the tip of either.
- **Chord (l_c)** - for a given profile, defined as the distance from the leading to the trailing edge.



(a) Definition of noteworthy profiles, axes, planes, and points.



(b) The applied geometrical parameters shown for a rectangular profile.

Figure 4.5

- **Fin span (s)** - span of the fin from the boss cap surface to the fin tip.
- **Leading/Trailing edge** - the front and back end intersection point for a given profile, respectively.
- **Installation position:**
 - **Circumferential distance (a)** - defined as the arc length from the plane perpendicular to the shaft axis and coinciding the trailing edge of the blade to the fin leading edge.
 - **Axial Distance (b)** - distance between the propeller reference plane to the leading edge of the fin.
- **Installation angle (α)** - the angle between the fin installation plane and the fin chord. Note that the installation angle is also referred to as the fin root pitch angle through some literature.
- **Max thickness (t_{\max})** - measure of the maximum thickness for a given profile. If the thickness throughout a profile is constant, this parameter will solely be referred to as thickness (t).
- **Camber (c)** - measure of the maximum camber of a given profile. Maximum distance from the chord to the camber mean-line (centre-line at all centre-points). For rectangular profiles or symmetric foils, no camber is present. The parameter is visualised in Figure 4.6.
- **Rake angle (θ)** - fins installed perpendicular to the boss cap surface curvature has a rake angle equal to zero. If the rake (inclination) angle is slightly changed, the fin will not be perpendicular to the surface curvature and thereby obtain a rake angle to some extent. The parameter is positive in the direction of rotation and is visualised in Figure 4.7.

4.2.3 Fin Profile

In over a century, airfoils have been integrated into numerous applications and are widely implemented within the maritime industry. The cross-sections of modern-day rudders, propellers, costa bulbs etc., are all constructed from the basis of airfoils, which will be referred to as hydrofoils, as they are utilised in water. The research and documentation of the countless hydrofoils are extensive and is therefore still highly applicable in recent maritime developments and constructions.

Regarding designing PBCF, the different studies have by default applied the rectangular profile, which the original developers proposed in their patent Ogura et al. [1987]. A cross-sectional view of the rectangular profile and NACA 4412 hydrofoil are visualised in Figure 4.6. Designing the fins as streamlined as possible is of great interest due to their enhanced hydrodynamic performance by decreasing resistance and drag, which can be assisted by utilising hydrofoils. Since the first series' development in the late 1920s, numerous NACA profiles have emerged. Each series of NACA hydrofoils has been designated by a digit system, describing the key parameters for each generation and each profile. The first series of NACA foils were designated by a four-digit system describing the maximum camber, camber placement, and

maximum thickness. For the NACA 4412 (seen in Figure 4.6b) the first digit describes a maximum camber as 4 % of the chord. The second digit defines the length of the maximum camber from the leading edge in tenths of the chord, here 40 %. The last two digits describe the maximum thickness as 12 % of the chord. [Jacobs et al., 1933]

As mentioned, the vast majority of the literature designs the PBCF based on the rectangular profile. In the original developers patent, Ogura et al. [1987], the authors investigate the fin shape's effect on the propeller efficiency. Their conception of the fin shape was only in regards to the fin aspect-ratio (chord-to-span ratio), where the profile chord is altered throughout the span of the fin. They implemented a rectangular rounded-edge profile (see Figure 4.6a) and investigated different aspect-ratios subsequently. In the study by Majumber and Maity [2020] the authors design the PBCF on a NACA hydrofoil basis. Of the four cambers tested, they concluded that the NACA 4412 hydrofoil had the greatest effect on efficiency, yielding a maximum of 3.52 % increase. Note that the authors have optimised all other geometrical parameters prior to the hydrofoil implementation and that the hydrofoils were not compared with the traditional rectangular design. The large efficiency increase due to the hydrofoil implementation indicates that the rectangular design is obsolete and that hydrofoils may have the capabilities to enhance the hydrodynamic performance of the PBCF even further. As stated in Section 1.1, the study by Ouchi et al. [1988] obtained an increase of up to 7 % when implementing PBCF, though the authors fail to state the production year of the CP26 propeller model. In the former study, the researchers investigate a VP1304 propeller from 1998, which is of newer date than the former, based on the publication year of each study. The CP26 propeller might be older than the publication date of their paper, indicating that it may not be as hydrodynamically optimised as the latter. In the paper by Gaggero [2018] the author investigates two different propellers; a five-bladed KP505 propeller designed by [Kim et al., 2001] and a four-bladed E779A propeller from 1959. By implementing hydrofoils as PBCF, the researcher increases open water efficiency of 0.9 % and 4 % from CFD analysis regarding the KP505 and E779A propellers, respectively. The authors discuss that the older E779A propeller is not as hydrodynamically optimised in mitigating the induced hub vortex as the newer KP505 propeller. He likewise states that implementing the PBCF on an obsolete propeller would yield an increase in efficiency regardless of geometrical parameter variation due to the unrefined hydrodynamic design and performance.

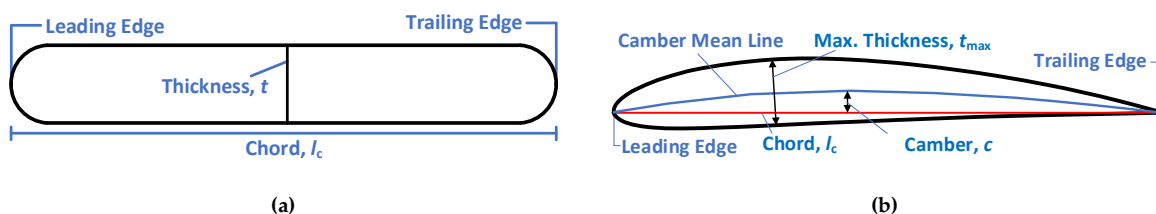


Figure 4.6: Common types of fin profiles: (a) the rectangular profile with rounded-edges and (b) the NACA four-digit hydrofoil's geometrical definition.

The thickness of the chosen profile is likewise vital, regardless of being a rectangular profile or hydrofoil. Extending the thickness of a given profile will yield more surface area added for each fin resulting in increased resistance and contributing to a rise in investment costs due to added production material. The inventors designed the PBCF with a thickness of

$t/R_p \approx 0.01$, constant due to the rectangular profile Ogura et al. [1987]. The authors likewise kept a constant root profile chord length of $l_c/D_p \approx 0.12$. In the study by Gaggero [2018] the researcher analyse the effect of thickness on efficiency but neglects to inform the reader about the actual value. He instead utilises a thickness scaling factor and examines the parameter's impact when using hydrofoils in the PBCF design. The author discusses that the thickness affects efficiency but lacks the same significance as the camber in comparison. Based on an optimisation algorithm, he optimises the chord length for the hydrofoil to be $l_c/D_p = 0.12$, similar to the former authors. Mizzi et al. [2017] likewise investigated the thickness and fin length of a rectangular fin based on an optimisation algorithm and found an optimum value for each of $t/R_p \approx 0.003$ and $l_c/D_p \approx 0.06$.

4.2.4 Fin Installation Position

The installation position consist of two parameters: the axial position b and the circumferential position a , which are shown in Figure 4.5. These two parameters were proposed by the inventors in their patent Ogura et al. [1987], and will be applied through this project. The two parameters determine the position of the leading edge of the fin and thereby the starting point for the fin's position on the boss cap. The axial and circumferential positions are defined by the propeller blade root's trailing edge (point O in Figure 4.5) and the propeller reference plane. From an extensive empirically obtained data set, the inventors discovered that $a < 0.14R_p$ and $b < 0.15R_p$ yields a considerable increase in efficiency. They likewise discuss that the best result is obtained by installing the fin's leading edge in-between two blade's circumferential position. Some authors utilise another approach to define the fin's position, see e.g. Druckenbrod et al. [2015] and Seo et al. [2016].

In the study by Ghassemi et al. [2012] the authors likewise investigate the installation position of the fins but instead utilises the phase angle to describe the circumferential position instead. The phase angle and circumferential distance are dependent on each other, as the phase angle describes the arc distance from the blade root trailing edge reference plane (perpendicular to the shaft axis) to the leading edge of the fin as an angle, instead of an arc distance. The authors still utilise the same definition of the axial distance and observe that by implementing PBCF, a more uniform flow downstream and a mitigated hub vortex is achieved. They conclude that the phase angle is a crucial parameter to determine, and if chosen unsuitable, a notable degradation in performance could be observed.

Hsin et al. [2008] He likewise investigated the installation position by utilising the circumferential arc distance instead of the phase angle. They discover through a parametric study, using the potential flow boundary element method, that the circumferential distance had little effect on the efficiency, in disagreement with the former paper, and fails to state their chosen value. They discover that the axial distance should be as close to the propeller blade root's trailing edge as possible and applied $b = 0.10R_p$.

4.2.5 Fin Installation Angle

As stated in the patent by Ogura et al. [1987], the authors describe the installation angle as one of the most critical parameters in the PBCF design. The inventors present that the difference between the installation angle (α) and the propeller blade root pitch angle (ϵ), should be kept between $-20^\circ \leq \alpha - \epsilon \leq 30^\circ$. The authors found that the highest gain in efficiency was achieved with a relatively small difference between the angles obtained at $\alpha - \epsilon = -1.4^\circ$. Note that

the inventors refer to the installation angle as the inclination angle, as various other authors have done since, which will not be utilised through this project. Generally, the terminology regarding the geometrical parameters through the literature is, to a great extent, challenging to decode, as various authors tend to invent new terms or mix the terminology from different authors.

In the study by Hsin et al. [2008] the researchers likewise investigate the installation angle and verifies the critical role of this parameter when designing the PBCF. They state that the installation angle should be chosen with careful consideration, but the authors neglect to mention their final measure of the parameter.

In the paper by Lim et al. [2014] the authors conduct a sensitivity analysis and analysis of variance, based upon the three critical parameters reported by [Ouchi et al., 1988]: diameter of the PBCF, rake angle, and installation angle. The installation angle was investigated within a range close to the propeller blade root pitch angle, $\alpha - \epsilon \approx \pm 5^\circ$. Their study clearly discarded the rake angle as a critical parameter, as the influence on efficiency from the installation angle and PBCF diameter were considered superior. Additionally, they conclude that the correlation between the different parameters is insignificant.

When the fin has been installed and welded in place, the installation angle is permanent. Designing PBCF for the boss cap of an FPP is relatively straightforward, as the blade root pitch angle cannot be altered under operation. The blade root pitch angle highly influences the installation angle (due to the blades' slipstreams and therefore the relative inflow angle to the fins), the optimum achieved PBCF design does not need to be varied as ϵ is constant. For a CPP, the design phase of PBCF needs to take the changing blade root pitch angle into account when the blades' pitch angle is altered. An approach is to analyse the operation time at each pitch setting so that the PBCF can be designed for the pitch setting that undergoes the highest operation time (design point operation). This implies that when the PBCF is welded onto the boss cap, the fins' geometrical parameters are fixed and could negatively affect the efficiency when the propeller pitch settings are altered. Therefore, it could be of great interest to examine this observed phenomenon, as it influences operation costs due to fuel consumption.

4.2.6 Fin Span

As stated by the inventors in their patent, Ogura et al. [1987], to obtain a considerable gain in efficiency by implementing PBCF, the diameter of the PBCF should not exceed $0.33D_p$. The radius of the PBCF is proportional to the fin span, as increasing the span will increase the r_{PBCF} by the same amount. Being one of the most influential parameters, various authors have investigated the fin span/diameter, which is stated in Table 1.2 on page 7 as well. Increasing the fin span yields a larger surface area, magnifying the torque upon the shaft, implying a decrease in efficiency. Similarly, an increased span height will enhance the fins hydrodynamic capabilities of redirecting the slipstreams from the blades to weaken the hub vortex induced downstream, yielding an increased efficiency. This phenomenon holds to a certain degree, where the span will become too large, and the increase in torque will be more significant than the redirecting abilities of the fins, resulting in a decrease in efficiency.

Gaggero [2018] analysed the different critical parameters in the PBCF design by utilising optimisation algorithms and carrying out CFD analyses. As mentioned in Section 4.2.3 on page 38 the author examines two propellers: a newer and an older and more unrefined (the KP505 and E779A). The author confirms the key role of the fin span for both propellers but

state that it has the greatest influence on the newer propeller. The researchers find that the optimum diameter ratio for the newer and older propeller are $D_{\text{PBCF}}/D_p = 0.39$ and $D_{\text{PBCF}}/D_p = 0.25$, respectively.

In the study by Seo et al. [2016] the authors focus on the hub vortex dynamics of the same propeller as Gaggero [2018], and the implementation of PBCF. The authors utilised a propeller open test (POT) setup to examine the various design parameters of the PBCF. The authors discuss that the most significant change in efficiency came from a variation of the fin span. They concluded that implementing PBCF indeed decreased the low-pressure zone generated behind the boss cap, contributing to a positive gain in efficiency. In accordance with Gaggero [2018] the authors optimised the diameter ratio and found $D_{\text{PBCF}}/D_p \approx 0.25$ yielded the most significant increase in efficiency. This value corresponds well with the condition set by the inventors, which was 33 % of the propeller diameter. Note that the presented condition by Ogura et al. [1987] of 33 % is merely a guideline to obtain a considerable gain in efficiency. The inventors found that the most significant efficiency increase was obtained at $D_{\text{PBCF}}/D_p \approx 0.23$.

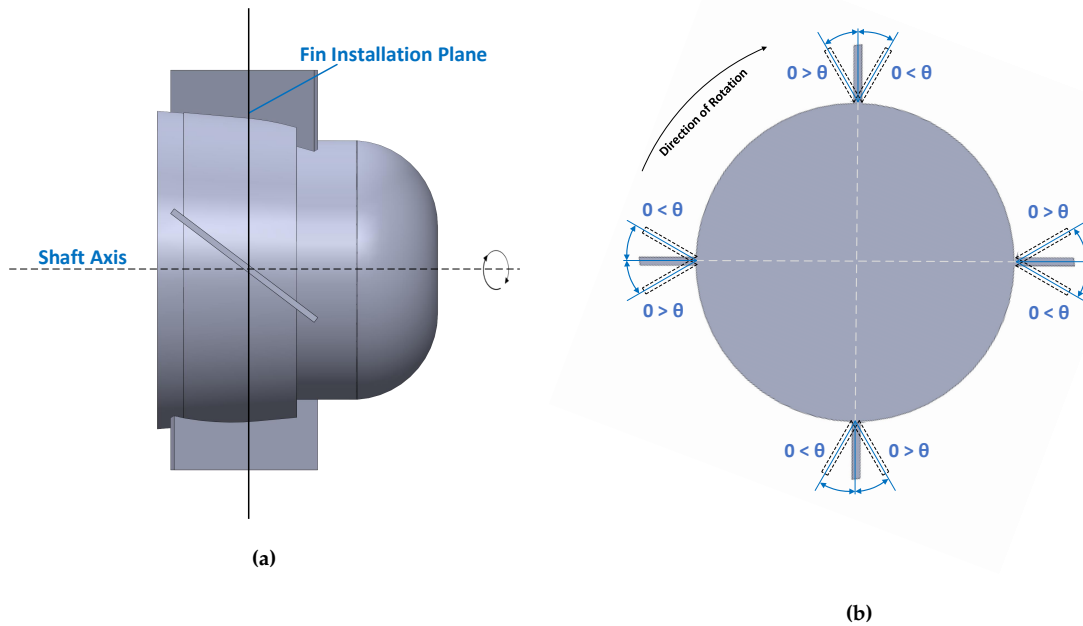


Figure 4.7: Rake angle definition, here (a) side view of the installed fin ($\theta = 0$), and (b) a cross-sectional cutout in the installation plane, with a changing rake angle visualised.

4.2.7 Rake Angle

Studies have been conducted regarding the rake angle (see Figure 4.7), but the authors tend to neglect to mention the optimised measure of the value. The inventors examined the rake angle in three tests in their patent, Ogura et al. [1987], with rake angles of 30° , 0° , and -30° . They obtain the highest efficiency gain at -30° when the fins are inclined towards the opposite direction of rotation. The improvement is though minimal, compared to the perpendicular installation of $\theta = 0^\circ$. In the paper by Lim et al. [2014] the authors similarly examines the effect of the rake angle, here from -10° to 10° in steps of 10° , which they refer to as the inclination

angle. They discuss that the rake angle is insignificant compared to the installation angle and diameter ratio, which nearly does not affect the result of the sensitivity analysis conducted. From their results, it can be analysed that changing the rake angle had little effect, and the results were more or less inconclusive. Contrary to the former two studies, in the paper by Hsin et al. [2008] the authors found that the two most critical parameters to consider are the installation and rake angles. The authors fail to state the final value of all the investigated parameters, likewise yielding inconclusive results.

4.2.8 Summary of Geometrical Parameters

Based on the literature study done above, a preferable range/type has been chosen to implement for each parameter, which is stated in Table 4.2. The table will be used as a guideline when further individual optimisation of each parameter is conducted. In the literature study above, the maximum preferable value for the diameter ratio was found to be ≈ 0.25 . It was found that most of the studies regarding this parameter investigate a smaller boss cap than the one utilised through this project. For instance, in the paper by Gaggero [2018] the author's boss ratio was found to be $D_{bc}/D_p = 0.18$, where the boss ratio through this project is $D_{bc}/D_p = 0.235$. Therefore, a larger diameter ratio has been chosen since a smaller ratio would yield a deficient fin span, not resulting in a functional PBCF design. This indicates that a more appropriate way is to state the boss ratio and span height together to indicate the parameters' measures clearly.

Table 4.2: Preferable measures/types of parameters regarding PBCF design, based on the literature study.

Parameter	Hub Cap	Number of Fins	Fin Profile	Installation Position	Installation Angle	Diameter Ratio	Chord Ratio	Thickness	Rake Angle
Preferable Range/Type	Converging	Same as number of blades	Rectangular or Airfoil	$a \leq 0.14R_p$ $b \leq 0.15R_p$	$-5^\circ \leq \alpha - \epsilon \leq 5^\circ$	$D_{PBCF}/D_p \leq 0.30$	$l_c/D_p \leq 0.12$	$t \approx 0.01R_p$	$-30^\circ \leq \theta \leq 10^\circ$

4.3 Rectangular Base PBCF Design

In this section, the base PBCF design will be introduced based on the literature study conducted above. From Table 4.2 a guideline for choosing a viable base design is shown, which will act as the starting point for future parameter investigations.

Before the design of the actual PBCF can commence, the boss cap should first be considered/revisited as stated in the literature study in Section 4.2 on page 33. The original boss cap designed by MAN Energy Solutions Frederikshavn can be seen in Figure 4.3 on page 33, where the bolt notch is clearly indicated. This bolt notch is a practical implementation, which aids the bolting process of the boss cap. When implementing fins directly on the boss cap, they may overlap the bolt notch implying complications in the bolting of the boss cap. Likewise, a more streamlined design may achieve higher efficiency, as the bolt notch may assist in forming re-circulation zones in the near vicinity of the notch.

As mentioned, the bolt notch is necessary for bolting the boss cap, which restricts the re-designing possibilities of the boss cap. In Figure 4.3a the restrictions are especially limited by the part from the base to the bolt notch, which contains the axial assembly of the bolting of the boss cap, implying a minimum change can occur for the slope angle.

A solution is to retain the original boss cap and then construct the PBCF upon a "cape" that can be assembled or pulled over the original boss cap, using the same bolts. The

cape can be designed much more streamlined, yielding better hydrodynamic performance than its predecessor. The practical manufacturing issues of producing the cape needs to be taken into account, and the slope angle for the cape can maximum be 1.4° (stated by MAN Energy Solutions Frederikshavn) to ensure a sturdy design of the cape. This ensures that the cape is durable enough to attain the required performance without becoming too thin in this particular section. Therefore, the maximum allowed limit of the slope angle is selected, as the literature study showed that a larger slope angle yielded higher efficiency of the configuration. The original boss cap with the cape seen in a cross-sectional view behind, and the new configuration can be seen in Figure 4.8 on page 43.

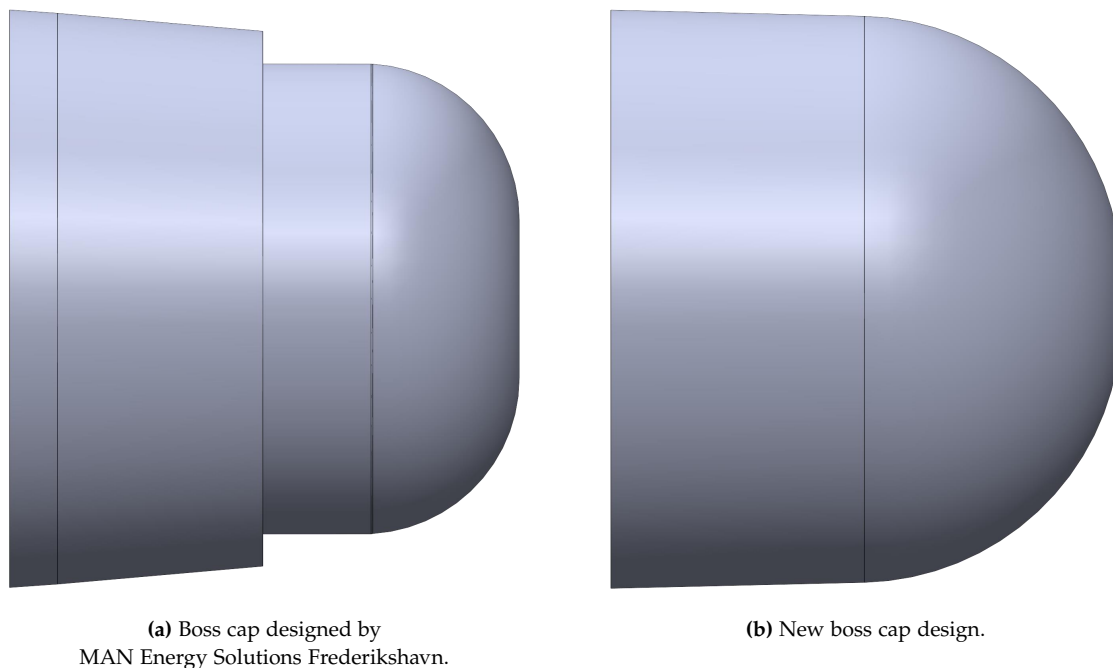


Figure 4.8

The original boss cap and the new cape design have an equal length, determined by the distance from the hub end base and the rudder placement. To accommodate the equal lengths without intersecting with the rudder requires the part of the boss cap from the bolt notch to the end to be removed. Likewise, can the MRF domain not be extended. As seen in Figure 3.2b on page 14 the MRF domain and the top part of the rudder nearly overlap, which limits the extension of the MRF. Without an extension, a part of a larger boss cap would not be included in the rotation scheme in the simulation, yielding incorrect results. A more extended boss cap would still be of great interest, as a more conically shaped boss cap have great potential of improving efficiency even further.

The original boss cap and the new have been tested through the numerical model presented in Chapter 3 starting from page 9. As expected, the cape design gave the most significant increase in efficiency and will therefore be utilised in the base designing of the PBCF. From the numerical model, comparing the original boss cap and the new design resulted in an efficiency increase of 0.17 %.

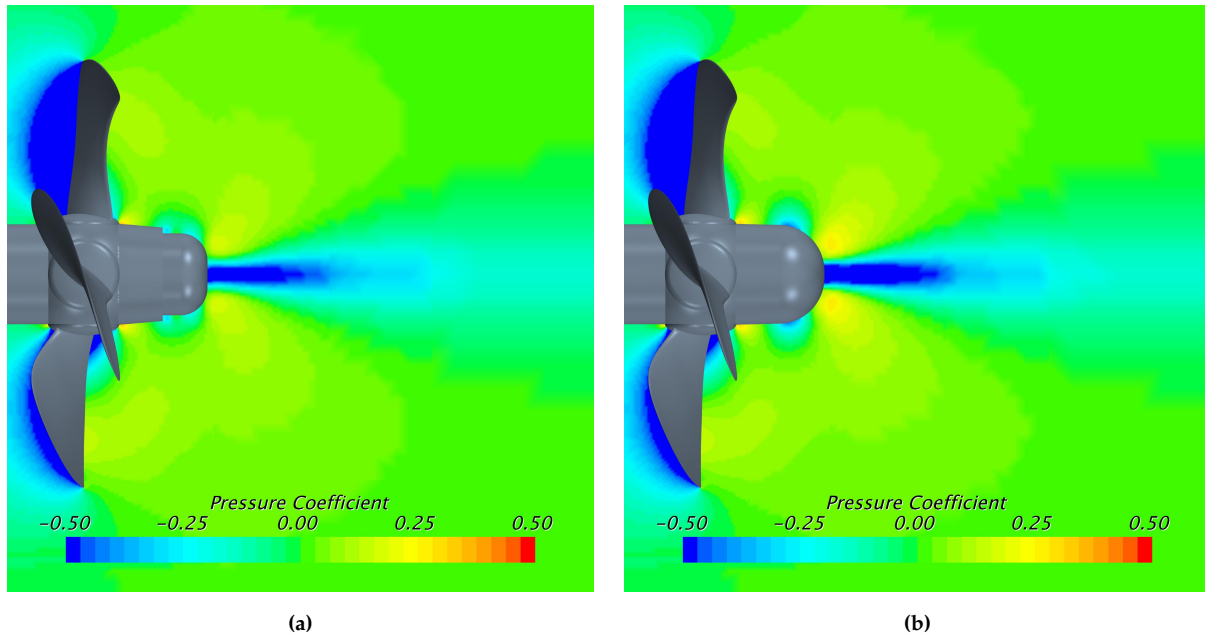


Figure 4.9: C_p contours comparison between the original and the new boss cap, without the rudder attached.

In Figure 4.9 a C_p contour plot comparison of the original and new boss cap can be seen. As expected, the new boss cap design has a negligible impact upon the low-pressure zone directly downstream of the end of the boss cap. This indicates that the efficiency increase gained by implementing the new boss cap does not originate from mitigating the hub vortex, which results from the low-pressure zone. The hub vortex has seemingly increased in strength for the new design, and it is therefore believed that the efficiency increase is implied by the more streamlined boss cap design. From Figure 4.9b it can be seen that a low-pressure zone around the beginning of the hemisphere at the end of the boss cap occurs. This indicates that a more streamlined and efficient boss cap design may be constructed, but due to the slope angle and the internal bolting limitation in the first part of the boss cap, this has not been evaluated further.

The chosen measures of each parameters is stated in Table 4.3, based upon the range stated in Table 4.2. A base PBCF design can be made from these selected measures, which can be seen in Figure 4.10. As a starting point for further optimisation, the traditional rectangular profile has been chosen for implementation. This is both done based on the vast data hereof and the straightforward implementation process. From the literature, it was noted that when applying rectangular profiles to the boss cap, most literature utilises fillets at the leading and trailing edges, and likewise on the fins' top surface curvature, which will be done to make the design more comparable with the literature. The design will, through the following sections, be referred to as the "Rectangular Base Design".

Table 4.3: The implemented values for each geometrical parameter in the rectangular base design.

Parameter	Number of Fins	Fin Profile	Installation Position	Installation Angle	Diameter Ratio	Span	Chord Ratio	Thickness	Rake Angle
Base PBCF Design	$n = 4$	Rectangular	$a = 0.088R_p$, $b = 0.062R_p$ $= 10 \text{ mm}$, $= 7 \text{ mm}$	$\alpha - \epsilon = -1.4^\circ$	D_{PBCF}/D_p $= 0.296$	s $= 7.5 \text{ mm}$	$l_c/D_p \approx 0.12$ $= 27 \text{ mm}$	$t = 0.009R_p$ $= 1 \text{ mm}$	$\theta = 0^\circ$

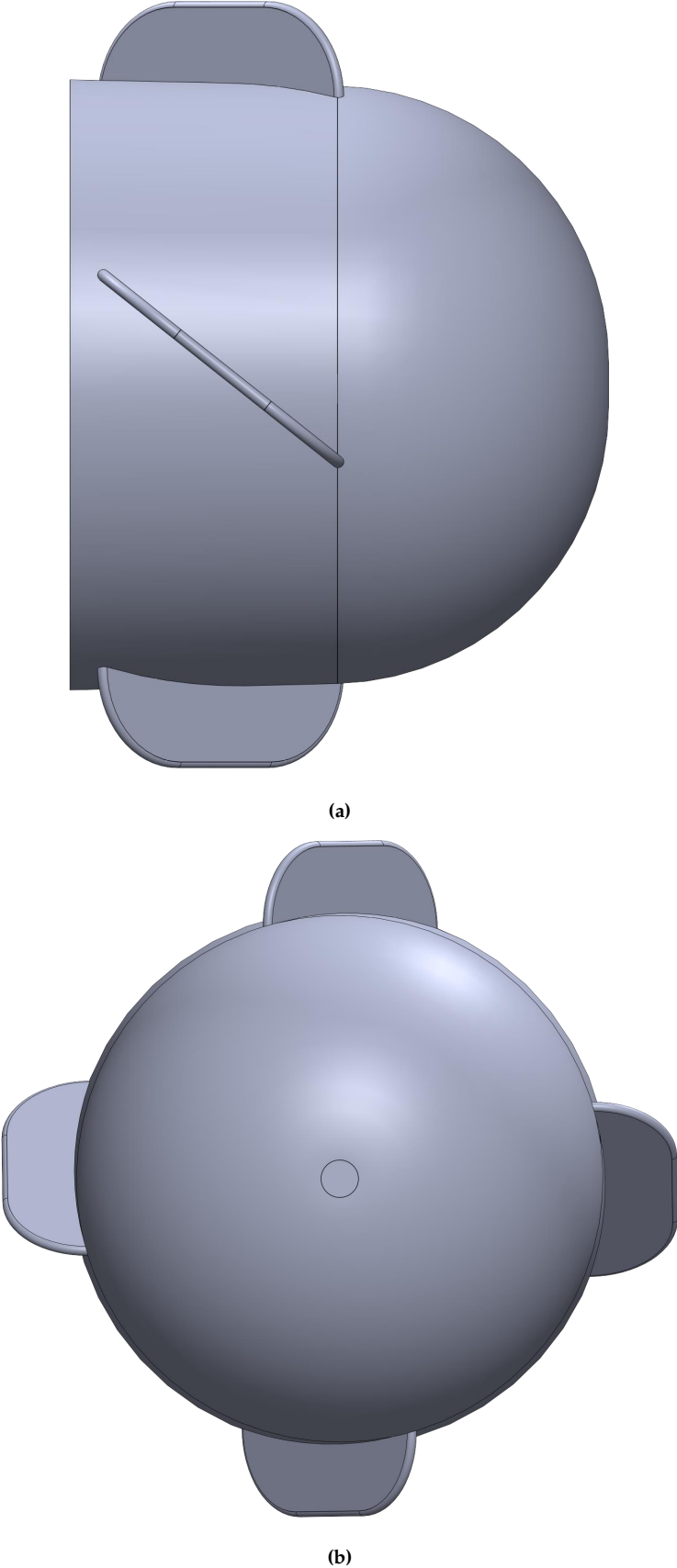


Figure 4.10: The rectangular base design, where (a) side view and (b) front view.

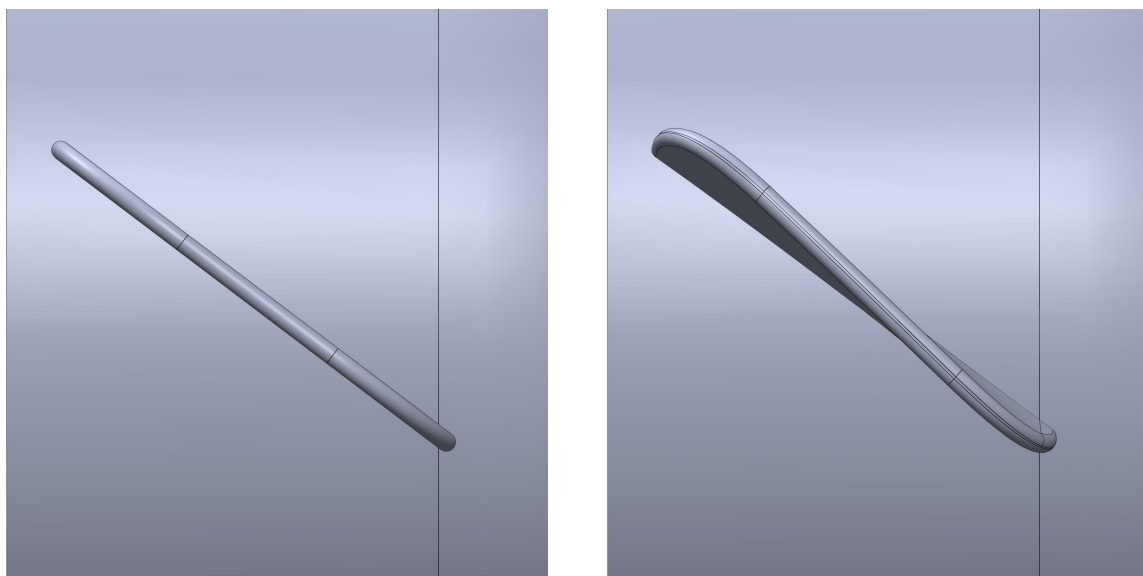
4.4 Analysing the Rectangular Base Design

This section will investigate different defining options of the rectangular base design to examine if a better base design alternative can be achieved before the individual optimisation of each parameter commences.

4.4.1 Fin Installation Arrangement

The literature attaches the fins in mainly two arrangements. The original approach by Ogura et al. [1987], is used to a great extent in the literature and installs the fins perpendicular at the intersection point on the boss cap surface curvature between the installation and the blade root trailing edge planes. Similarly, the installation angle and chord length are kept constant throughout the span of the fins, which would not be the case if a pitching fin were implemented. The other approach has likewise been given much attention in recent years and is, for example, applied by Hsin et al. [2008]. This particular arrangement is made by ensuring that throughout the fin's span, the fin is perpendicular to the boss cap surface curvature at all times. Applying this arrangement implies an unavoidable change to the chord, thickness, and installation angle, as these three parameters will change due to the arrangement. Making the fin perpendicular to the boss surface curvature implicitly creates a pitching fin, causing the pitch angle at different PBCF radii to change accordingly. The fin root at the second arrangement will still be designed based on the initial values for each parameter stated in Table 4.3.

Furthermore, can the pitch angle at different PBCF radii be a parameter to investigate, which for example, was done by Gaggero [2018]. This will not be investigated in this project, but the two installation arrangements will be analysed to see if a better base design can be obtained. The traditional design by Ogura et al. [1987] and the perpendicular to the boss cap surface curvature applied by Hsin et al. [2008] arrangements will be referred to as the traditional and perpendicular arrangement, respectively.



(a) Traditional arrangement by Ogura et al. [1987].

(b) Perpendicular arrangement applied by Hsin et al. [2008].

Figure 4.11

In Figure 4.11 the two different fin arrangements can be seen. In Figure 4.11a the fins are only perpendicular to the boss cap surface curvature in the intersection points, mentioned prior. In Figure 4.11b the fins are arranged perpendicular throughout its intersection with the boss cap, clearly imposing unavoidable pitching of the fins.

The two arrangements have been simulated, and the perpendicular arrangement showed the most promising results. The traditional and perpendicular arrangement yielded an efficiency improvement compared to the original boss cap of 0.62 % and 0.78 %, respectively. The increase in efficiency due to the perpendicular fin installation indicates that the pitching of fins should be considered. The perpendicular installation will be implemented into the design procedure.

4.4.2 Hydrofoil Investigation

As mentioned in Section 4.2.3 on page 37 replacing the traditional rectangular fin design with hydrofoils could produce some interesting results by redirecting the blades' slipstream and thereby weaken the induced hub vortex.

The selection of hydrofoils is immense, as numerous have been developed over the years. On the web page, Airfoil Tools [2021] 1,638 different airfoils can be found, where the vast majority have been tested through the software *XFOIL* developed by the Massachusetts Institute of Technology in the 1980s. The software is still widely used today, despite it being old-fashioned and has undergone multiple updates since its release.

As the web-page address indicates, the foils presented and investigated through the software *XFOIL* on the web page are tested in air. Though the lift and drag coefficient for a given airfoil can not be compared with those of a hydrofoil, due to change in viscosity, density, resistance, etc., the lift/drag ratio is assumed to be approximately the same. This permits that the lift and drag coefficient ratio (C_L/C_D) data for each airfoil on the web-page can be utilised for the investigation of replacing the rectangular profile with an airfoil/hydrofoil.

To determine the lift/drag ratio for each selected airfoil, the Reynolds number and Ncrit parameter must be specified. The Reynolds number is dependent on the chord length and is calculated as stated in Equation 4.3:

$$\text{Re}_{l_c} = \frac{V_S l_c}{\nu_\infty} = \frac{2.08 \text{ m/s} \cdot 0.027 \text{ m}}{1.191 \cdot 10^{-6} \text{ m}^2/\text{s}} = 47,153 \approx 50,000 \quad (4.3)$$

where ν_∞ is the kinematic viscosity, obtained from the propeller datasheet.

The Ncrit parameter is a way of predicting the transition of incompressible flow boundary layers and is highly influenced by the free stream turbulence (see Ingen [2008]). On the website, the parameter ranges from 1 to 14, where a small and large Ncrit implies a high and low turbulent flow, respectively. Ncrit = 5 has been chosen, as the flow indeed is turbulent after the propeller.

Nine hydrofoils have been chosen to be investigated and compared with the rectangular profile to see if a better base design can be achieved. These hydrofoils have been chosen mainly based on their respective lift/drag ratio, where a higher ratio yields the highest lift and efficiency. The chosen hydrofoils for investigation can be seen in Table 4.4, together with their respective profile number, maximum lift/drag ratio, and the Angle of Attack (AoA) at which the maximum lift/drag ratio occurs. The profile "*CH10*" seen in the table has been chosen due to its high lift at low Reynolds numbers. The profile likewise has a high drag, as seen for its lift/drag ratio, and have been investigated to examine if this could yield a better result

than just analysing the profiles with the highest lift/drag ratio. The profile NACA 4412 has been widely used in fluid dynamics for nearly a century and keeps being mentioned through various literature. Likewise, was this profile investigated by Majumber and Maity [2020], as mentioned in Section 4.2.3 on page 37, and yielded the highest result in their research when implementing hydrofoils as fins for the implementation of PBCF.

Each of the profiles stated in Table 4.4 are visualised in Appendix B on page 85.

Table 4.4: Profile performance information from Airfoil Tools [2021].

Profile Name	Rectan- gular	AH-6-40-7	Bergey BW-3	CH10	E63	GOE 79	NACA 4412	cp-100-050-gn	20-32C	S1223
Profile Sim. Number [-]	0	1	2	3	4	5	6	7	8	9
Max C_L/C_D (at $Re \approx 5 \times 10^4$, $N_{crit} = 5$) [-]	-	46.9	46	12.4	51.1	42.7	36.1	23.9	40.8	42.3
AoA for Max C_L/C_D [°]	-	4.8	5.0	3.5	5.3	5.5	8.5	11.0	3.8	3.3

Optimum Installation Angle Estimation

As seen in Table 4.4 the different profiles yields their individual maximum lift/drag ratio at different AoA. To make comparable results, an estimate of the actual AoA must be made to obtain an approximation for each profile’s performance. Shown in Figure 4.2a on page 32 the AoA is the angle between the chord line and the relative inflow. The latter is difficult to measure through the figures obtained from the CFD software, so an alternative must be found. The installation angle and AoA are closely related, as increasing the AoA by a certain amount increases the installation angle by the same amount.

A workaround is done by selecting three separate profiles, each with a different optimal AoA for maximum lift/drag ratio. A fourth profile is also taken into account, which will act as a “dummy” profile. The dummy profile is introduced to check if an equal optimum AoA also yields the same optimum installation angle. The installation angle is thereafter changed within a range of $\pm 12^\circ$ with a step size of 2° from the blade root pitch angle of $\epsilon = 52.89^\circ$, to see if an optimum installation angle can be achieved within this specific range. The results for the four profiles can be seen in Figure 4.12.

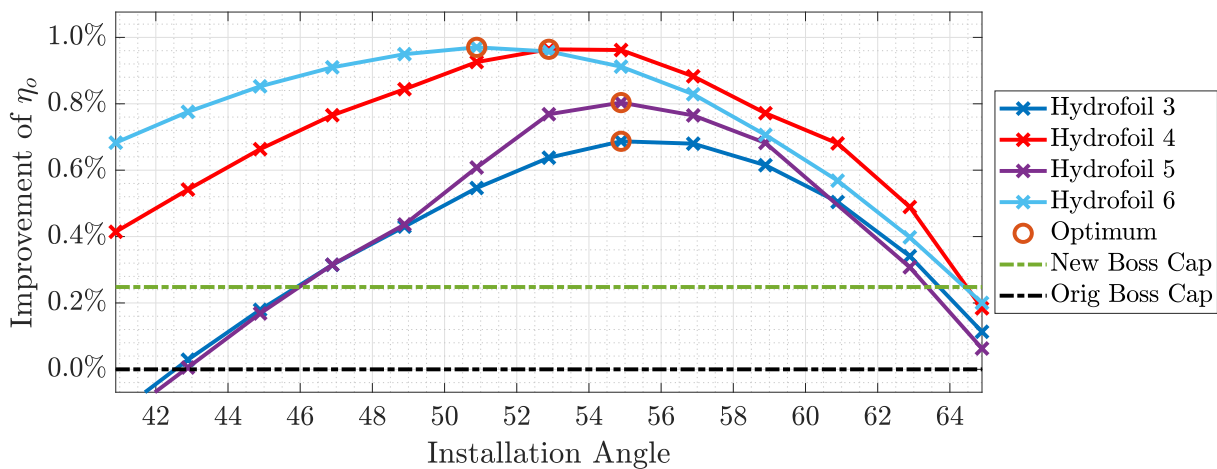


Figure 4.12: Estimation of optimum installation angle for the four selected profiles.

The figure shows that the NACA 4412 profile, which has the largest AoA, is also the profile with the smallest optimum installation angle. Similarly, is the S1223 and CH10 profiles the ones with the most significant optimum installation angle and the smallest optimum AoA. They both have near equal AoA, and their optimum installation angle is the same. Therefore, it is assumed that the installation angle can be chosen to represent the AoA for any of the given profiles. The last profile, E63, has an optimum installation angle just in the near vicinity of the blade root pitch angle, which was the centre-point for the installation angle range. Therefore, it is assumed that the E63 profile's optimum AoA can be converted to an installation angle equalling the blade root's pitch angle of $\epsilon = 52.89^\circ$. In Equation 4.4 a simple correlation converting the optimum AoA of each profile to an estimated optimal installation angle can be found. The equation is based on the E63 profile being equivalent to the blade root pitch angle, and the difference between the E63 profile's AoA and any other chosen profile will be added to the blade root pitch angle to obtain an estimate for the optimal installation angle for each profile.

$$\alpha_n = \epsilon + \text{AoA}_{E63} - \text{AoA}_n \quad (4.4)$$

here α_n is the installation angle for n'th profile, AoA_{E63} is the optimum AoA for the E63 profile, and AoA_n is the optimum AoA for the n'th profile.

Comparison of Hydrofoils

Equation 4.4 has been applied to each profile, and the corresponding estimate of each individual profile's optimum installation angle have been determined, as seen in Table 4.5.

Table 4.5: Estimated optimum installation angle for each profile.

Profile Name	Rectan- gular	AH-6-40-7	Bergey BW-3	CH10	E63	GOE 79	NACA 4412	cp-100- 050-gn	20-32C	S1223
Profile Sim. Number [-]	0	1	2	3	4	5	6	7	8	9
AoA for Max C_L/C_D [°]	-	4.8	5.0	3.5	5.3	5.5	8.5	11.0	3.8	3.3
Estimated Optimum Installation Angle [°]	-	53.4	53.1	54.6	52.9	52.6	49.6	47.1	54.4	54.9

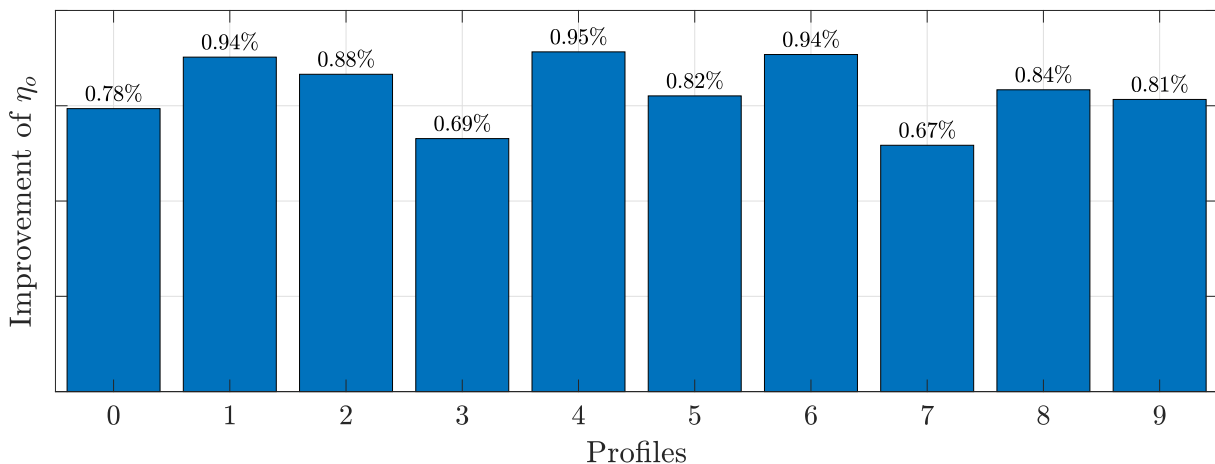


Figure 4.13: The 10 different profiles simulated with their respected estimated optimal installation angle.

Each hydrofoil will be simulated with their respective estimated optimal installation angle and compared with one another to investigate which hydrofoil yields the highest increase in efficiency. The results obtained from the simulations are visualised in Figure 4.13.

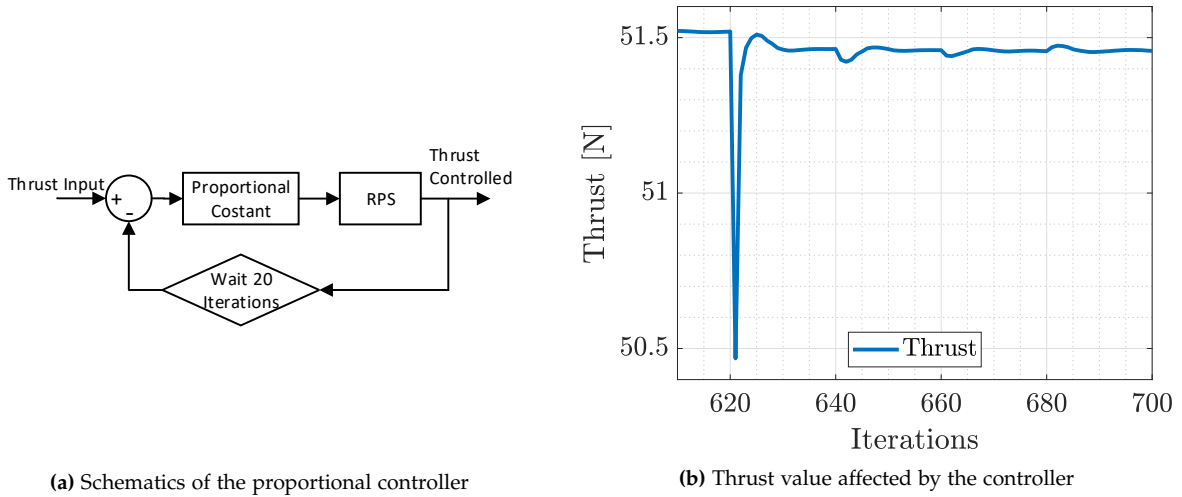


Figure 4.14: The controller implemented for the control of the rotational velocity.

As seen in Figure 4.13 the profiles perform differently when applied to the PBCF at their optimal installation angle. Even though Equation 4.4 implies some uncertainties for the given profiles at their respective installation angle, three profiles still result in a significant increase in efficiency. It is assumed that the uncertainty for each profile by applying the equation can not justify the poorer performing hydrofoils, and these will therefore be disregarded. Comparing the rectangular profile to the hydrofoils tested, it is clear that an increase in efficiency can be gained by applying hydrofoils instead of the traditional rectangular profile.

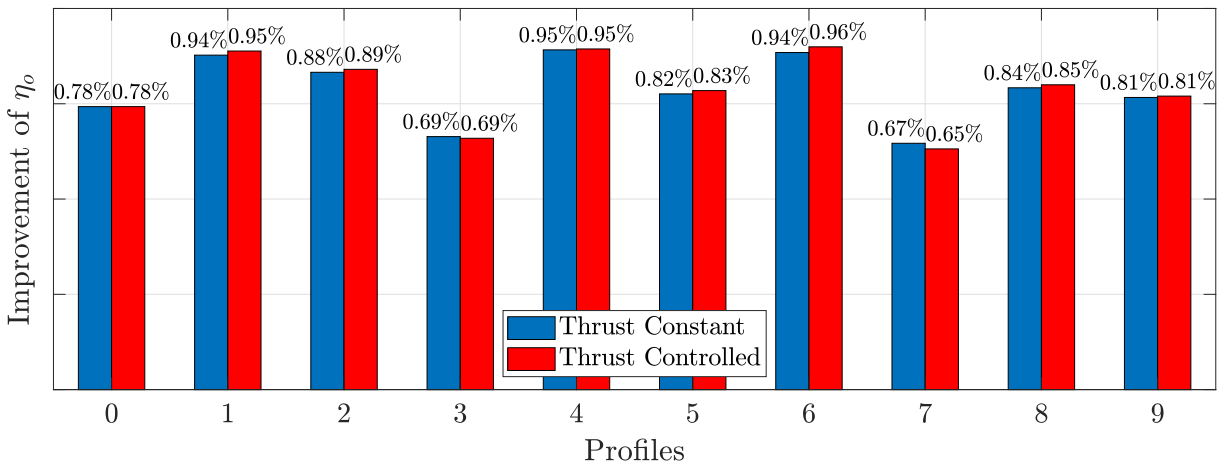


Figure 4.15: Updated efficiency increase from each profile, when applying the thrust controller.

The increased efficiency gained from the implemented hydrofoils is partly due to an increased thrust. In order to properly compare the profiles to the boss cap without implemented PBCF and to compare them with each other, the thrust must be equal. This is done by decreasing the propeller’s rotational velocity, thus lowering the forward motion of the propeller. A simple proportional controller is used for this purpose, where the difference between the thrust of

the propeller with the PBCF and without is used to alter the rotational velocity. This happens every 20 iterations after the simulation has reached a steady-state at iteration 600. By doing this throughout 200 iterations, a thrust very similar to that of the propeller without the PBCF is achieved. For the thrust in Figure 4.14b a value of 51.46 N is desired to achieve. The first time the controller is activated is at 620 where a relative big reaction is seen due to the controller. The thrust stabilise over the next 20 iterations where at 640 a new input is given by the controller. This precedes until iteration 800 where a thrust value of 51.4594 is achieved.

By implementing the thrust controller on profiles, slightly different results occur. These are shown in Figure 4.15 where small variations are visible when comparing with Figure 4.13. Profile 6 are now the one with the highest efficiency after lowering the rotational velocity accordingly to the original boss cap. The reason behind this can be found by inspecting the torque and thrust coefficient shown in Figure 4.16. Profile 6 has the highest thrust coefficient before the implementation of the controller, and the rotational velocity is thus possible to lower more than the others, which improves the efficiency. Profile 4 which gives a high efficiency improvement as well, can be seen to rely mostly on lowering the torque coefficient instead of increasing the thrust coefficient.

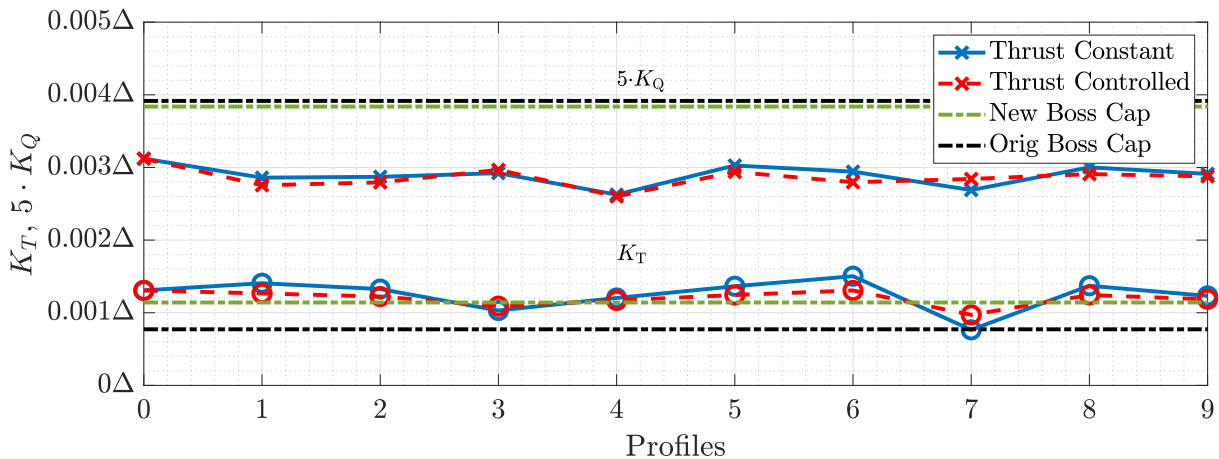


Figure 4.16: The constant and controlled thrust visualised.

Optimal Installation Angle for Profile 1, 4, and 6

Profile number 1, 4, and 6 all lie within the same efficiency increase, making it difficult to choose one over the other. Especially when taking the uncertainty of applying Equation 4.4 into account, their individual estimated optimal installation angle may be or lie close to the implemented. Final testing regarding these three hydrofoils will therefore be conducted to determine the correct optimum installation angle.

In Figure 4.17 the results for changing the installation angle of the three best performing hydrofoils are shown. The determined optimum installation angle for each hydrofoil and their respective increase in efficiency are found in Table 4.6. After implementing the correct optimum installation angle for each hydrofoil, a similar performance is still present. It should be noted for the measured improvements that the number of significant digits might be more detailed than what can be expected from the model but is stated in order to be able to distinguish the three profiles from each other.

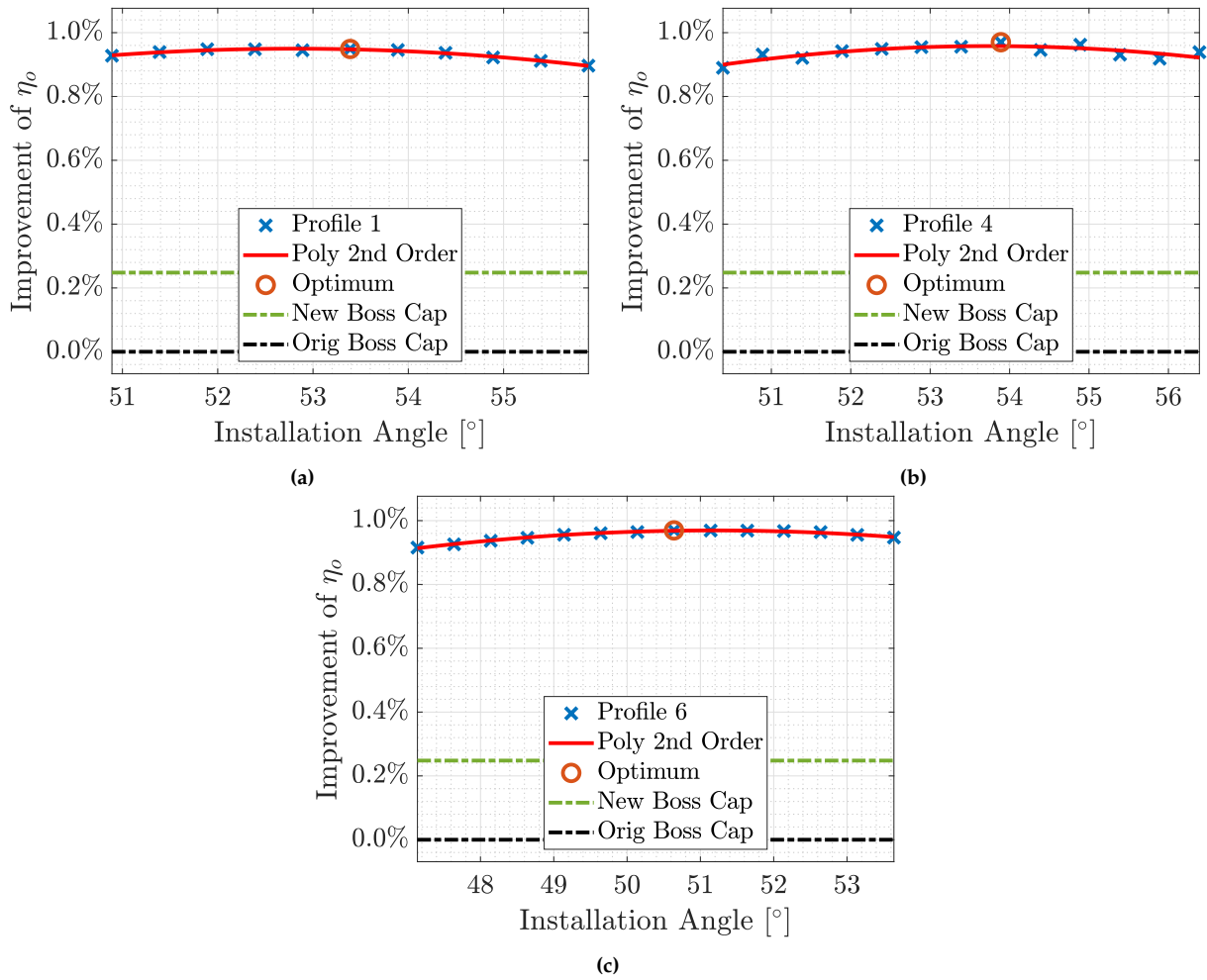


Figure 4.17: Tuning of installation angle, for the three best performing hydrofoils.

Table 4.6: Improvement compared to the original boss cap, where p.p. is percentage points.

Profile	1	4	6
Installation Angle	53.39°	53.89°	50.64°
Improvement	0.949 %	0.969 %	0.970 %
Improvement p.p.	0.6627	0.6771	0.6775

Profile number 6 (NACA 4412) is chosen as the hydrofoil used for the parametric study and individual parameter optimisation in the following sections. As mentioned prior, each profile can be seen in Figure B.1 on page 87. Here it can be seen that the NACA 4412 in Figure B.1g is much sturdier than the other two best performing hydrofoils, which provides even further justification for implementing this hydrofoil over the others. The NACA 4412 has a maximum thickness of 12 % of the chord length, which is a fairly large measure. Therefore, it could be an interesting parameter to investigate, as decreasing the maximum thickness of the hydrofoil yields a smaller surface area. As already stated, a smaller surface area should yield a reduction in torque, as the resistance should be reduced. Likewise, the NACA 4412 hydrofoil performed the best when analysing each of the three hydrofoils' optimum installation angles.

4.4.3 Number of Fins

As stated throughout various literature, the number of fins should be kept equal to the number of propeller blades. However, some authors have had success applying more fins than the number of propeller blades (see e.g. Katayama et al. [2015]) to the boss cap. Therefore, it will be investigated if the number of fins should be kept equal to the propeller blades or if another configuration could yield better results.

In Figure 4.18 the results of changing the number of fins from two to eight can be seen. It is evident that equalising the fin and blade number has the highest efficiency gain and will be utilised in the following sections. The largest number of fins tested was eight, which achieved the second highest increase in efficiency, which was also expected. Four fins are still positioned in the same manner as for the simulation with just four fins, but four extra have been placed in between for eight in total. The geometry of the four fins installed in-between could require a different geometry to optimise their hydrodynamic performance. A smaller span height and chord length could be interesting to investigate regarding the eight fins, which could yield an increase to the eight similar fins. As no slipstream from the blades is present for the extra four fins, their contribution to reducing the hub vortex must be negligible.

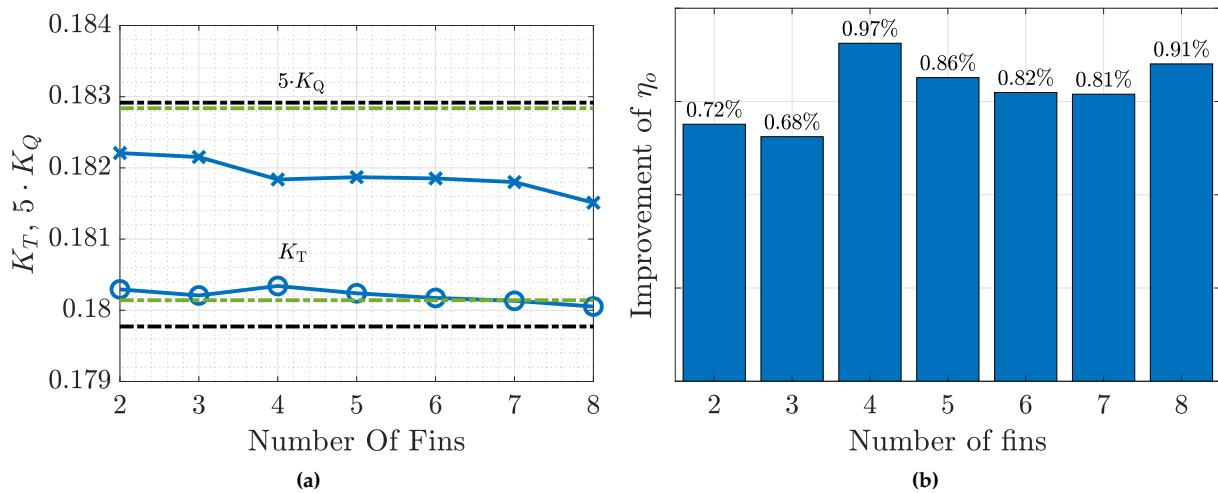


Figure 4.18: Results obtained from the number of fins analyses.

4.4.4 Mirrored

Though not stated in the literature, it was suggested by MAN Energy Solutions Frederikshavn that mirroring the fin profiles should mitigate the induced hub vortex downstream. This was thought since mirroring the profile would align the trailing edge of the fins more with the flow direction, which should weaken the vorticity generation of the rotating propeller/boss cap.

The mirroring of the NACA 4412 hydrofoil is visualised in Figure 4.19, where the normal and mirrored installation can be seen. The mirroring has been done about the chord line. Mirroring the fins about the chord line produces an entirely new hydrofoil, which can not be compared directly with the original NACA 4412. Though none of the defining parameters of the NACA 4412 profile is changed (chord length, maximum thickness, camber position, and camber), it can still be seen as the camber is negative due to the mirroring.

Because of the generation of a new hydrofoil, the installation angle should be investigated

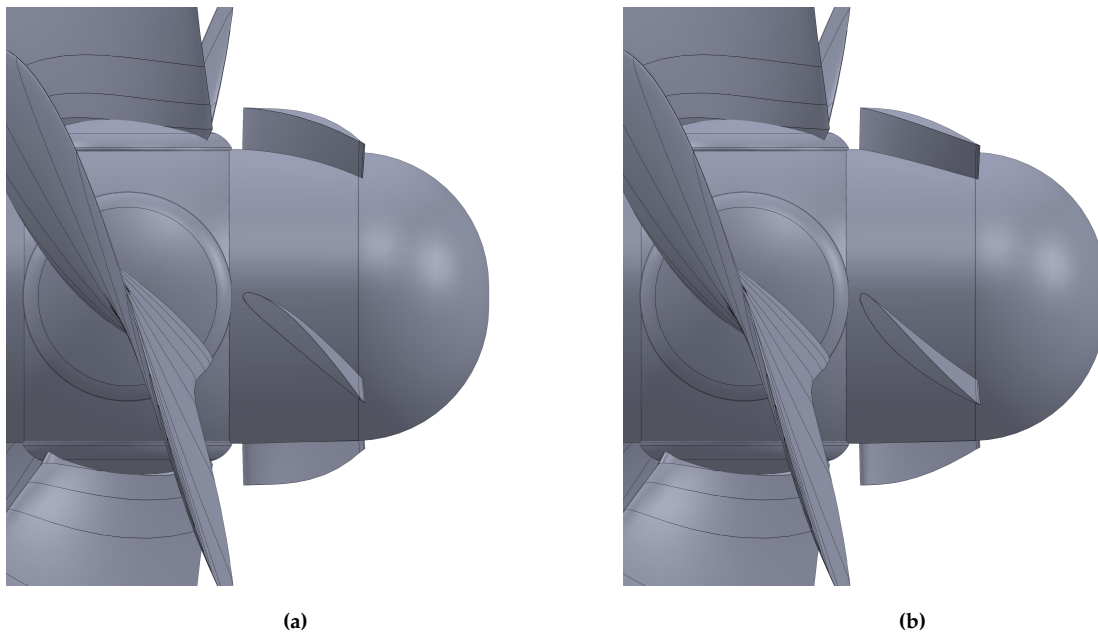


Figure 4.19: Figure of the non-mirrored and mirrored design.

to obtain the best performing configuration for the fins. The range of installation angles that have been tested has been done by “trial-and-error”. Due to no present data on mirrored NACA 4412 hydrofoil, the range has been increased until a satisfactory data set was achieved. The results of changing the installation angle can be seen in Figure 4.20, where the optimum installation angle is found to be $\alpha = 44^\circ$.

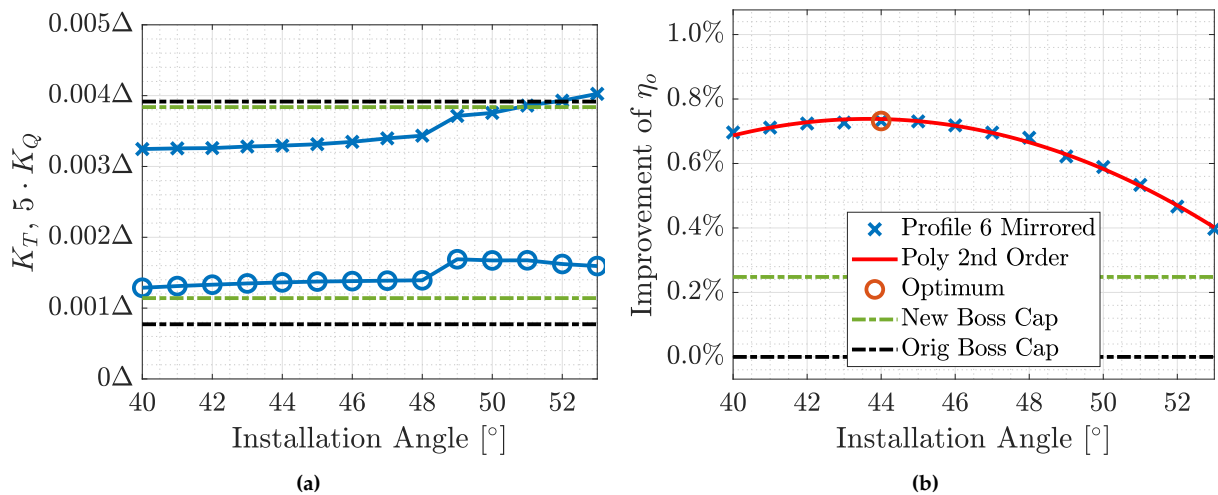


Figure 4.20: Variation in installation angle results from mirroring the NACA 4412 about the chord line.

Comparing the maximum gained efficiency from changing the installation angle of the mirrored fin in Figure 4.20, and the maximum efficiency gained for the original configuration in Figure 4.17, the mirrored fins’ performance is inferior to the original configuration. The non-mirrored hydrofoil and the mirrored yields a maximum efficiency of 0.97 % and 0.73 %, clearly indicating the superiority of the original configuration.

Mirroring the hydrofoil produces an entirely new profile, as mention prior. This implies that the initial values stated in Table 4.3 should be reconsidered as they do not comply with the new configuration. Here, it is believed that a change in the circumferential position of the fins could promote a better hydrodynamic performance by the fins, as the slipstreams from the blades' interaction with the fins could be improved by investigating this parameter.

Therefore, the fins' circumferential position has been varied within the range of 4 mm to 16 mm with a step size of 2 mm. The results obtained from the variation of the circumferential position of the mirrored fin are seen in Figure 4.21.

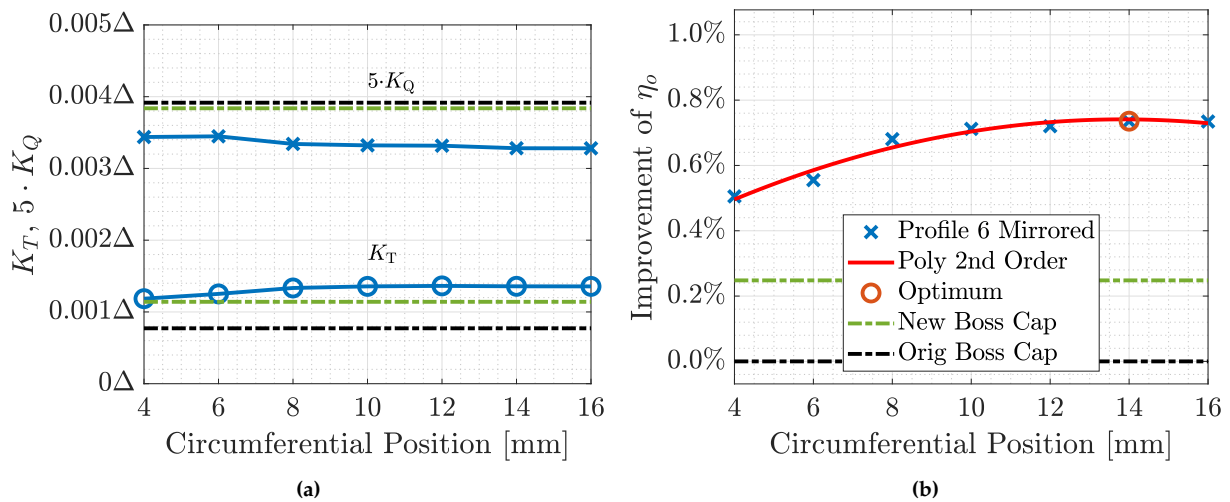


Figure 4.21: Results from the circumferential position variation with the mirrored NACA 4412 hydrofoil.

From Figure 4.21b it is evident that the variation of the circumferential position could not promote the performance of the mirrored hydrofoil sufficiently, and the mirrored design has therefore been discarded.

4.4.5 Rectangular and Base Design Comparison

As a result of investigating the Rectangular Base Design, shown in Figure 4.10, it was found that some basic configurations regarding the implementation of the fins should be changed to obtain a better performing PBCF. Firstly, the fins have been arranged perpendicular to the boss cap surface curvature. Secondly, the traditional rectangular profiles were replaced with the NACA 4412, which construction and performance were superior to the other profiles tested. Lastly, the number of fins should indeed equal the number of propeller blades, and the mirrored NACA 4412 performed inferior to the traditional NACA 4412. Applying these settings results in the Base Design utilised for the parameter study in the next chapter. The Base Design is visualised in Figure 4.19a.

An analysis of how the greater hydrodynamic performance is achieved for the base design will be conducted. This is done by comparing the Rectangular Base Design presented in Figure 4.10 on page 45 with the newly tuned Base Design by pressure contour plots. C_p contour plots of both the rectangular and base design are seen in Figure 4.22a and 4.22b from a side view perspective. The reason for the better performing base design cannot be distinguished from these figures, as only the pressure at the stagnation points for each profile is changed. As seen in the figures, the pressure on the pressure side of the profiles seems equal, indicating that the performance improvement must come from a pressure change on the suction side of the

profile. The suction side of the rectangular and base design profiles are visualised in Figure 4.22c and 4.22d. A lower pressure contour on the suction side of the NACA 4412 hydrofoil is clearly, which indicates that a larger thrust is generated due to the pressure difference between the pressure and suction side, equalling the superior performance.

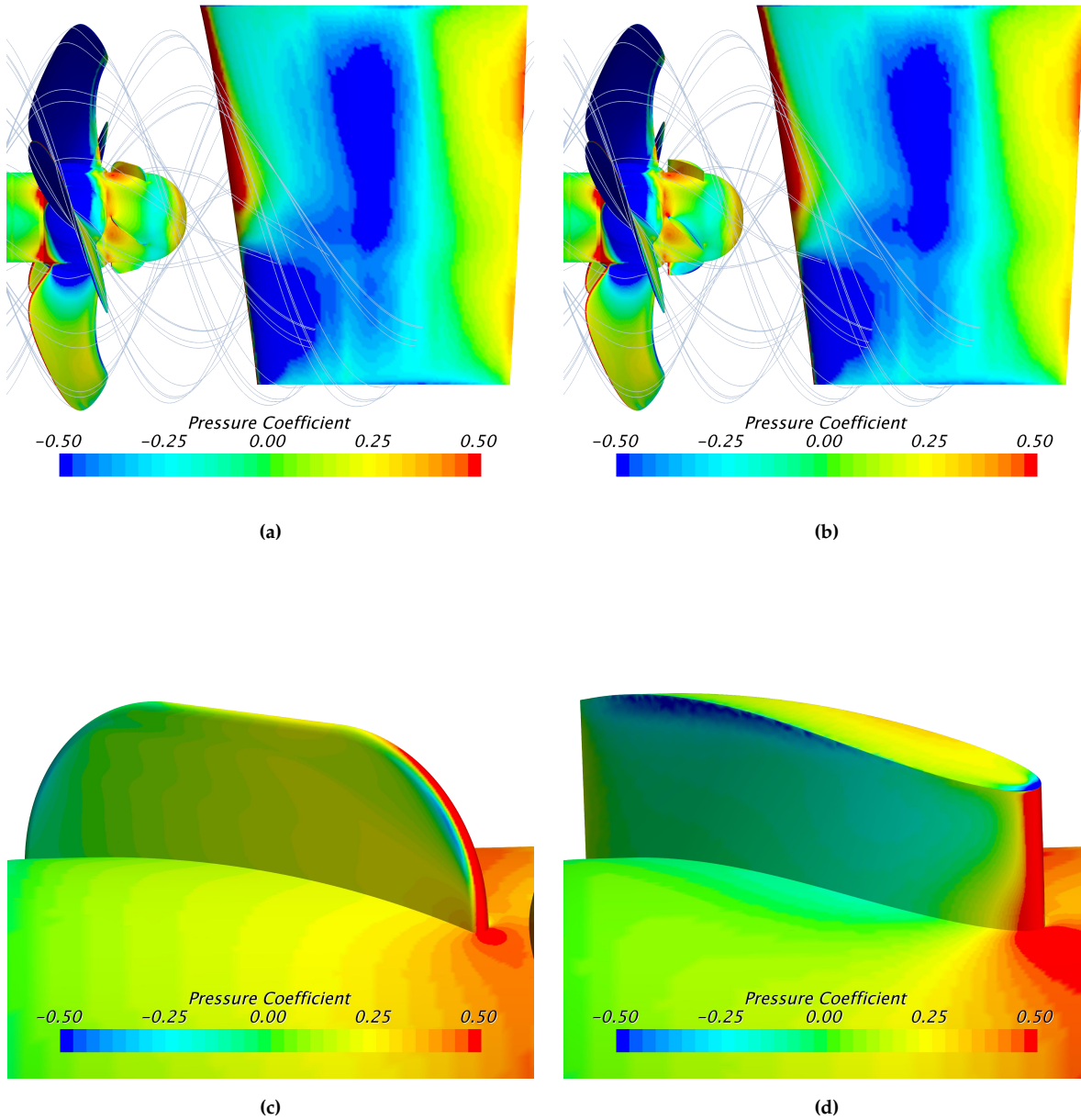


Figure 4.22: C_p contour plot comparison of the rectangular and base design, where (a) and (b) is a side view of the rectangular and base design, respectively, and (c) and (d) a suction side view of the fins from the rectangular and base design, respectively.

Chapter 5

Parameter Study and Optimisation of PBCF

This chapter presents a parameter study on the geometry of the PBCF. An optimised design is presented and compared with the propeller without the PBCF attached.

5.1 Parameter Study

Through the comparison presented in the previous chapter, profile 6 has been found to result in the greatest efficiency increase, as stated in Section 4.4.2 on page 51. This hydrofoil is from the NACA four-digit series, where the specific profile is called NACA 4412. For further improvement of the hydrodynamic performance, a parameter study of the geometrical shape of the fins will now follow. The resulting design that was determined in the last part of the previous chapter is stated in Table 5.1 and is referred to as the “Base Design”. These values will be kept at the Base Design value while one of the other parameters are varied within the stated range. For all the variations, the same ship speed is applied, and the thrust of the propeller is controlled to equal the thrust of the original boss cap, by adjusting the propeller’s rotation speed.

The PBCF with the minimum and maximum value of the range stated in Table 5.1 as well as the optimum value found in the parameter study, are visualised in Appendix C on page 88.

Table 5.1: Base values obtain from the Rectangular Base Design and the variation range of each parameter.

Design parameters	Base values	Range	Step Size
Geometry			
Span Height [mm]	7.5	3 to 12.5	0.5
Chord Length [mm]	27	17 to 37	1
Rake angle [°]	0	-30 to 40	5
Naca Profile³⁾			
Camber [%]	4	0.5 to 9.5	0.5
Camber Position [%·10]	4	2 to 9	0.5
Max Thickness [%]	12	5 to 20	1
Installation Position			
Circumferential position [mm]	10	-2 to 20	2
Axial Position [mm]	7	-5 to 14	1

3) % of the chord length.

5.1.1 Geometry

The primary geometric parameters are first investigated, including the span height, chord length, and rake angle.

Span Height

In the patent by Ogura et al. [1987] the inventors obtained the highest increase in efficiency at a diameter ratio (D_{PBCF}/D_p) of 0.23 and stated that for a considerable increase in efficiency, the diameter ratio should not exceed 0.33. Other authors like Gaggero [2018] and Seo et al. [2016] obtained similar results, where an optimum diameter ratio was found to be approximately 0.25. Therefore, the span height will be varied accordingly, but with a range over the condition of 0.33, to evaluate if the condition stated can be supported.

The result of varying the span height of the PBCF fins are shown in Figure 5.1, where the torque and thrust coefficients are shown in Figure 5.1a and the efficiency is shown in Figure 5.1b. A second-order polynomial is fitted to the efficiency data and can describe the data quite well, though some deviations are present. The vertex of the polynomial is located at 8.1 mm, though the simulation conducted for 7.5 mm yields higher efficiency. Thus, the polynomial will solely be used to indicate a trend and not be utilised to optimise the design.

The diameter ratio at a span height of 7.5 mm is measured to ≈ 0.30 , which is considerably above the stated authors' optimum (measured between two opposite leading edges). This is mainly due to the boss cap utilised in this project having a larger diameter, yielding the fin root placement further from the shaft axis. As shown in Table 4.1 on page 32, the boss ratio is ≈ 0.23 through this project, where a boss ratio of 0.18 were applied by both Gaggero [2018] and Ogura et al. [1987]. Therefore, the results obtained through this section are not possible to compare directly with the literature but was below the condition of 0.33 set by the inventors. A diameter ratio of ≈ 0.33 was equivalent to a span height of 11 mm, which still contributes to increased efficiency. Though the span height should be given great attention, as it evidently yields a great impact on efficiency.

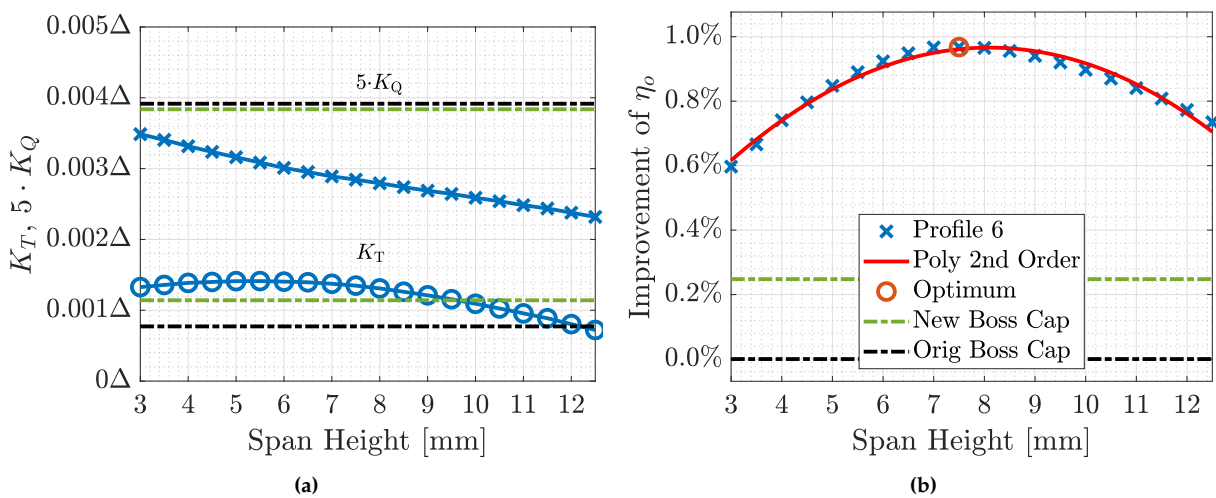


Figure 5.1: Span height investigation.

Maximum efficiency increase at 7.5 mm of 0.6759 p.p. or 0.9677 % compared to the original boss cap.

The torque coefficient is descending as the span height of the fins is increased, while the thrust coefficient increases when the span is altered from 3 to 6 mm and descends after that as well.

This results in an efficiency where the optimum is in the centre of the range due to the balance between a low torque coefficient and a high thrust coefficient. Compared to the original boss cap, the efficiency increase equals 0.6759 p.p. (percentage points) or 0.9677 %.

Chord Length

As mentioned in Section 4.2.3 beginning on page 37 the chord length yields great impact upon the defining profile parameters (max. thickness, camber, and camber position), as they are defined as a percentage of the chord length. The optimum chord length was found to be $0.12D_p$ by both Ogura et al. [1987] and Gaggero [2018], and by Mizzi et al. [2017] to be $0.06D_p$.

A continuing decreasing tendency for the lower range of chord lengths tested was found, which indicated that further reduction was unnecessary. The final interval tested ranged from approximately $0.075D_p$ to $0.164D_p$, which therefore did not include the chord length of $0.06D_p$ determined by Mizzi et al. [2017].

The trend of the efficiency when changing the chord length follows a second-order polynomial as well as for the span height. However, the fitted polynomial is more compressed in the y-direction, indicating that the exact value of chord length is less critical when optimising the PBCF fin design, though this depends on the chosen range and step size as well. The optimum chord length is $l_c \approx 0.13D_p$ (i.e. 30 mm), which is in good correlation with the literature. Applying the chord length of 30 mm results in an efficiency increase compared to the original boss cap of 0.6826 p.p. or 0.9773 %. It can be seen that the chord length yields a higher absolute efficiency than the span height. This is due to the fact that the optimum span height was already chosen for implementation of the base values, where by varying the parameter, only a smaller efficiency can be gained.

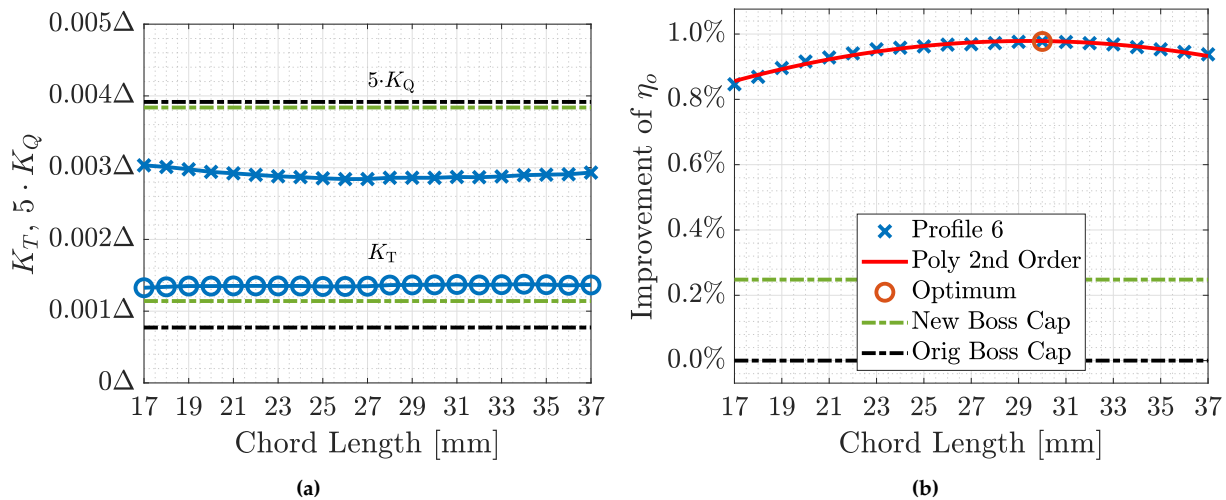


Figure 5.2: Chord length investigation.

Maximum efficiency increase at 30 mm. of 0.6826 p.p. or 0.9773 % compared to the original boss cap.

Rake angle

As stated in Table 1.2 only four studies have researched the rake angle. The last two studies by Hsin et al. [2008] and Katayama et al. [2015] have failed to state their final measure of the parameter, and from the visualised PBCF in these studies a direction of the rake angle cannot be distinguished. In the study by Ouchi et al. [1988] the researchers found an optimum rake angle of -30° by only varying the parameter in three steps: 30° , 0° , and -30° . The paper by

Lim et al. [2014] yields inconclusive results regarding the parameter, as its likewise varied in three steps: 10° , 0° , and -10° . They conclude that the rake angle is insignificant, and from their stated results a clear tendency is not observed. The effect of increasing or decreasing the rake angle results in both increased and decreased efficiency depending on what values were chosen for the other geometrical parameters. In order to fully understand the influence of the rake angle more research is needed to gain a sensible understanding of the implementation hereof. Studies with smaller step sizes should be conducted and the interdependence on the other fin parameters needs to be explored carefully to fully describe the trend of the rake angle.

In this study the efficiency decrease when a negative value is implemented, while an increase in efficiency is gained when a positive angle is chosen. This is due to the torque coefficient which increases towards the ends of the range and has the lowest value at 10° , while the thrust coefficient increases when the rake angle increases. An optimum is thus found at 30° as seen in Figure 5.3b, where the efficiency increase compared to the original boss cap is 0.6968 p.p. or 0.9973 %. This is not in accordance with the results conducted by Ouchi et al. [1988] where a negative rake angle gives an increase in efficiency, but the results conducted by Lim et al. [2014] show that the influence of the rake angle cannot be seen as an isolated parameter, but is dependent on the other fin parameters.

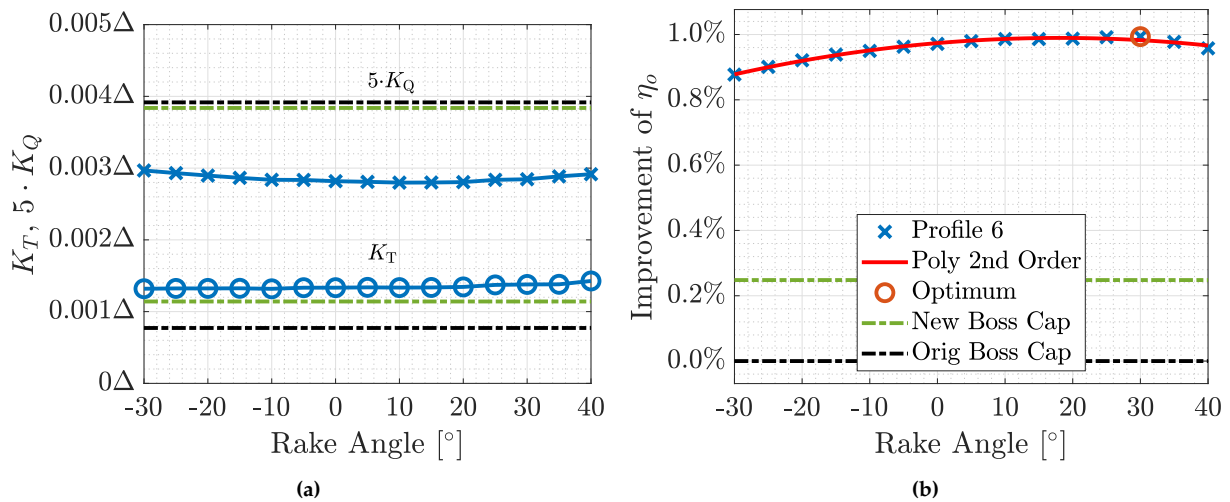


Figure 5.3: Rake Angle investigation.

Maximum efficiency increase at 30° of 0.6968 p.p. or 0.9976 % compared to the original boss cap.

5.1.2 NACA 4412

The NACA hydrofoil can be altered by three properties indicated by the four-digit series designation. These resemble the camber, camber position, and max thickness in that respective order.

Camber

In the paper by Majumber and Maity [2020] the authors investigate variations of the camber. They investigate a constant maximum thickness of 12 % and camber position of 40 % of the chord, with cambers of 1 %, 2 %, 4 %, and a symmetric foil. They conclude that the NACA 4412 yields the highest increase in efficiency, which was also found in Section 4.4.2 beginning on page 47.

The torque coefficient of the maximum chamber shows a similar trend to the rake angle in the shape of an inverted parabola, while the thrust coefficient decreases as the maximum chamber increases. The balance between a low torque and high thrust is thus reached at a value of 4, in accordance with the study by Majumber and Maity [2020]. A value of 4 % was already implemented in the Base Design, which corresponds to the chamber being 4 % of the chord length. The efficiency increase compared to the original boss cap is 0.6767 p.p. or 0.9687 %.

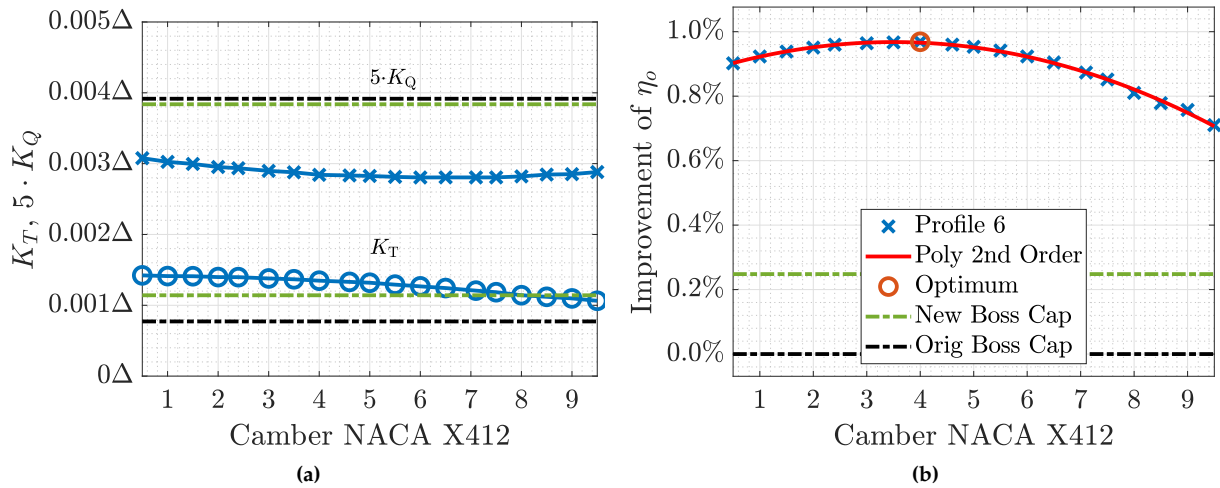


Figure 5.4: Camber investigation.

Maximum efficiency increase at 4 of 0.6767 p.p. or 0.9687 % compared to the original boss cap.

Camber Position

The camber position has not been investigated in the found literature and will therefore be evaluated to gain an understanding regarding this parameter. It is expected that the camber position has minimal effect on the hydrodynamic performance.

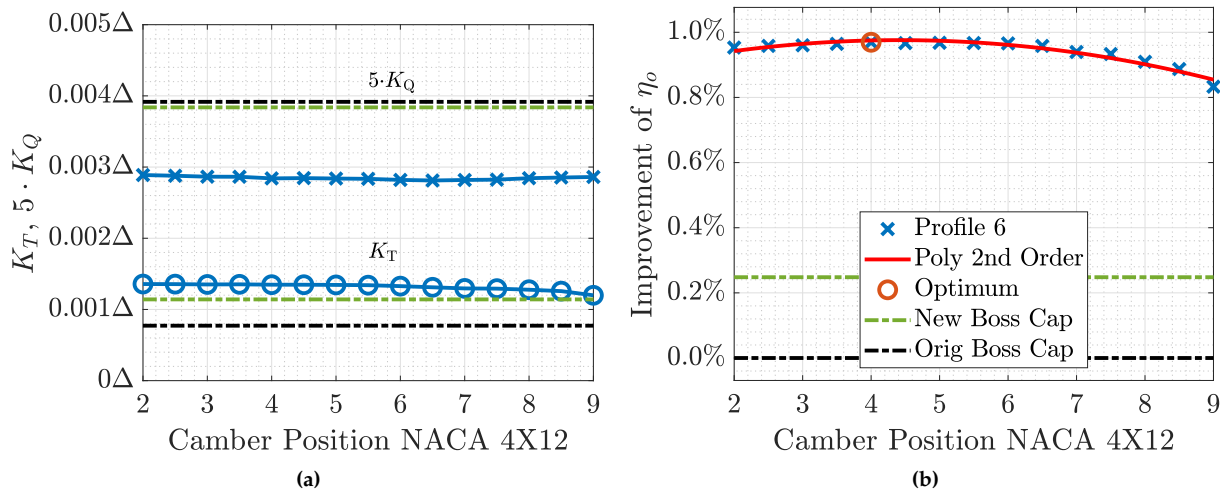


Figure 5.5: Camber Position investigation.

Maximum efficiency increase at 4 of 0.6771 p.p. or 0.9694 % compared to the original boss cap.

The camber position shows a similar trend to the camber through the alteration influences the coefficient less. The optimum is reached at 4, which corresponds to the maximum camber being placed at 40 % from the fin's leading edge. The efficiency increase compared to the original boss cap is 0.6771 p.p. or 0.9694 %.

Maximum Thickness

Few studies are conducted regarding the maximum thickness of hydrofoils, but since a smaller surface area is obtained by decreasing the thickness, it is expected that a gain in efficiency can be achieved. In the PBCF patent by Ogura et al. [1987] the authors chose a constant thickness of $0.01R_p$ (≈ 1 mm at model-scale), where the paper by Mizzi et al. [2017] found an optimal thickness of $0.003R_p$ (≈ 11 mm at full-scale), both utilising the rectangular fin design. None of the two studies took any regards to the sturdiness of the fins, which a yield strength analysis could have provided.

The maximum thickness shows a different trend to the other NACA properties. Here the torque and thrust coefficient increases as the thickness are increased. The torque is increased due to the larger surface area which is a results of increasing the maximum thickness of the profiles. The slope of the torque coefficient is greater than the thrust resulting in the efficiency decreasing as the thickness is increased. It is expected that the efficiency will increase if the maximum thickness is lowered further but is kept at 5 % to ensure that the fins will not fail due to stresses or fatigue. 5 % of the chord yields a maximum thickness of $\approx 0.01R_p$, similar to the chosen value by Ogura et al. [1987]. It could be of great interest to perform a yield strength analysis of the fins to analyse if they can withstand practical operation as well. The efficiency increase at 5 % compared to the original boss cap is 0.7047 p.p. or 1.009 %.

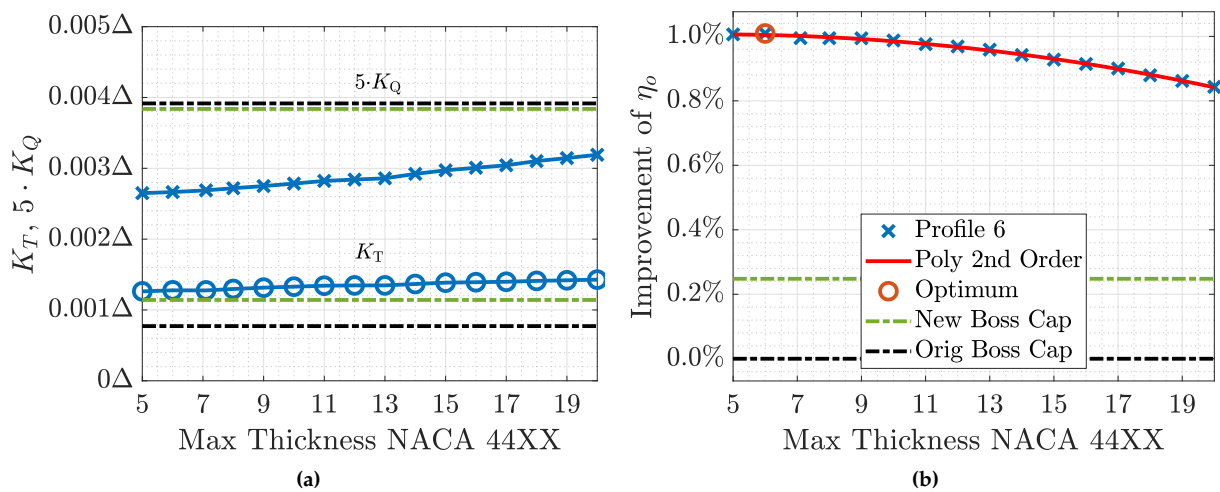


Figure 5.6: Max thickness investigation.

Maximum efficiency increase at 5 % of 0.7047 p.p. or 1.009 % compared to the original boss cap.

5.1.3 Installation position

The installation position are defined by two parameters, the circumferential arc distance and the axial distance, which will be investigated in that order.

Circumferential

The circumferential position has been applied by two different methods in the literature, which was discussed in Section 4.2.4 on page 39. Regardless of the method, applying the phase angle instead of the circumferential arc distance, Ghassemi et al. [2012] conclude that the circumferential position is a critical parameter and largely impacts the performance of PBCF. Authors who utilise the phase angle method can not be compared directly as the angle needs to be converted to an arc distance, but some still implement the latter. Hsin et al. [2008]

did not state their final value but concluded that the circumferential position had little effect on efficiency which disagrees with the former authors. In the patent by Ogura et al. [1987] the authors discuss that the circumferential distance should be kept below $0.14R_p$, which will be evaluated in this section.

Similar to the study by Ghassemi et al. [2012], it is found that the circumferential position has a significant influence on efficiency. Values in the lower and higher range increase the torque and lower the thrust, resulting in significantly decreased efficiency. The position with the highest efficiency is found at 10 mm, where the efficiency increase compared to the original boss cap is 0.6776 p.p. or 0.9701 %.

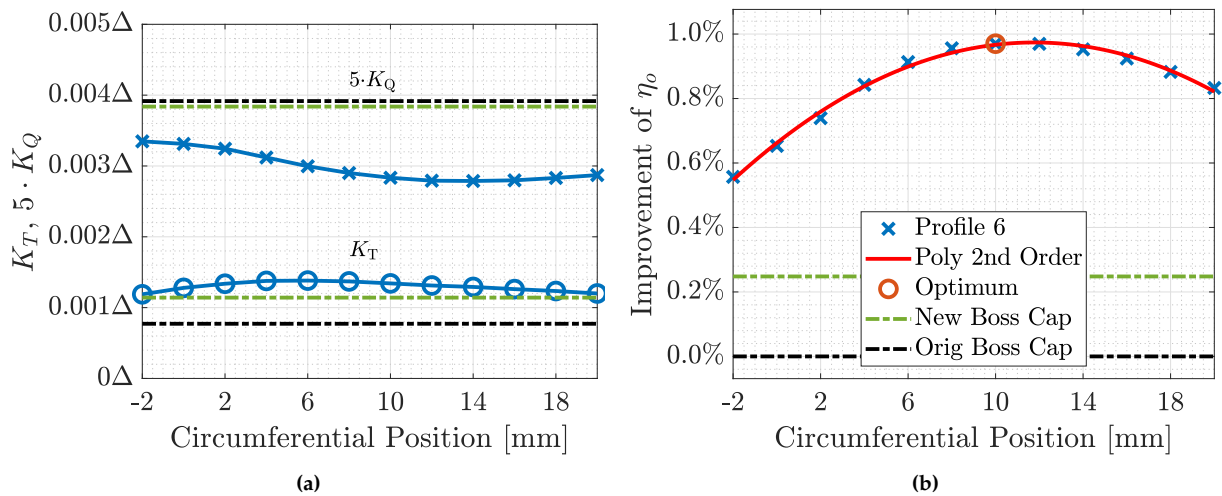


Figure 5.7: Circumferential installation position investigation.

Maximum efficiency increase at 10 mm. of 0.6776 p.p. or 0.9701 % compared to the original boss cap.

Axial

In the paper by Hsin et al. [2008] the authors states that the axial distance should be kept as close to the propeller blade root's trailing edge as possible. They found an optimal axial position at $0.10R_p$, where the inventors in their patent (Ogura et al. [1987]) state that it should be kept below $0.15R_p$.

The axial position has a considerable influence on the efficiency, corresponding to the circumferential position. The thrust coefficient slowly decreases in the upper end of the range, while the torque coefficient rapidly increases as the axial position decreases. This results in a higher torque coefficient and lower efficiency than the original boss cap when the axial position is at -5 mm. The lower range of the tested interval was selected to investigate if an improved interaction between the slipstreams and the leading edges of the fins could be achieved. This was expected as the slipstreams are more concentrated in the near vicinity of the blade's trailing edge, but like seen in Figure 5.8b it only had a decreasing effect. The highest efficiency is achieved when the axial position is 9 mm, resulting in an efficiency increase compared to the original boss cap of 0.6874 p.p. or 0.9842 %. The axial position of 9 mm is equivalent to $0.08R_p$, which is in accordance with the literature.

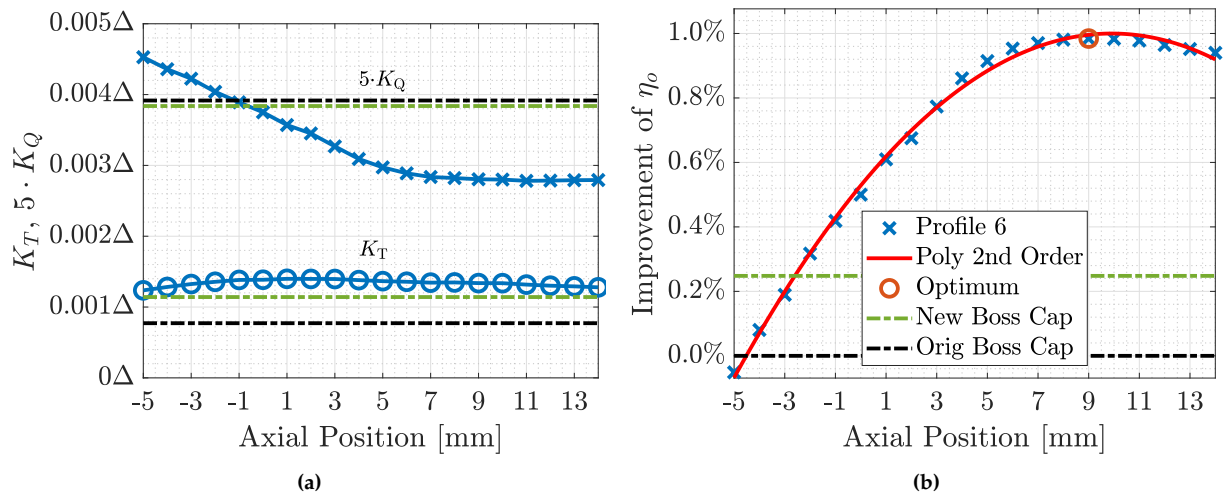


Figure 5.8: Axial installation position investigation.

Maximum efficiency increase at 9 mm. of 0.6874 p.p. or 0.9842 % compared to the original boss cap.

5.2 Optimised Design

The parameter study presented in the previous section has given a thorough understanding of the behaviour of the PBCF. It was possible to determine one value for each variable, which resulted in the highest efficiency increase. For most of the parameters, this was already the chosen parameter for the Base Design. A summary of the Base Design values and the values resulting in the highest efficiency based on the parameter study is stated in Table 5.2. The two

Table 5.2: Measures of each geometrical PBCF parameter obtained from the literature, parametric study, and the optimised design.

Design parameters	Base Design	Parameter study	Optimised Design
Geometry			
Span Height [mm]	7.5	7.5	7.5
Chord Length [mm]	27	30	30
Installation Angle [°]	50.6	50.6	52
Rake angle [°]	0	30	30
Naca Profile⁴⁾			
Camber [%]	4	4	4
Camber Position [%·10]	4	4	4
Max Thickness [%]	12	< 5	6
Installation Position			
Circumferential position [mm]	10	10	10
Axial Position [mm]	7	9	8
Efficiency gain			
Percentage point	0.6759	0.6830	0.7284
Percentage [%]	0.9677	0.9779	1.0429

4) % of the chord length.

columns show that the preferred range and measures of the geometrical variables are well documented and proposed in the literature. The meshing of the fin are shown in Appendix A on page 84.

Only one variable has been varied at the same time, while the other parameters were kept at the Base Design values, thus not taking the interaction between the variables into account. To compensate for this, a new parameter study of each variable has been carried out with a basis in the values stated in the table under "Parameter study". Only the axial position and maximum thickness should be changed for a higher efficiency gain. The maximum thickness should be as small as possible to decrease the torque to the greatest extent. A maximum thickness of 6 mm was chosen for further studies, as the trailing edge of the fin at 5 mm seemed feeble for practical implementation.

The installation angle has been investigated again with the new design, and a value of 52° instead of 51° resulted in the highest efficiency. Lastly, fillets at the base of the PBCF fins is implemented to replicate the welding joints for the fin attachment to the boss cap and improve strength. Likewise, to improve the hydrodynamic behaviour of the flow in this area by avoiding sharp edges resulting in higher efficiency. A comparison of the Base Design and Optimised Design is shown in Figure 5.9.

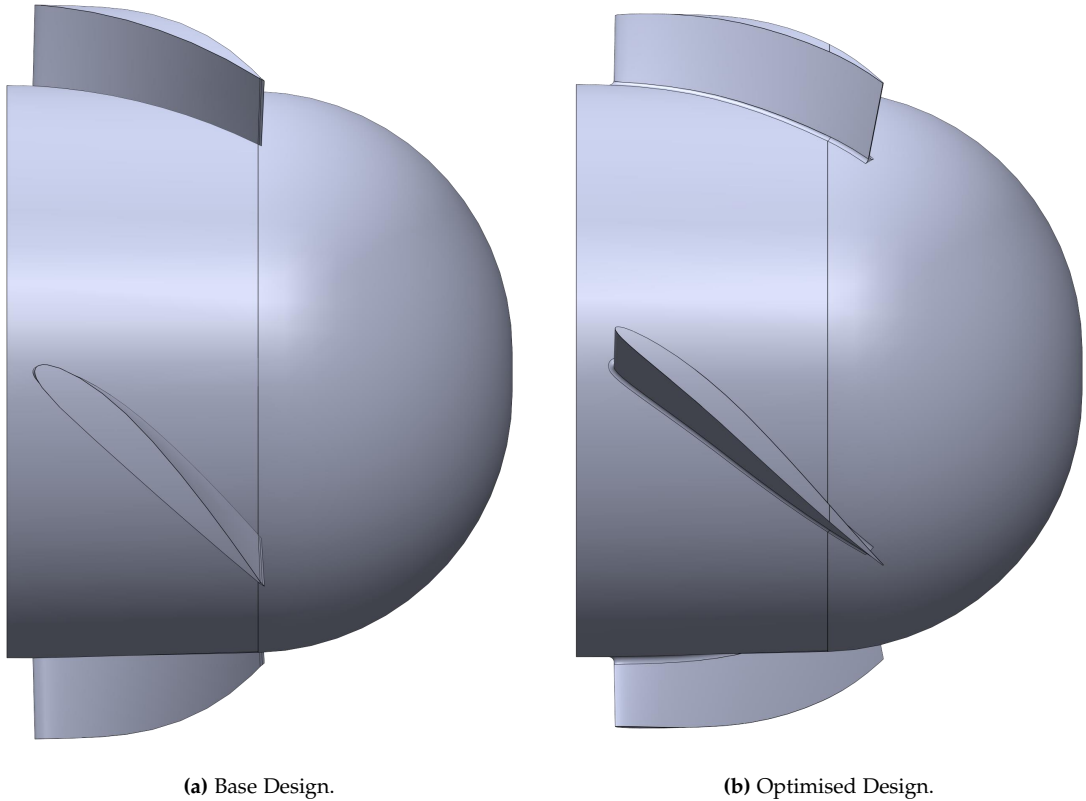


Figure 5.9

A comparison between the pressure distribution with and without the PBCF is presented in Figure 5.10, where the figures without the PBCF initially were presented in Figure 3.14 on page 26. A change in the downstream area of the boss cap is visible when comparing Figure 5.10a and 5.10b as the lower pressure zone is removed. This is a result of implementing the

PBCF, which have changed the flow around the boss cap. The same phenomena are visualised in Figure 5.10c where the lower pressure contour is present at the centre directly downstream of the boss cap, possibly causing a hub vortex, but is removed in Figure 5.10d, where the PBCF is attached. Comparable pressure contour plots can be seen achieved by Sun et al. [2016], who included the rudder as well. The rest of the flow field has not changed significantly, which was not expected from the implementation of a PBCF either.

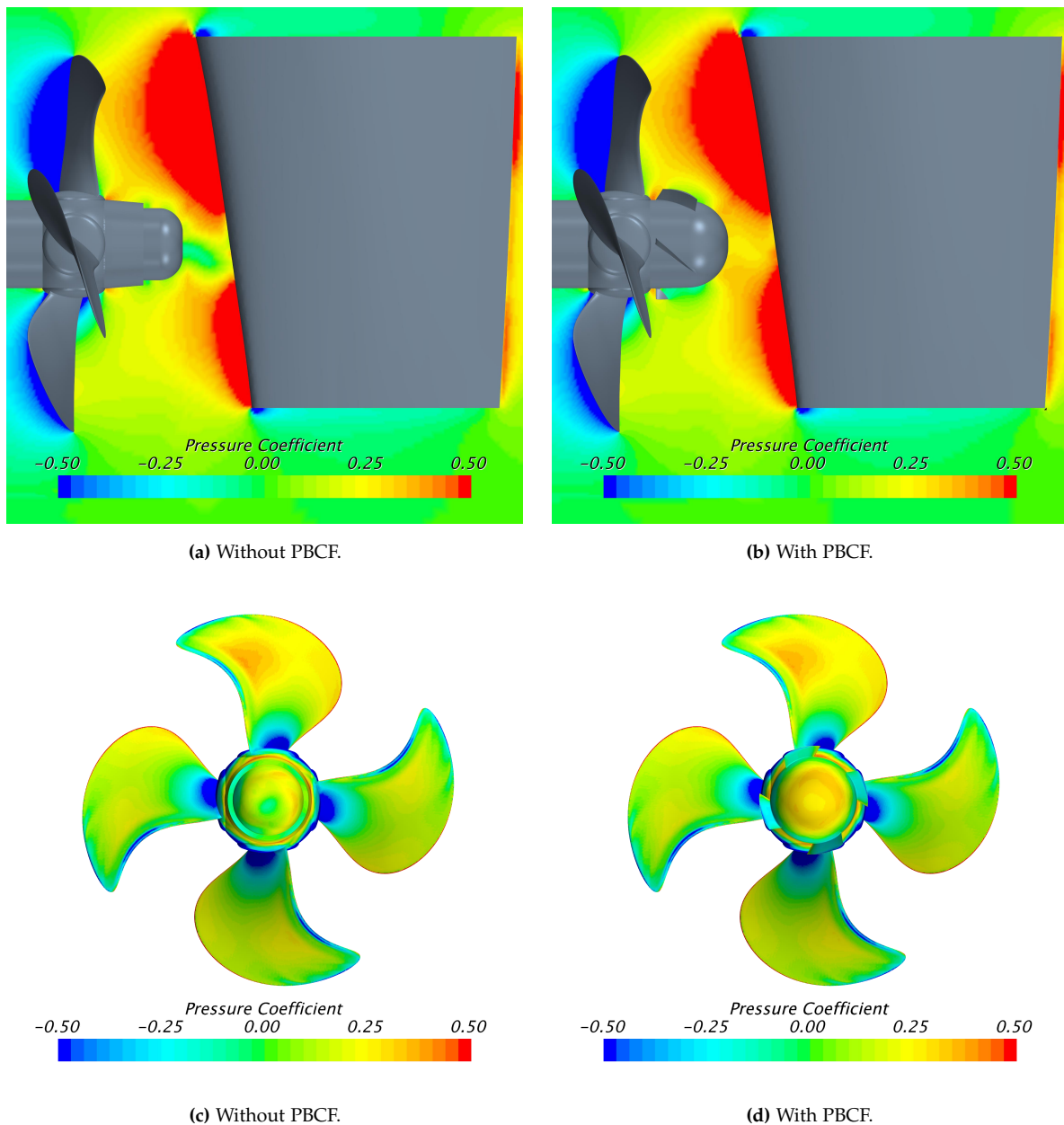


Figure 5.10: C_p contours plots on or around the propeller and rudder, where (a) and (b) are a side view and (c) and (d) are downstream without the rudder visible.

Simulations without the rudder have been conducted to illustrate further the changed flow behaviour caused by the PBCF implementation. These are shown in Figure 5.11, where the low pressure contours without the PBCF in Figure 5.11a is reduced in Figure 5.11b as the PBCF and new boss cap is implemented. The low-pressure contour directly behind the boss cap

indicates the generation of the hub vortex. A lower pressure zone further downstream of the boss cap is still present, which is insignificant as it does not influence the PBCF performance. The pressure coefficient contour figures are in excellent correlation with the literature, as the majority does not investigate the behaviour when the rudder is included. Similar resulting contour plots have been stated in Katayama et al. [2015], where the author likewise achieve increased efficiency by removing the low-pressure zone behind the boss cap by implementing PBCF.

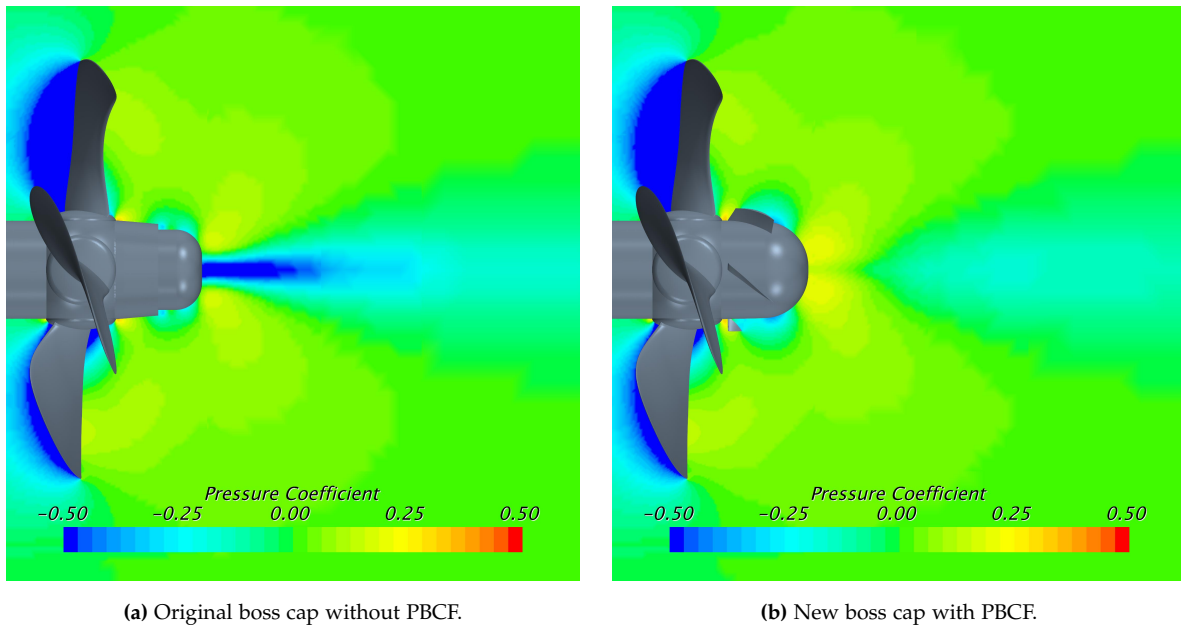


Figure 5.11: C_p contours plots around the propeller without the rudder.

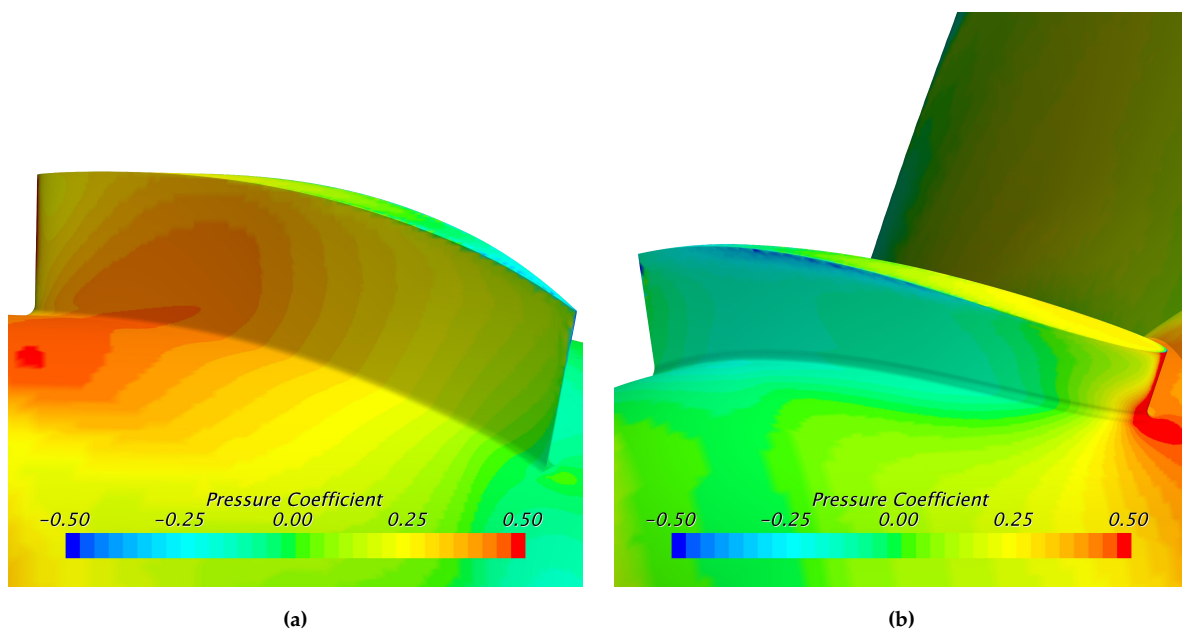


Figure 5.12: Pressure coefficient on or around one PBCF fin where (a) is the pressure side and with flow from left to right (b) is the suction side with flow from right to left.

The pressure and suction side of one PBCF fin are shown in Figure 5.12. A high-pressure zone is present at the fin's leading edge and on the boss cap at the pressure side of the fin. The high pressure on the leading edge is expected but should be decreased as much as possible to reduce drag and further increase efficiency. The streamlines at the leading edge follow the fin profile, which shows that the installation angle is applied correctly.

5.3 Performance of the Optimised Design

An optimised design based on a parameter study is present in the previous chapter. This resulted in an efficiency improvement of 1.04 % when compared to the propeller with the original boss cap. The parameters were carried out with the same ship speed for all variations. However, to gain an understanding of the usage of the PBCF in realistic conditions, a range of ship speeds and advance ratios will be investigated. These will be conducted by simulating the original propeller with the same ship speed and rotational velocity used for the validation simulations presented in Section 3.5.1 and 3.5.2. The propeller with the PBCF attached will be simulated with the same ship speed, but the rotational velocity will be controlled to give the same thrust as the propeller without the PBCF. This results in two sets of simulations (with and without the PBCF) where the ship speed and thrust are equal, and efficiency can thus be compared.

5.3.1 Varying Ship Speed

The ship speed is varied between 2 and 2.5 m/s while the rotational velocity of the propeller is varied accordingly to give a similar advance ratio for all ship speeds for the original boss cap. The rotational velocity of the propeller with the PBCF is controlled to give a similar thrust.

It is evident from Figure 5.13b that the added PBCF shows a similar improvement of efficiency for the entire range of the ship speed and not only for the velocity it was designed for. The thrust coefficient is similar to the original boss cap, while the torque coefficient lowered for the entire range. The efficiency improvement shows that the PBCF can be used in a range of ship velocities while the advance ratio is kept.

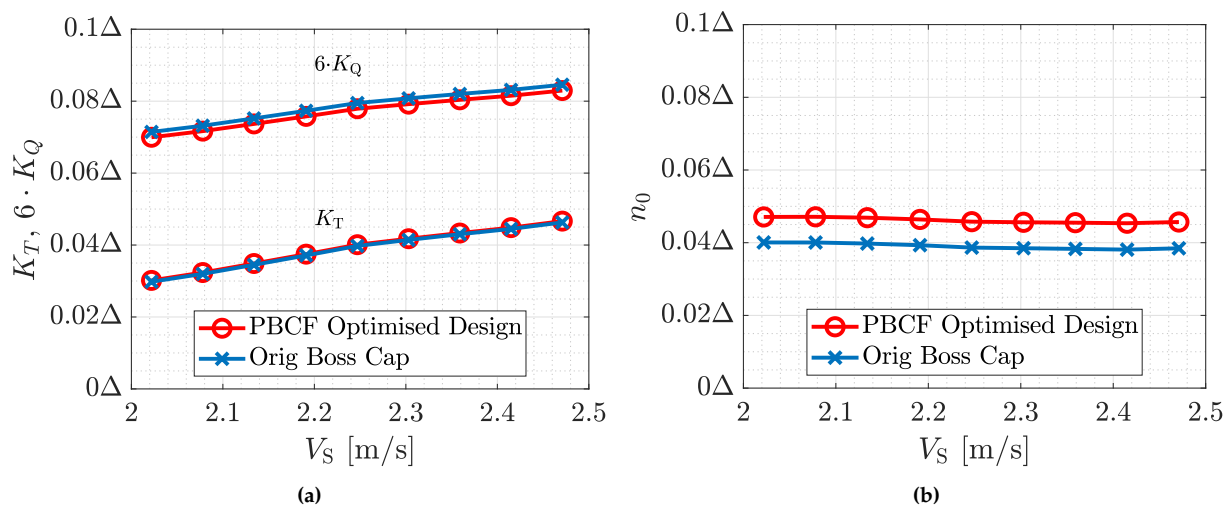


Figure 5.13: Varying ship speed and rps of the propeller resulting in a similar advance ratio.

The improve of the efficiency when attaching PBCF compared to the simulation with out the PBCF is stated in Table 5.3. The improvement is above 1 % for the entire, though a higher improvement is present as the ship speed is increased.

Table 5.3: Improvement of the efficiency when attaching PBCF compared to the simulation with out the PBCF.

V_S [m/s]	2.02	2.08	2.13	2.19	2.25	2.30	2.36	2.42	2.47
η_o [%]	1.0	1.01	1.02	1.01	1.02	1.02	1.03	1.04	1.04

5.3.2 Varying Advance Ratio

For this comparison, a constant rotational velocity is kept while the ship speed is altered, resulting in an advance ratio ranging from 0.3 to 1.0. The propeller with the added PBCF shows an increased efficiency for the entire range. This shows that the advantages of the PBCF is not restricted to the advance ratio used in the parameter study but can be applied to a range of different advance ratios.

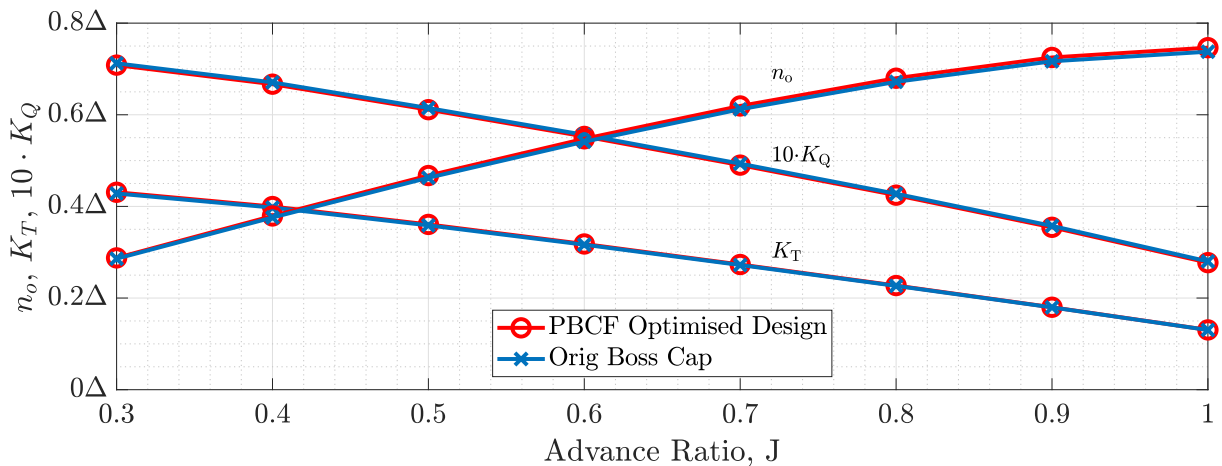


Figure 5.14: Varying ship speed with constant rps of propeller, resulting in a range of advance ratio.

Table 5.4: Improvement of the efficiency when attaching PBCF compared to the simulation with out the PBCF

J [-]	0.3	0.4	0.5	0.6	0.7	0.8	0.9	1.0
η_o [%]	0.59	0.91	1.05	1.18	1.18	1.17	1.16	1.19

5.3.3 Yield Strength Analysis

The yield strength of the optimised design has been tested to ensure that the structure can endure the force applied under normal load. The analysis has been conducted by applying the total X, Y and Z force of one fin at the top of the fin while the rest of the boss cap is stationary as seen in Figure 5.17. This applies the force in the most critical point, thus resulting in a conservative answer of whether the fin structure is going to last. The span height and maximum thickness are two factors that have a big impact on this, and these should thus be altered if the fin is not able to withstand the forces applied to it. The analyses have not been conducted by the authors of the report but are performed by

MAN Energy Solutions Frederikshavn using the software ANSYS. Figure 5.15 show the stress on the fin due to the force applied, where a maximum value is indicated on the figure. It is estimated by MAN Energy Solutions Frederikshavn that the stresses shown are so negligible that no structural fatigue should be a concern for this design. Figure 5.16 where the total deformation is shown further supports this claim as the maximum deformation equals 4.22×10^{-5} mm or 1.6×10^{-4} % of the chord length.

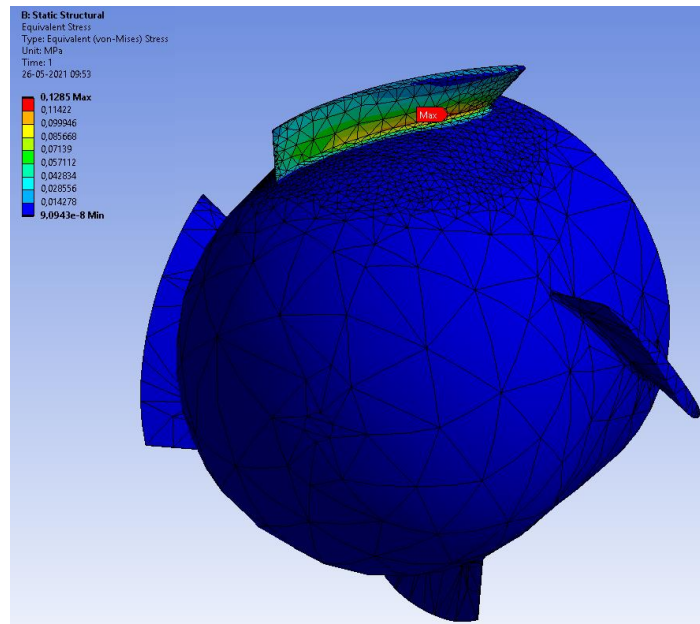


Figure 5.15: Stress due to the force applied.

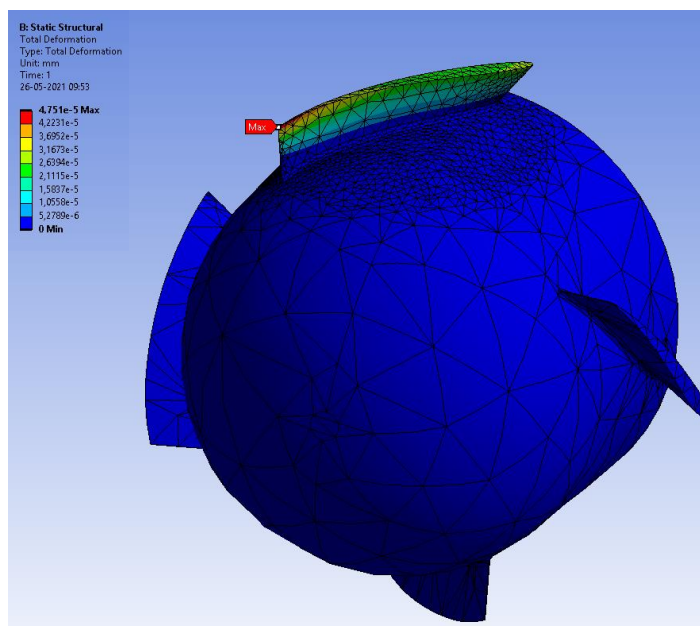


Figure 5.16: Displacement due to the force applied.

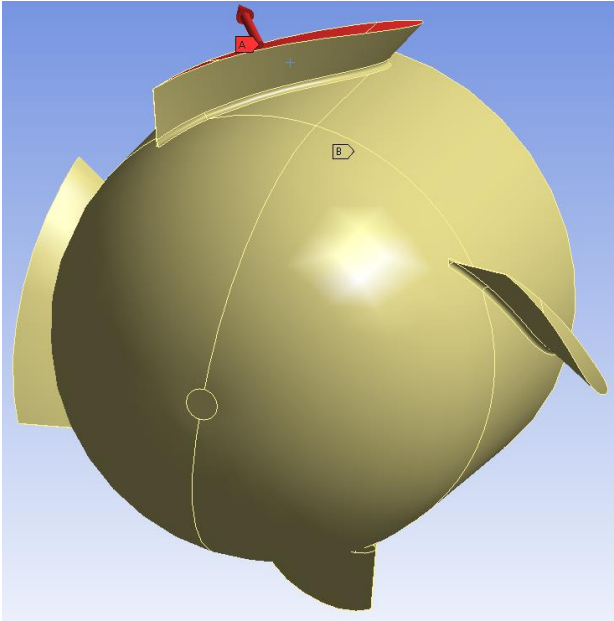


Figure 5.17: Total force on the fin applied to the top in the direction of the arrow.

Chapter 6

Conclusion

Based on the literature, an appropriate computational domain surrounding the propeller was constructed. Meshing models were investigated and compared in order to gain a high-quality grid representing the geometry accurately. By utilising a grid independence analysis, a model independent of the cell count where obtained, with GCI values of 1.9 % and 0.2 % for the parameters studied. By comparing multiple flow related models the first-order segregated model resulted in the lowest residuals and represented the empirical results most accurately. By validating the model with the rudder attached by empirical data, a deviation of maximum 0.5 % for the efficiency was archived.

From the literature study conducted, valuable information regarding the defining geometrical parameters and their measures were obtained. It was discovered that the process of attaching the fins to the original boss cap yielded practical complications due to the fins intersecting the bolt notch. Therefore a new boss cap was designed, yielding an increase in efficiency of 0.17 % when compared to the original. The new design was not able to weaken the hub vortex generation, and PBCF should therefore be attached to mitigate this phenomenon.

The literature study resulted in a rectangular base PBCF design, where the various geometrical parameters were chosen based on the optimised values determined by the different studies. The majority of PBCF research was discovered to be based on a rectangular profile fin design, which was investigated in comparison to nine chosen hydrofoils. It was found that the NACA 4412 hydrofoil had the most significant efficiency gain of the profiles tested and that attaching the fins perpendicular to the boss cap surface curvature throughout the fin span had the highest efficiency gain. It can be concluded that applying carefully chosen hydrofoils instead of the traditional rectangular design yields a considerable gain in efficiency.

The installation angle was investigated due to it being stated as one of the most influential parameters in the designing of PBCF. It was found that the installation angle should be kept in close proximity to the propeller blade root pitch angle, which is in good correlation with the literature. The number of fins was found to yield the highest efficiency increase when they equal the number of propeller blades.

A parameter study was conducted to investigate the geometrical parameters' effect on efficiency. Here the span height, circumferential position, and axial position were the most sensitive parameters when varied, and yielded the highest change in efficiency. These should therefore be considered with great consideration. The optimum value of each parameter investigated was in accordance with the literature. The rake angle resulted in increased efficiency when increasing the angle, which is the opposite of what was found by the inventors. However, another research showed that the effect of the rake angle depended heavily on other fin parameters. Literature regarding the effect of changing the rake angle is limited, thus making it difficult to predict the effect. However, the authors are confident in the results presented in this project due to the small and consistent step size showing a clear trend of the efficiency as a function of the rake angle.

The parameter study resulted in a design based on each parameter's individual performance contribution, which neglected the interaction between the parameters when they are varied. A new parameter study was conducted to analyse the interaction based on the values

Table 6.1: The optimum design values for a propeller with $D_p = 0.23$ m.

Geometry				Naca Profile			Installation Position	
Span Height	Chord Length	Installation Angle	Rake Angle	Camber	Camber Position	Max Thickness	Circumferential	Axial
7.5 mm $0.033D_p$	30 mm $0.13D_p$	52°	30°	4 %	40 %	6 %	10 mm $0.044D_p$	8 mm $0.035D_p$

obtained from the prior. This resulted in minor variations for few parameters, which, when implemented, yielded the optimised PBCF design, with the values stated in Table 6.1. Comparing the original boss cap without PBCF and the optimised design with PBCF attached, it was concluded that an increase of 0.7284 percentage points or 1.0429 % in efficiency was achieved. From visualisation of the pressure coefficient around the propeller, it was evident the a weakened hub vortex in the boss cap end base vicinity had been accomplished.

The yield strength analysis performed by MAN Energy Solutions Frederikshavn concluded that the forces applied on the fin resulted in negligible stresses, which implied that no concerns should be taken in regards to this. This proves that the design have a practical applicability as fatigue is not a concern. The parameter study and optimisation of the propeller geometry have been conducted at one design point not taking varying ship speeds or advance ratio in to account. A variation of these did however show that implementing a PBCF resulted in an increase in efficiency of more than 1 % for all conditions except an advance ratio below 0.5. The implementation of the PBCF is thus advantageous in a wide range of flow parameters.

Chapter 7

Future Works

The implementation of the PBCF has been proven to increase the efficiency of the given propeller by over 1 %. However, this might not be the case for other propellers, as has been stated by other researchers. The efficiency gain depends on the propeller, where older models often have more to gain. An investigation of how the proposed PBCF design will perform with other propellers could give a great insight into the versatility of the design. A parameter study of the PBCF design for each investigated propellers would further heighten the understanding.

The design and optimisation process through this study have been conducted at model-scale, which mentioned by some authors shifts the analysed media towards the laminar region. In addition some authors have conducted research both at model- and full-scale, where a comparison between the two yielded a higher boss drag at full-scale than for model-scale. The boss drag caused by the hub vortex downstream of the boss cap is therefore more significant at full-scale. Investigating the PBCF by a full-scale numerical analysis could therefore yield a greater insight to this phenomena, where the PBCF should perform even greater due to its superior mitigation ability. Similarly, should the PBCF be evaluated through empirical studies, to ensure that the performance determined in this project are accurate when utilised at full-scaled. This could for instance be achieved by attaching the PBCF on the already operating Ro-Ro vessel, and thereafter analysing the vessel's fuel consumption.

The fins were installed perpendicular to the boss cap surface curvature, implying pitching of the fins. The pitching was not evaluated further but would yield valuable insight into the hub vortex's mitigation. The pitch at different radii could be investigated, as some researchers have done, and the results could thereafter be compared. Pitching could probably aid in the position of the stagnation point at the leading edge of the fin, which should be sought to be position on the pressure side.

Likewise, were the chord-to-span ratio neglected through this project but still indirectly applied due to the perpendicular installation of the fins. This resulted in an increased chord length as the span became larger, which likewise could yield great insight and possibly increase efficiency by decreasing the torque implied by a smaller fin surface area.

The parameter study and following optimisation has been conducted through a manual process for each computational result. In order to make the optimisation of a new PBCF feasible, an automatic optimisation algorithm should be created. This would significantly decrease the time and increase the possibility of gaining higher efficiency by further exploring the geometry and interaction of parameters. A Box-Behnken approach would be a great choice as an arbitrary number of factors can be explored following a straightforward and consistent method for determining the optimum value.

Bibliography

- Abar et al., 2018.** I. A. C. Abar, I K. A. P. Utama and M. Iqbal. *An Investigation into the Effect of Slope Angle of Hub Cap Geometry against the Efficiency of Ship Propeller in the Presence of PBCF.* In *Proceeding of Marine Safety and Maritime Installation*, July 2018. doi:10.23977/msmi.2018.82616. Indonesia, Bali.
- Airfoil Tools, 2021.** Airfoil Tools. *Airfoil Tools*, 2021. URL <http://airfoiltools.com/index>. Web page, accessed: 18-05-21.
- Celik, 2008.** Ismail B. Celik. *Procedure for Estimation and Reporting of Uncertainty Due to Discretization in CFD Applications.* *Journal of Fluids Engineering*, 130(8), 1–4, 2008. doi:10.1115/1.2960953.
- Druckenbrod et al., 2012.** M. Druckenbrod, L. Greitsch, S. Bednarek, S. Berger and M. Abdel-Maksoud. *Geometric Modelling for Optimisation of Propeller Hub Caps.* In *15th Numerical Towing Tank Symposium*, pages 58–63, October 2012. Italy, Cortona.
- Druckenbrod et al., 2015.** M. Druckenbrod, K. Wang, L. Greitsch, H.-J. Heinke and M. Abdel-Maksoud. *Development of hub caps fitted with PBCF.* In *Proceedings of the Fourth International Symposium on Marine Propulsors*, pages 393–400, May 2015. USA, Texas, Austin.
- Engpin, 2015.** Brian Engpin. *Terminology: Parts of ships and equipment aboard ships*, 2015. URL <https://maritimesa.org/grade-10/terminology-parts-of-ships-and-equipment-aboard-ships/>. Web page, accessed: 26-05-21.
- Gaggero, 2018.** Stefano Gaggero. *Design of PBCF energy saving devices using optimization strategies: A step towards a complete viscous design approach.* *Ocean Engineering*, 159(1), 517–538, 2018. doi:10.1016/j.oceaneng.2018.01.003.
- Ghassemi et al., 2012.** Hassan Ghassemi, Amin Mardan and Abdollah Ardeshir. *Numerical Analysis of Hub Effect on Hydrodynamic Performance of Propellers with Inclusion of PBCF to Equalize the Induced Velocity.* *Polish Maritime Research*, 19, 17–24, 2012. doi:10.2478/v10012-012-0010-x.
- Hansen et al., 2011.** H. R. Hansen, T. Dinham-Peren and T. Nojiri. *Model and Full Scale Evaluation of a 'Propeller Boss Cap Fins' Device Fitted to an Aframax Tanker.* In *Proceedings of the Second International Symposium on Marine Propulsors*, pages 186–196, June 2011. doi:10.1007/s00773-012-0181-2. Germany, Hamburg.
- Hao-peng et al., 2013.** C. Hao-peng, M. Cheng, C. Ke, Q. Zheng-fang and Y. Chen-jun. *An Integrative Design Method of Propeller and PBCF(Propeller Boss Cap Fins).* *Journal of Hydrodynamics, Ser. B*, 26(4), 586–593, 2013. doi:10.1016/S1001-6058(14)60066-4.
- Haun, 2014.** Eric Haun. *Underwater PBCF Installation in South Korea*, 2014. URL <https://www.marinelink.com/news/installation-underwater374238>. Web page, accessed: 26-05-2021.

- Hsin et al., 2008.** Ching-Yeh Hsin, Bo-Hong Lin and Chung-Ching Lin. *The Optimum Design of a Propeller Energy-Saving Device by Computational Fluid Dynamics*. *Computational Fluid Dynamics*, 1(1), 655–660, 2008. doi:10.1007/978-3-642-01273-0_87.
- IMO, 2020.** International Maritime Organization IMO. *Energy Efficiency Measures*, 2020. URL <https://imo.org/en/OurWork/Environment/Pages/Technical-and-Operational-Measures.aspx>. Web page, accessed: 09-12-2020.
- Ingen, 2008.** J. L. Ingen. *The eN Method for Transition Prediction. Historical Review of Work at TU Delft*. In *Proceedings of the 38th AIAA Fluid Dynamics Conference and Exhibit*, pages 1–49, June 2008. doi:10.2514/6.2008-3830. USA, Washington, Seattle.
- Jacobs et al., 1933.** E. N. Jacobs, K. E. Ward and R. M. Pinkerton. *The Characteristics of 78 Related Airfoil Sections from Tests in the Variable-Density Wind Tunnel*, National Advisory Committee for Aeronautics, 1933. November, Report No. 460.
- Katayama et al., 2015.** K. Katayama, Y. Okada and A. Okazaki. *Optimization of the Propeller with ECO-Cap by CFD*. In *Proceedings of the Fourth International Symposium on Marine Propulsors*, pages 401–407, May 2015. USA, Texas, Austin.
- Kawamura et al., 2012.** Takafumi Kawamura, Kazuyuki Ouchi and Takeo Nojiri. *Model and full scale CFD analysis of propeller boss cap fins (PBCF)*. *Marine Science and Technology*, 17(1), 469–480, 2012. doi:10.1007/s00773-012-0181-2.
- Kim et al., 11 2001.** W. Kim, Suak Ho Van and D. Kim. *Measurement of flows around modern commercial ship models*. *Experiments in Fluids*, 31, 567–578, 2001. doi:10.1007/s003480100332.
- Lim et al., 2014.** Sang-Seop Lim, Tae-Won Kim, Dong-Myung Lee, Chung-Gil Kang and Soo-Young Kim. *Parametric study of propeller boss cap fins for container ships*. *International Journal of Naval Architecture and Ocean Engineering*, 6(2), 187–205, 2014. doi:10.2478/IJNAOE-2013-0172.
- Majumber and Maity, 2020.** P. Majumber and S. Maity. *Numerical Analysis of Aerofoil Shape Propeller Boss Cap Fin (PBCF) to Improve Propeller Efficiency*. *International Journal of Innovative Technology and Exploring Engineering (IJITEE)*, 9(3), 231–238, 2020. doi:10.35940/ijitee.C8036.019320.
- Maulik et al., 2020.** Romit Maulik, Himanshu Sharma, Saumil Patel, Bethany Lusch and Elise Jennings. *A turbulent eddy-viscosity surrogate modeling framework for Reynolds-Averaged Navier-Stokes simulations*. *Computer & Fluids*, 2020. doi:10.1016/j.compfluid.2020.104777.
- Menter, 1994.** F. R. Menter. *Two-equation eddy-viscosity turbulence models for engineering applications*. *AAIA Journal*, 32(8), 1598–1605, 1994. doi:10.2514/3.12149.
- Mizzi et al., 2017.** Kurt Mizzi, Yigit Kemal Demirel, Charlotte Banks and Osman Turan, Panagiotis Kaklis and Mehmet Atlar. *Design optimisation of Propeller Boss Cap Fins for enhanced propeller performance*. *Applied Ocean Research*, 62(1), 210–222, 2017. doi:10.1016/J.APOR.2016.12.006.

- MOL Techno-Trade, 2015.** MOL Techno-Trade. *Energy-Saving Propeller Boss Cap Fins System Reaches Major Milestone - Orders Received for 3,000 Vessels*, 2015. URL <https://www.mol.co.jp/en/pr/2015/15033.html>. Web page, accessed: 26-05-2021.
- Officer of the Watch, 2020.** Officer of the Watch. *MARITIME DICTIONARY*, 2020. URL <https://officerofthewatch.com/tools/maritime-dictionary/>. Web page, accessed: 26-05-21.
- Ogura et al., 1987.** M. Ogura, H. Koizuka, T. Takeshita, Y. Kohno, K. Ouchi and T. Shiotsu. *A screw propeller boss cap with fins.*, 1987. URL <https://patents.google.com/patent/EP0255136A1/en>. Patent, App. nr.: 87111052.4, Pub. nr.: 0 255 136 A1.
- Ouchi et al., 1988.** K. Ouchi, M. Ogura, Y. Kono, H. Orito, T. Shiotsu, M. Tamashima and H. Koizuka. *A Research and Development of PBCF(Propeller Boss Cap Fins)*. *Journal of the Society of Naval Architects of Japan*, 1988(163), 66–78, 1988. doi:10.2534/jjasnaoe1968.1988.66. Written in Japanese.
- Reynolds, 1895.** Osborne Reynolds. *IV. On the dynamical theory of incompressible viscous fluids and the determination of the criterion*. *Philosophical Transactions of the Royal Society of London*, 186, 123–164, 1895. doi:10.1098/rsta.1895.0004.
- Roache, 1998.** Patrick J. Roache. *Verification and Validation in Computational Science and Engineering*. Hermosa Publishers, 1 edition, 1998. ISBN 9780913478080.
- Seo et al., 2016.** J. Seo, S. Lee and S. H. Rhee. *Influence of Design Parameter Variations for Propeller-Boss-Cap-Fins on Hub Vortex Reduction*. *Journal of Ship Research*, 60(4), 203–218, 2016. doi:10.5957/JOSR.60.4.160003.
- Sun et al., 1 2016.** Y. Sun, Y. Su, X. Wang and H. Hu. *Experimental and numerical analyses of the hydrodynamic performance of propeller boss cap fins in a propeller-rudder system*. *Engineering Applications of Computational Fluid Mechanics*, 10(1), 145–159, 2016. doi:10.1080/19942060.2015.1121838.

Appendix A

Validation of CFD Model

Segregated and Coupled Flow Model Comparison

A comparison between the first- and second-order segregated flow solver and the coupled flow solver is presented in Figure A.1. The three simulations have the mesh and number of iterations. The first-order segregated solver shows the best agreement with the experimental results.

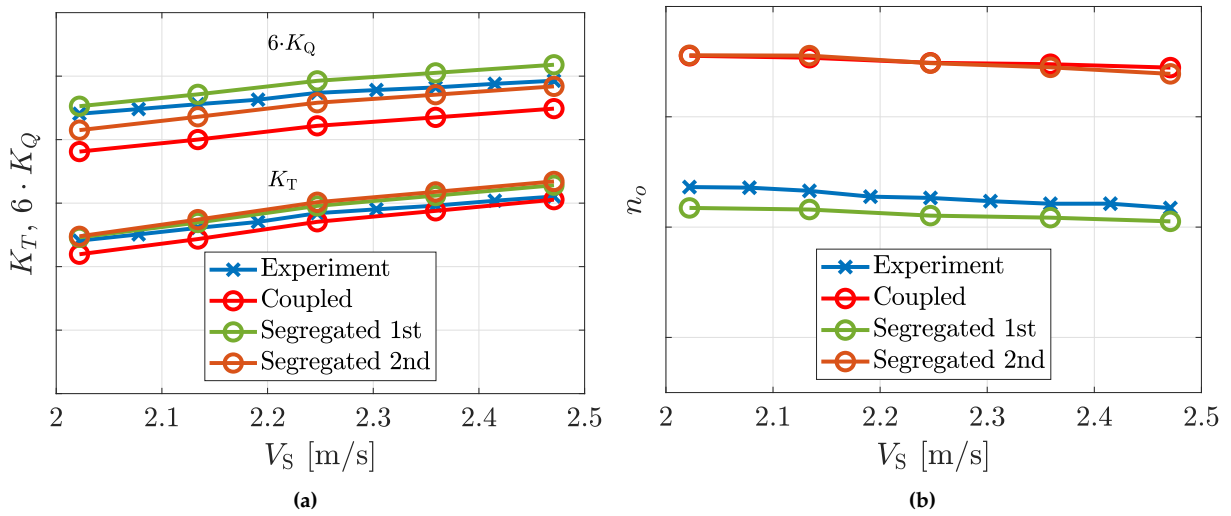


Figure A.1: Comparison between first- and second-order segregated flow solver and the coupled flow solver.

Table A.1: Deviation between the efficiency (η_0) of the simulations and experiments.

V_S [m/s]	2.02	2.13	2.25	2.36	2.47
Segregated first-order [%]	0.5	0.5	0.5	0.4	0.3
Segregated second-order [%]	3.4	3.5	3.5	3.5	3.5
Coupled [%]	3.4	3.4	3.5	3.6	3.6

A comparison of the residuals is included as well. Here it should be noted that the residuals of the segregated second-order solver are a factor of 10 higher than the first-order. The coupled and first-order segregated solver result in similar values though the coupled solver needed 4000 iterations before being stable, resulting in more computational time.

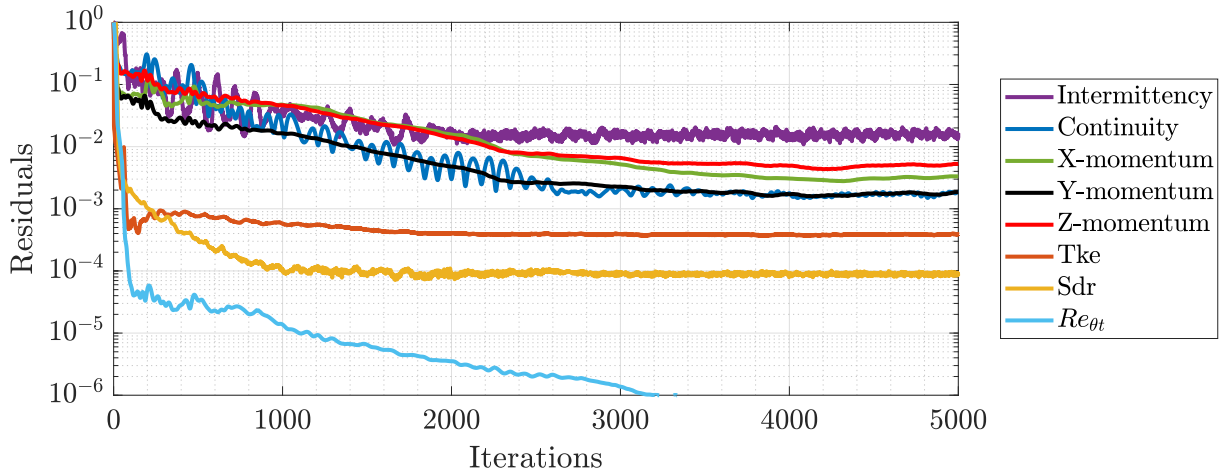


Figure A.2: Normalised global residuals over 5000 iterations for the coupled flow solver.

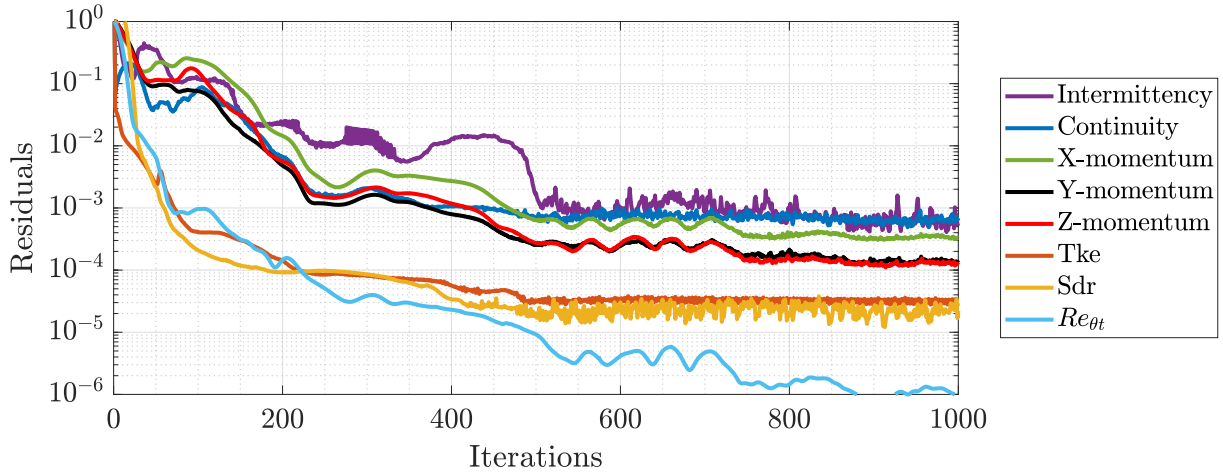


Figure A.3: Normalised global residuals over 1000 iterations for the segregated first-order solver.

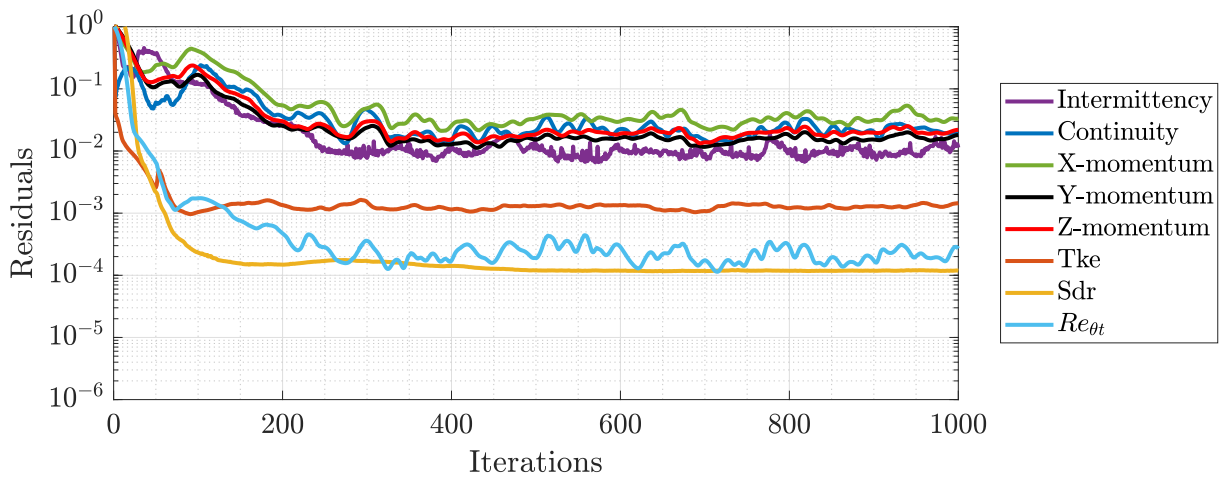


Figure A.4: Normalised global residuals over 1000 iterations for the segregated second-order solver.

Mesh Refinement Comparison

The values chosen in the meshing model are highly determinant for the overall residuals of a computational model. The residuals of the two models will here be compared to show the difference when refining the model. In the less refined model, the default values given in STAR-CCM+ are used except for the cell base size. The final values are determined through an iterative process where a goal of residuals $< 10^{-3}$ were sought. The values for the two models are stated in Table 3.1. The volumetric controls presented in Section 3.3.1 on page 17 are not implemented for the starting model but the same meshing models and solvers are implemented.

Table A.2: Meshing values for the starting model and the final model.

	Starting values	Final values
Number of cells, MRF	6.48×10^6	1.15×10^7
Number of cells, Outer	1.06×10^6	2.66×10^6
Cell base size, MRF	$1.0 \times 10^{-1} D_p$	$8.7 \times 10^{-2} D_p$
Cell base size, Outer	$1.4 \times 10^{-1} D_p$	$1.0 \times 10^{-1} D_p$
Volume growth rate	8 cells pr. layer	8 cells pr. layer
Points in surface curvature	36	36
Surface growth rate	1.1	1.1
Prism layer thickness	$8.7 \times 10^{-4} D_p$	$8.7 \times 10^{-4} D_p$
Number of prism layers	6	18
Prism layer growth rate	1.5	1.1

Residuals

Figure A.6 shows the residuals for the two models with the starting values and the final values, respectively. It can be noted that most of the residuals are decreased by a factor of 10 when the final values are used. However, faster convergence is reached for the model with the starting values.

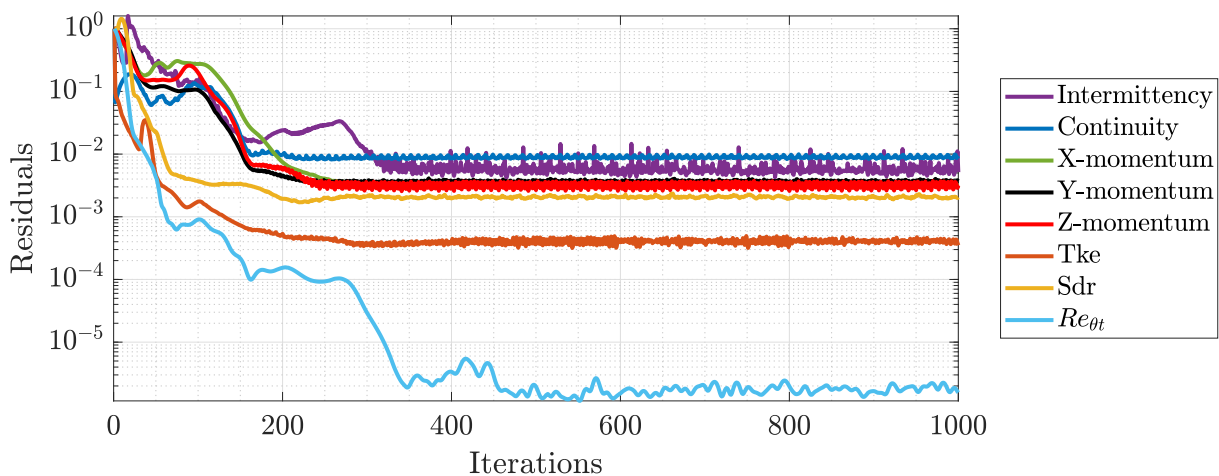


Figure A.5: Residuals with the starting values.

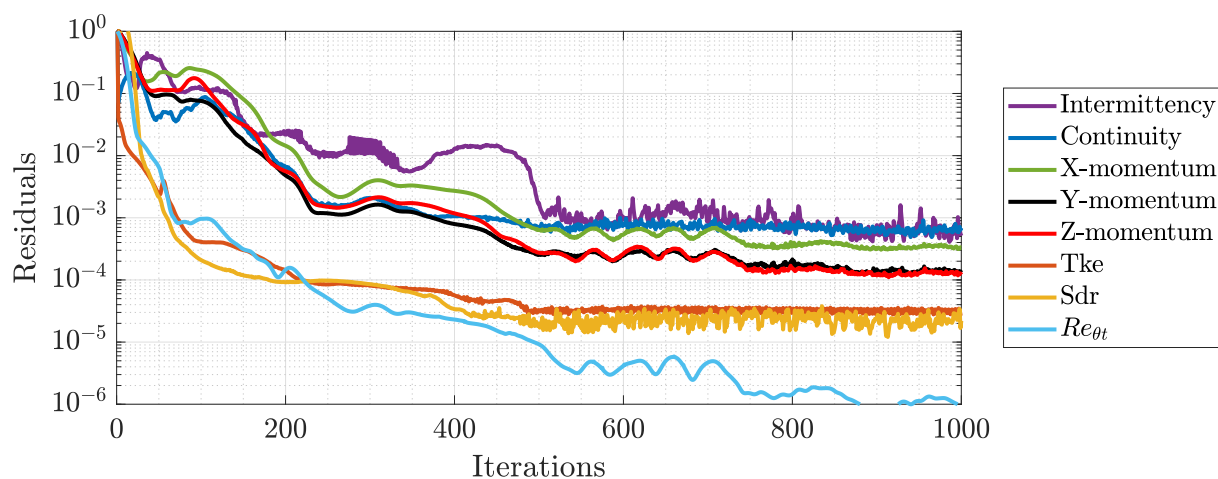


Figure A.6: Residuals with the final values.

Intermittency

Figure A.7 shows cells with intermittency residuals greater than $\pm 5 \times 10^{-6}$. The values are chosen by decreasing the value until only the cells with the highest residuals were present for the model with the starting values as seen in Figure A.7a. The intermittency error occurs at the blade tips, boss cap, and on the rudder for the starting model. This is greatly reduced in Figure A.7b, possibly due to the implementation of volumetric controls in these areas. Further refinement of the mesh on the rudder could lead to lower intermittency residuals.

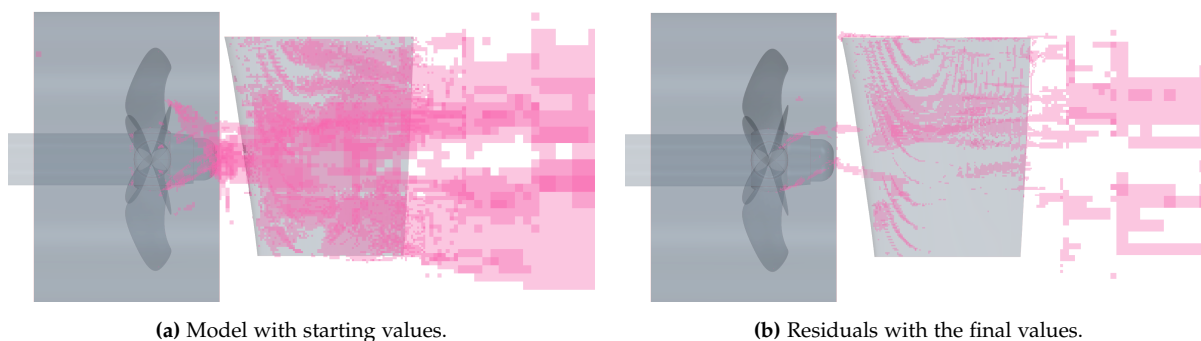


Figure A.7: Cells with intermittency residuals greater than $\pm 5 \times 10^{-6}$.

Mass Imbalance

The mass imbalance mainly shows a problem downstream of the boss cap and at the bottom of the rudder. Big square areas appear, which are cells far away from the propeller. Implementing volumetric controls at the boss cap resolves the problems at the boss cap, while the refinement of the prism layers on the rudder possibly lowers the mass imbalance on this.



Figure A.8: Cells with mass imbalance greater than $\pm 3 \times 10^{-7}$ kg/s.

Momentum

Figure A.9 shows cells with momentum residuals more significant than $\pm 2 \times 10^{-5}$ N. This regards the momentum in both the X, Y and Z direction. The boss cap and the rudders is again an area where residuals are likely to happen. The high residuals appear to travel downstream from the areas where they are formed, affecting the area downstream of the rudder.

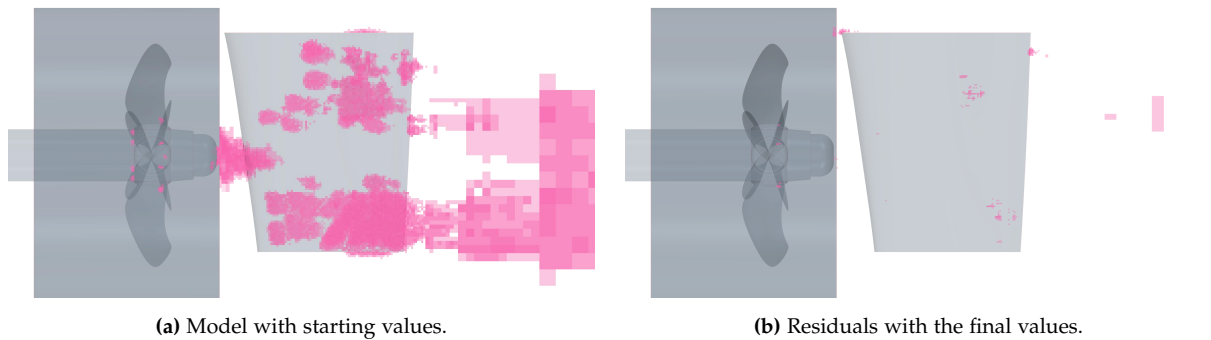


Figure A.9: Cells with momentum residuals greater than $\pm 2 \times 10^{-5}$ N.

Turbulent Kinetic Energy (Tke)

Figure A.10 shows cells with Tke residuals greater than $\pm 5 \times 10^{-5}$. The boss cap and rudder are again the most affected areas. The final model does still have some cells with high Tke residuals downstream but the amount is lowered.

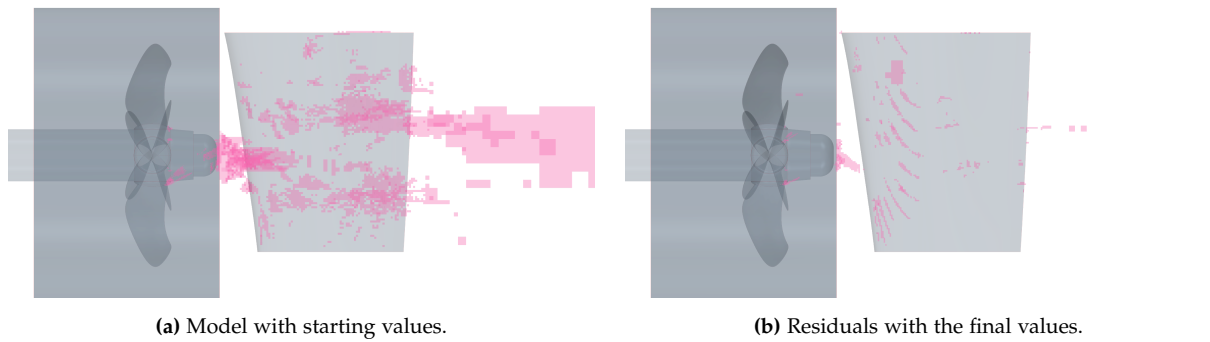


Figure A.10: Cells with Tke residuals greater than $\pm 5 \times 10^{-5}$.

Specific Dissipation Rate (Sdr)

Figure A.11 shows cells with Sdr residuals greater than $\pm 1 \times 10^{-2}$. The boss cap, rudder, and propeller blades' trailing edges are the areas with cells with the highest residuals. The Sdr residuals at the boss cap are lowered in the refined model but the residuals on the rudder appear to be more spread, though the residuals are shown in Figure A.6 are lowered.

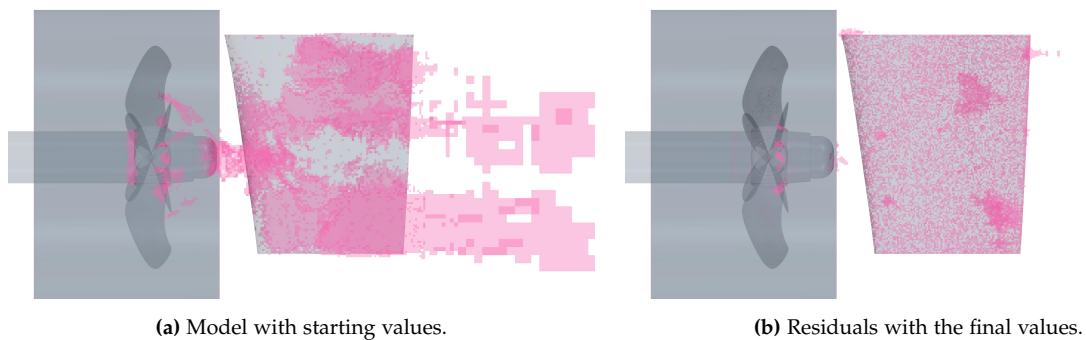


Figure A.11: cells with Sdr residuals greater than $\pm 1 \times 10^{-2}$.

Mesh on PBCF Fins

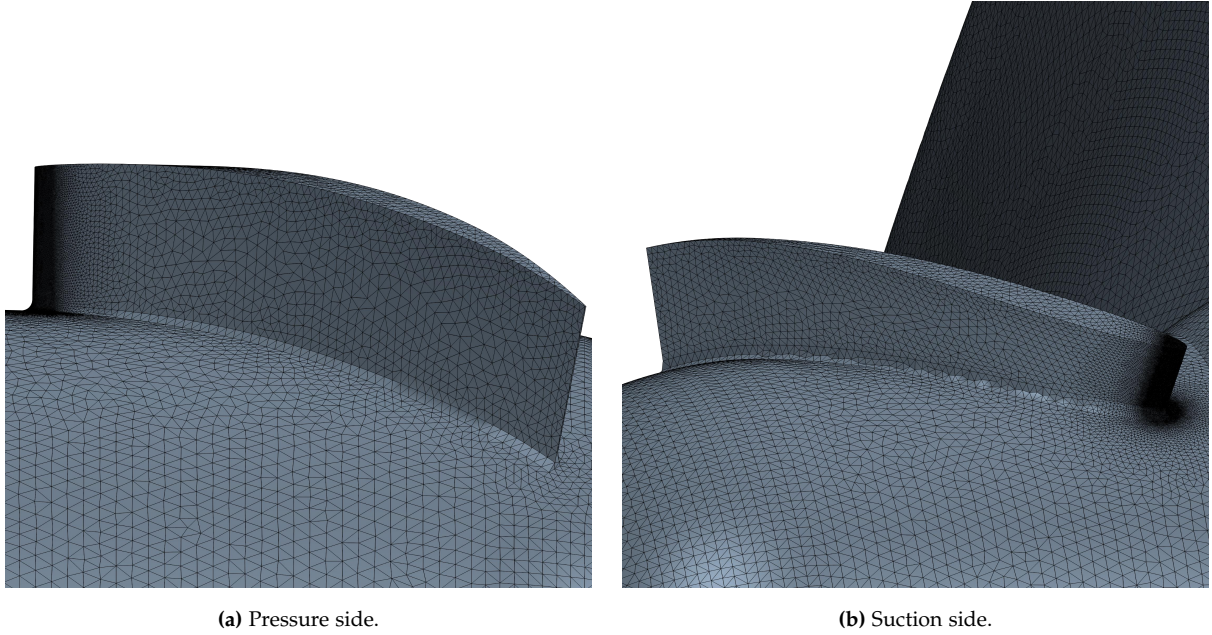
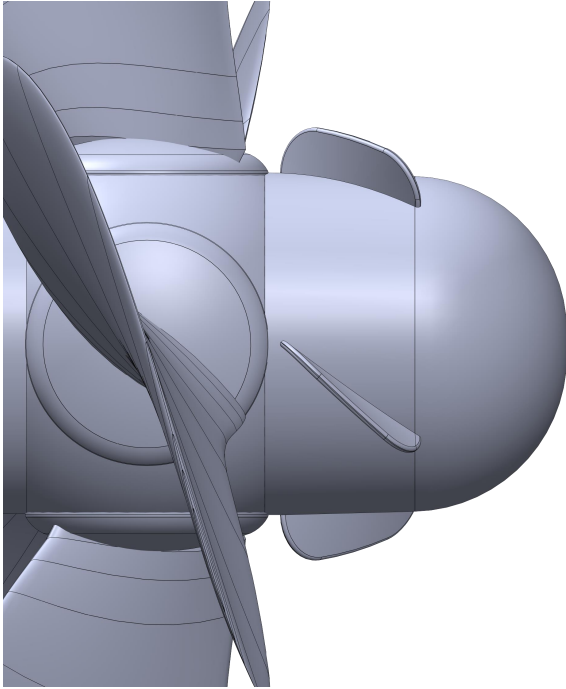


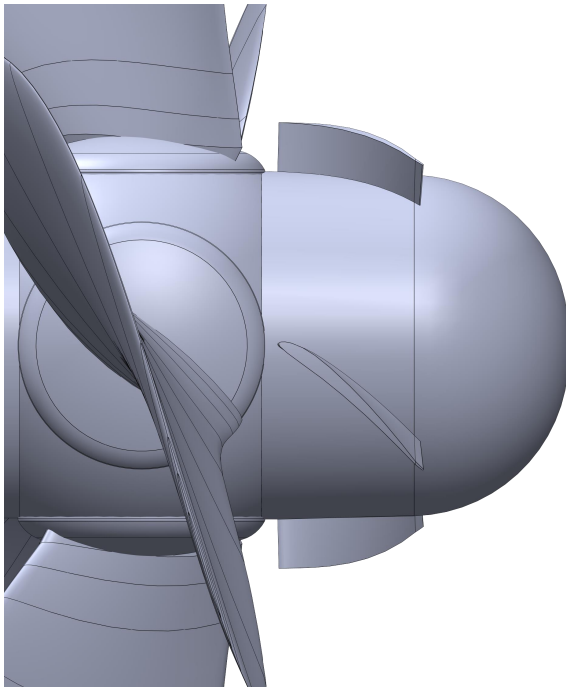
Figure A.12: Mesh on the PBCF fins

Appendix B

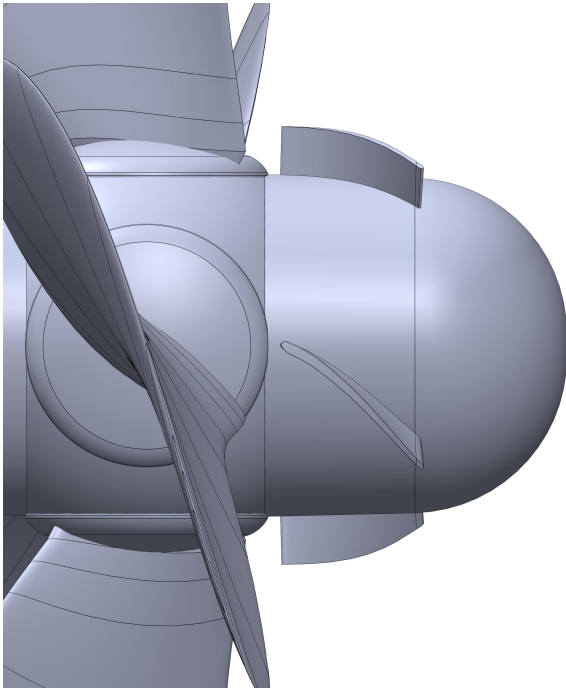
Visualisation of Investigated Hydrofoils



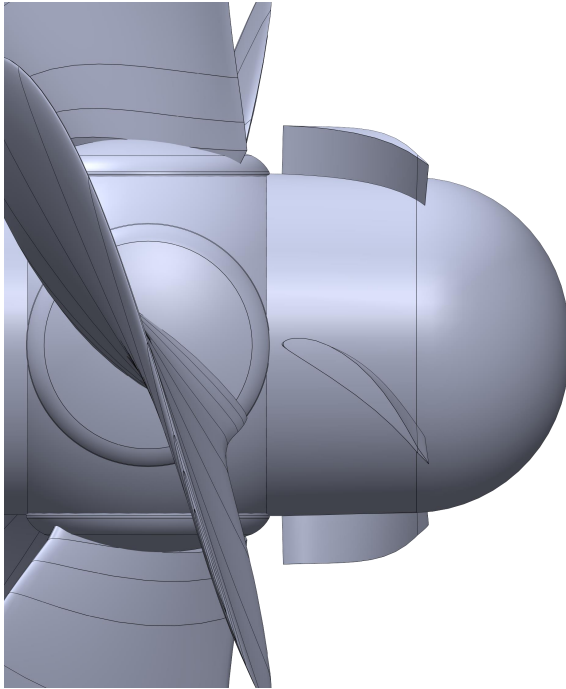
(a) Profile 0, Rectangular



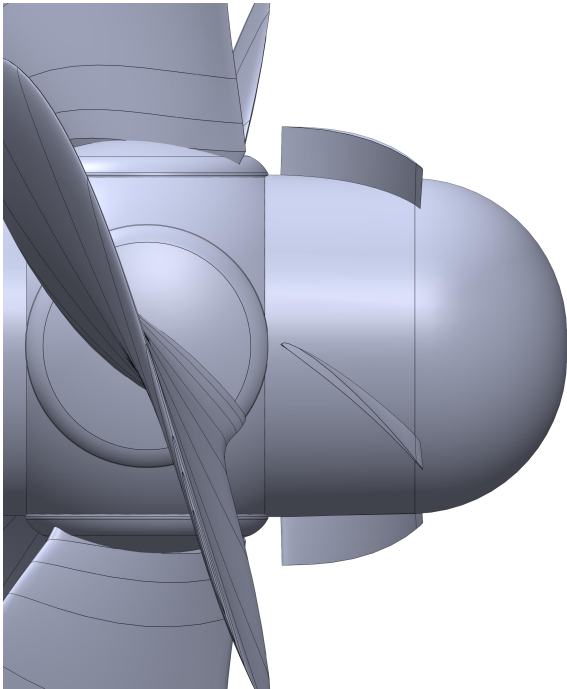
(b) Profile 1, AH-6-40-7



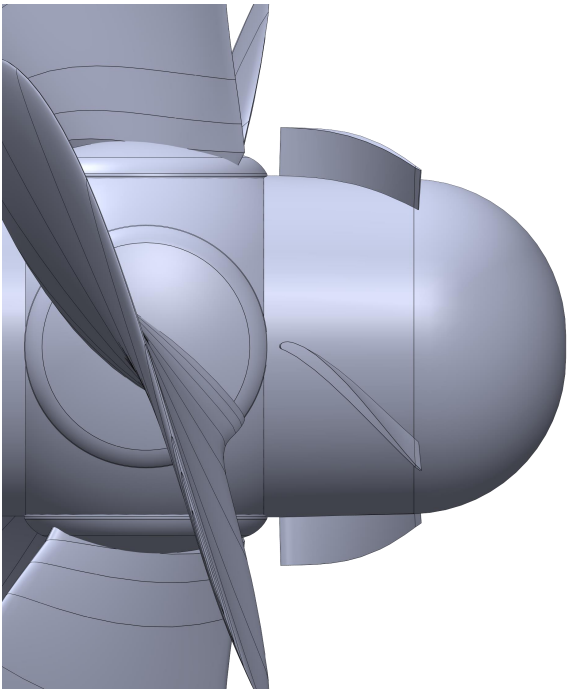
(c) Profile 2, Bergey BW-3



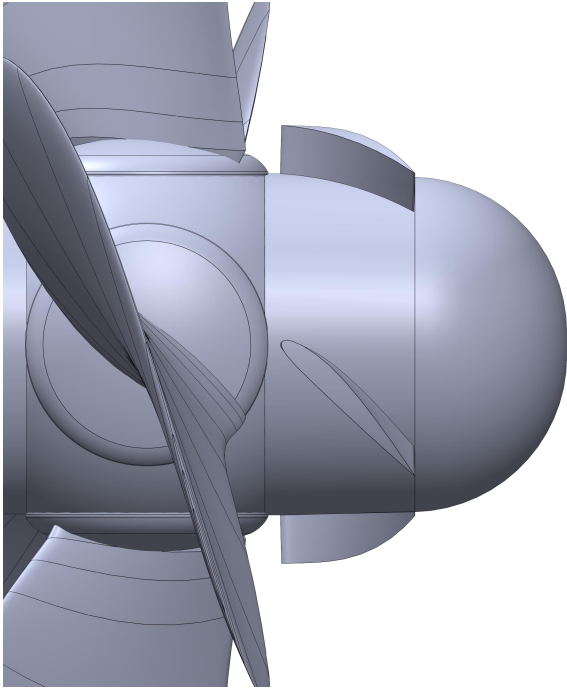
(d) Profile 3, CH10



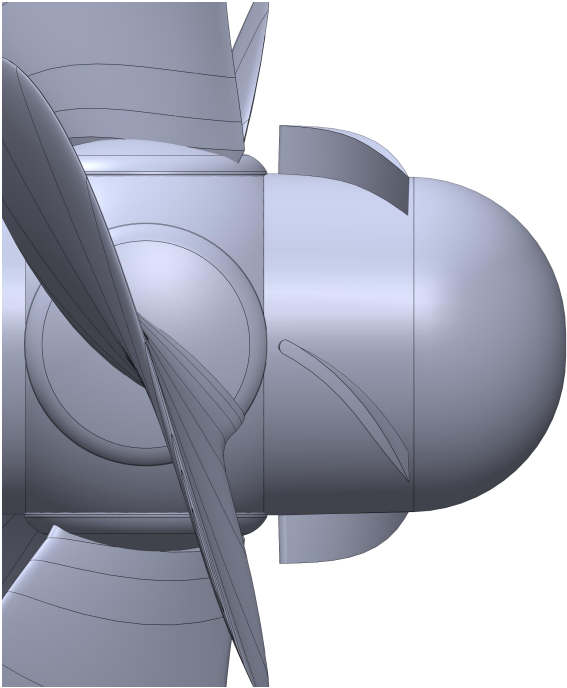
(e) Profile 4, E63



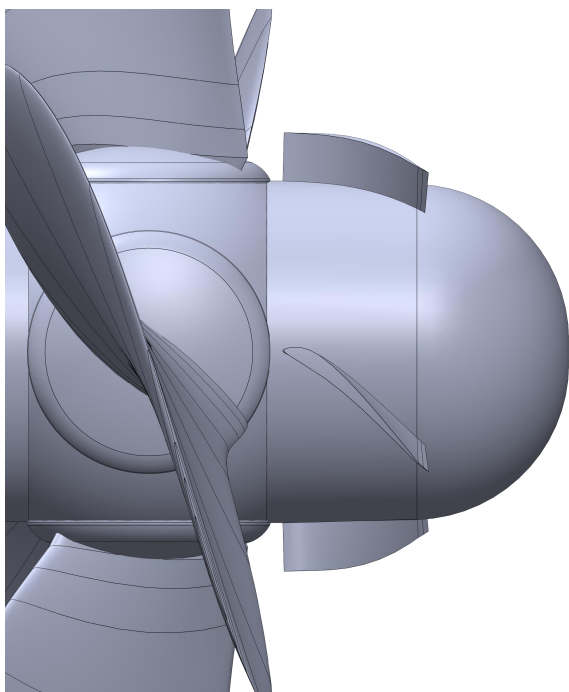
(f) Profile 5, GOE 79



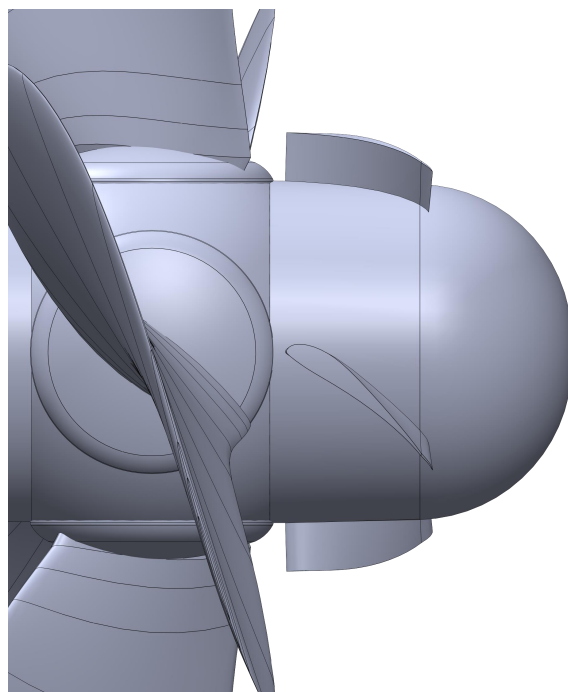
(g) Profile 6, NACA 4412



(h) Profile 7, cp-100-050-gn



(i) Profile 8, 20-32C



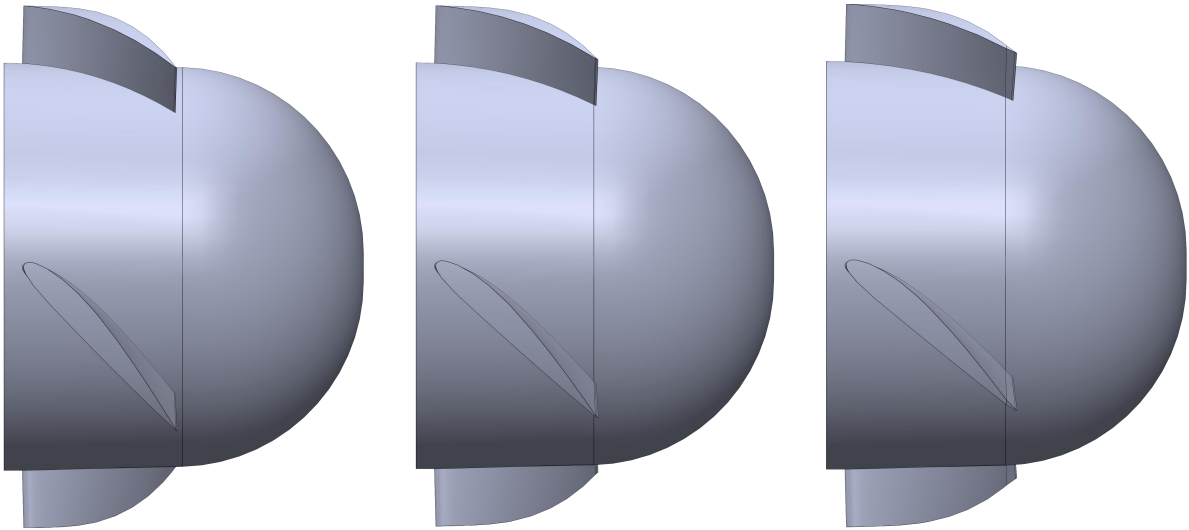
(j) Profile 9, S1223

Figure B.1

Appendix C

Parameter Study Visualisation

Installation Angle



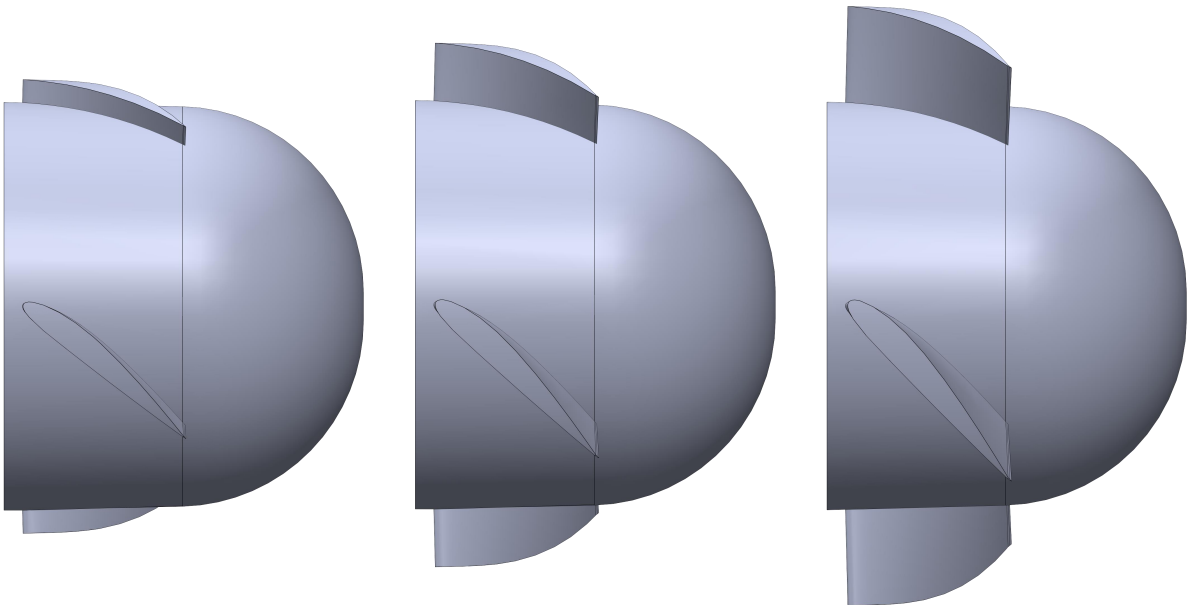
(a) Minimum: 47.1°.

(b) Optimum: 50.6°.

(c) Maximum: 53.6°.

Figure C.1

Span Height



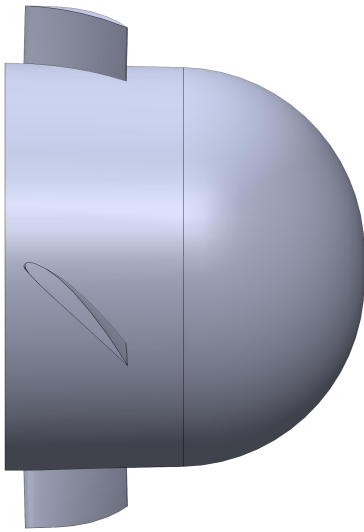
(a) Minimum: 3.0 mm.

(b) Optimum: 7.5 mm.

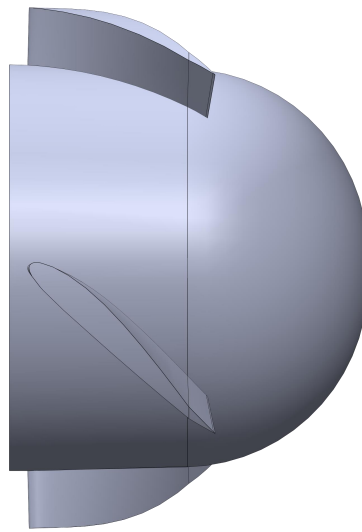
(c) Maximum: 12.5 mm.

Figure C.2

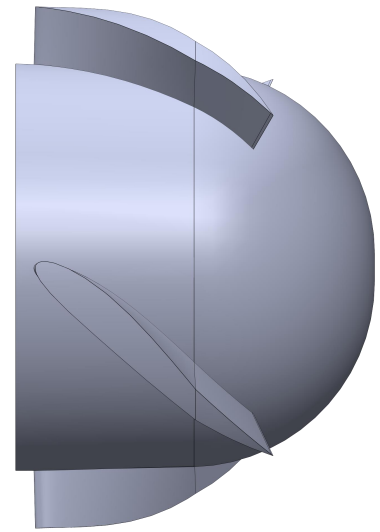
Chord Length



(a) Minimum: 17.0 mm.



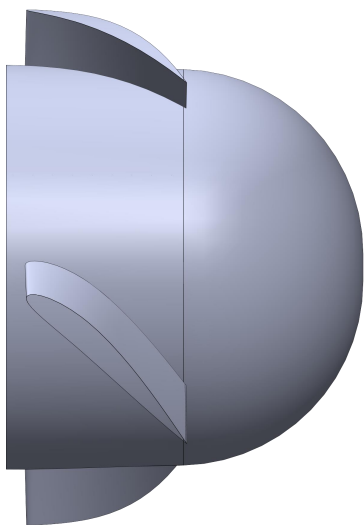
(b) Optimum: 30 mm.



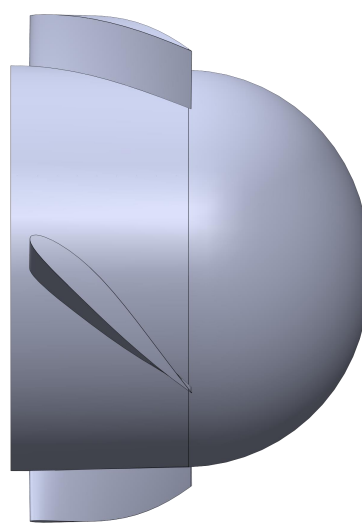
(c) Maximum: 37.0 mm.

Figure C.3

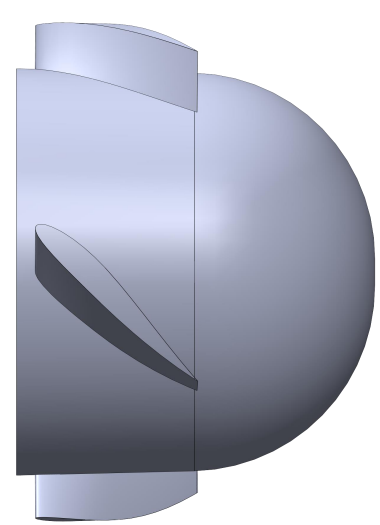
Rake Angle



(a) Minimum: -30°



(b) Optimum: 30°



(c) Maximum: 40°

Figure C.4

Camber

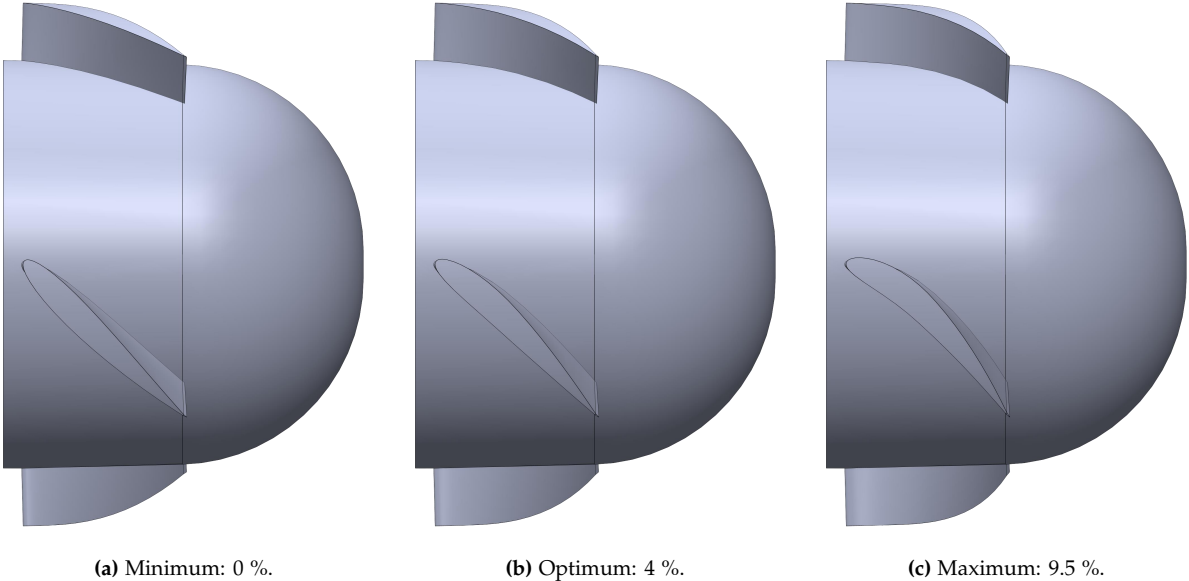


Figure C.5

Camber Position

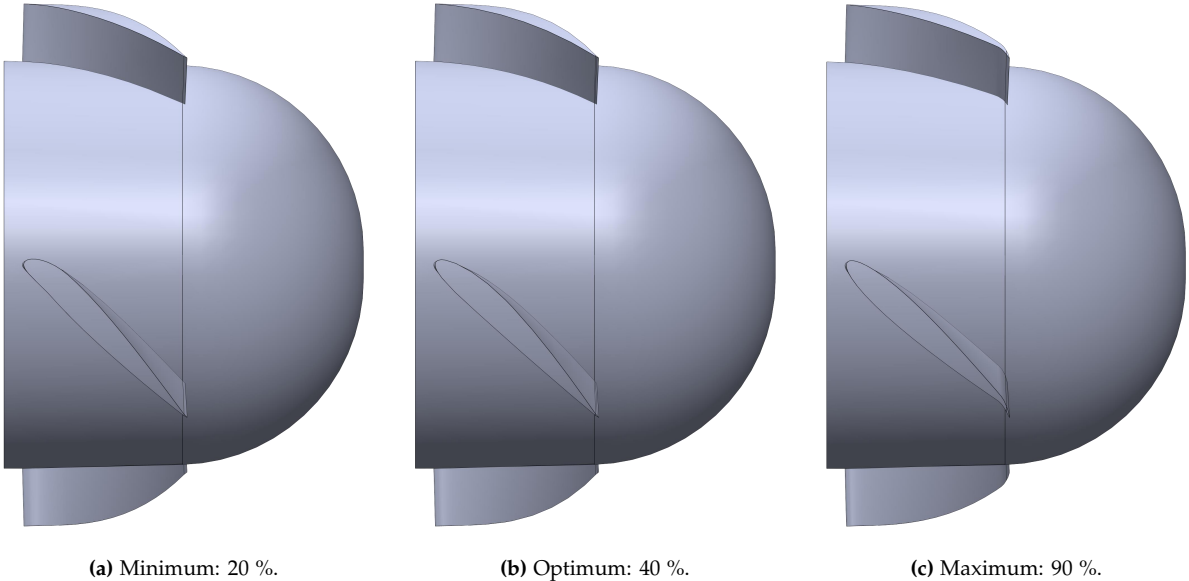
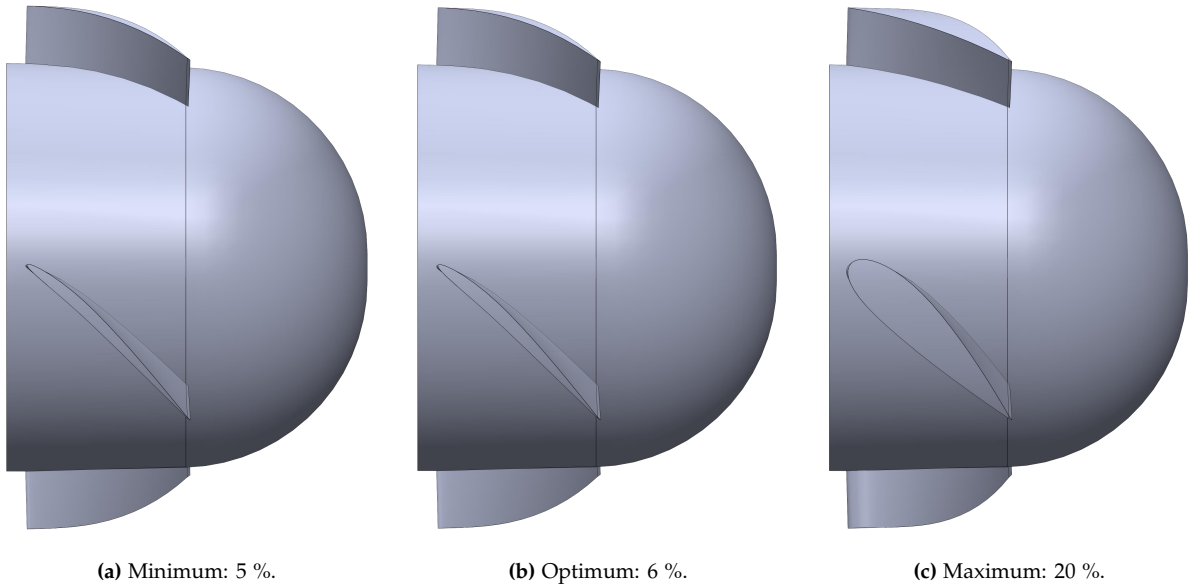
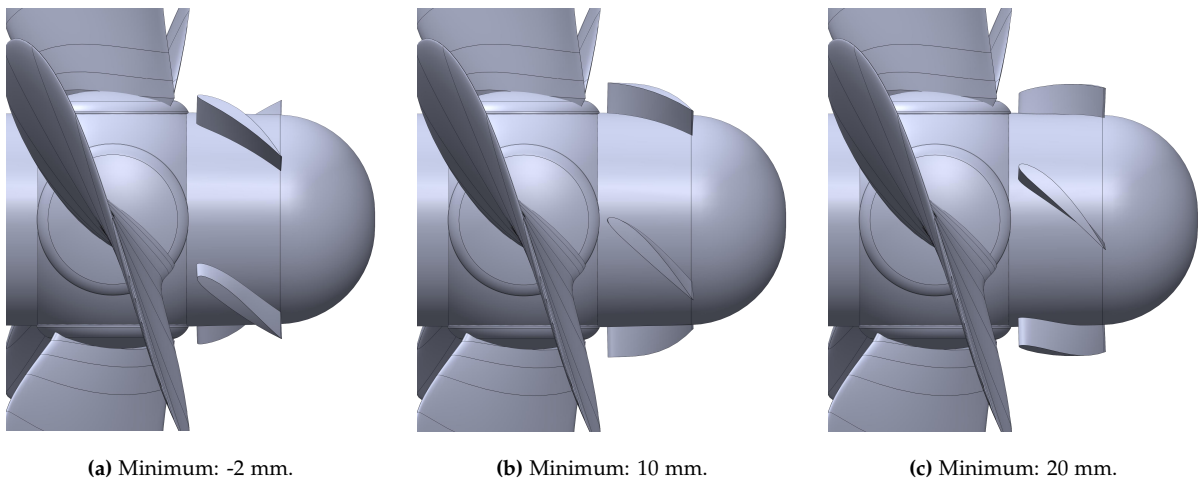
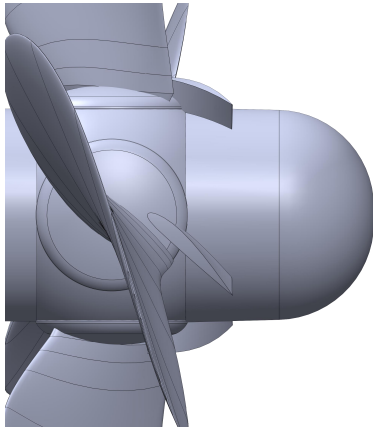
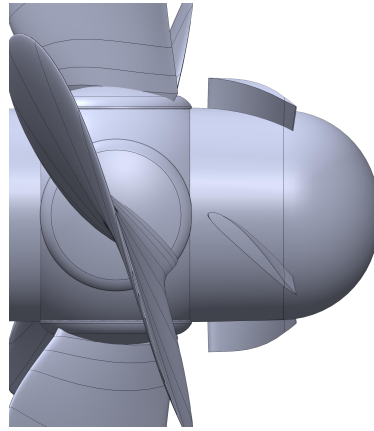
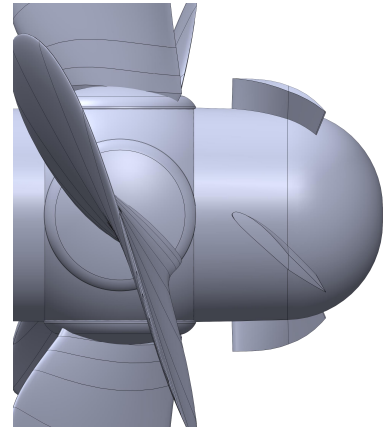


Figure C.6

Max. Thickness**Figure C.7****Circumferential Position****Figure C.8**

Axial Position**(a) Minimum: -5 mm.****(b) Optimum: 8 mm.****(c) Maximum: 14 mm.****Figure C.9**